Experimental Nanofluidics

- Capillary filling of nanochannels -

Morten Bo Lindholm Mikkelsen

Simon Eskild Jarlgaard

Peder Skafte-Pedersen
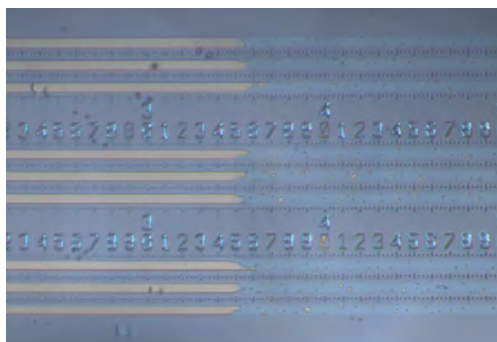
Supervisors

Associate Professor Anders Kristensen
&
Professor Henrik Bruus

MIC – Department of Micro and Nanotechnology
Technical University of Denmark

June 20th 2005

Abstract

As integrated microfluidic systems with modern technology can be fabricated with dimensions on nanoscale, it is vital to gain a knowledge of the behaviour of fluids in this regime. This report focuses on the investigation of capillary effects in nanochannels. Relevant theory is exploited to design a suitable nanofluidic system. A reliable cleanroom process sequence for making nanochannels on wafer scale is developed and used to implement the design in silicon and pyrex. Measurements are performed on the fabricated devices using different liquids and the data are analyzed for comparison with theory.

Resumé

Da det er muligt, ved brug af moderne teknologi, at fabrikere integrerede mikrofluidsystemer på nanoskala, er det vigtigt at opnå en viden om fluiders opførsel i dette område. Denne rapport fokuserer på undersøgelse af kapillareffekter i nanokanaler. Den relevante teori bliver udnyttet til at designe et passende nanofluidsystem. En pålidelig rentrumsprocesfølge, til fabrikation af nanokanaler på waferskala, bliver udviklet og benyttet til at implementere designet i silicium og pyrex. Målinger bliver udført på de fremstillede chips ved benyttelse af forskellige væsker. Data bliver efterfølgende analyseret og sammenholdt med teorien.

Preface

This report is written on the basis of experimental work performed in the spring 2005. The midterm project is a compulsory project for achieving the degree of Master of Science in Engineering at the Technical University of Denmark, DTU, and has been carried out at MIC – Department of Micro and Nanotechnology.

In the course of this project, several persons have been of great help. First of all we would like to thank our supervisors Anders Kristensen and Henrik Bruus for guidance regarding both theoretical and practical issues and for letting us carry out the project.

Furthermore many persons at MIC and DANCHIP have helped with various assistance for which we are very thankful. Especially Ph.D. student Anders Brask, M.Sc. student Søren Jakobsen, assistant professor Yanxin Zhuang and laboratory technician Helle Vendelbo Jensen have been of great help.

Morten Bo Lindholm Mikkelsen, s021709

Simon Eskild Jarlgaard, s021982

Peder Skafte - Pedersen, s021678

MIC – Department of Micro and Nanotechnology
Technical University of Denmark
June 20th 2005

Contents

List of Figures

List of Tables

List of symbols

Symbol	Description	Unit
$\boldsymbol{x}$	Position vector	m
$\boldsymbol{v}$	Velocity vector	m s^{-1}
v	Velocity	m s^{-1}
h	Channel height	m
w	Channel width	m
A	Area	m^2
T	Temperature	K
p	Pressure	N m^{-2}
R_{hyd}	Fluidic resistance	kg m^{-4} s^{-1}
Q	Volume flow rate	m^3 s^{-1}
ρ	Mass density	kg m^{-3}
η	Dynamic viscosity	kg m^{-1} s^{-1}
γ	Surface tension	J m^{-2}
θ	Contact angle	
Υ_{ev}	Electroviscous retardation factor	
ρ_{el}	Charge density	C m^{-3}
$\boldsymbol{E}$	Electric field	V m^{-1}
$\boldsymbol{J}$	Electric current density	A m^{-2}
$\boldsymbol{I}$	Electric current	A
ϵ	Permittivity	F m^{-1}
ϵ_r	Relative permittivity	
σ_{el}	Electrical conductivity	S m^{-1}
c_0	Bulk ion concentration	m^{-3}
λ_D	Debye length	m
ν	Electrokinetic distance, $\nu \equiv h/2\lambda_D$	
Z	Ionic valence	
M	Molar concentration	mol L^{-1}
r	Coefficient of correlation	
α	Level of significance	
e	Elementary charge	1.602×10^{-19} C
k_B	Boltzmann constant	1.381×10^{-23} J K^{-1}
N_A	Avogadro constant	6.022×10^{23} mol^{-1}

Chapter 1

Introduction

1.1 Motivation

The motivation for investigating capillary effects in nanoscale channels is to be found in the fact that integrated microsystems keep scaling down, approaching the sub micron regime. In particular for this project the concept of "Micro Total Analysis Systems" or "Lab-on-a-Chip" systems are of interest as these systems integrate fluidic systems with common MEMS, optical and electronic components.

The objective of these systems is to develop fully integrated laboratories on a single small disposable chip, which can perform specific analysis of for instance blood or groundwater samples. Moreover, the sample size required is much smaller than what is used today which is of great interest for e.g. the medical industry. Here a downsizing of the fluidic parts opens up for more advanced circuits on less space, and thereby fabrication with lower costs.

Furthermore nanoscale channels are the only suitable option in certain applications, as for instance DNA stretching devices, since DNA strings will unwind when placed in confined spaces, for which microscale channels are much too big.

An obvious and easily integrated use of nanocapillaries is as capillary pumps to make a flow of for instance laser dye or chemical solutions, where nano channels can be used for low flow rate pumps with high pressures.
But before this can be used in applications it is important to know the general physical behaviour.

1.2 Goal

The goal of this project is to develop a simple and reliable design and fabrication process, suitable for making channels with different dimensions on nanometer scale. Afterwards experiments must be performed to see if it is possible at all to fill the channels, and in that case to investigate if consistent patterns regarding filling speed and other phenomena can be observed when loading the channels with different liquids. It is also interesting to investigate if the general theory will be able to describe the fluidic behaviour on nanoscale,

approaching the limit of the continuum hypothesis.

The project is inspired by a similar experiment made by N.R. Tas *et al.* [9], who have proposed that electroviscous effects can retard the flow for small nanochannels. As a part of the experiments it will be investigated if we can confirm this assumption.

1.3   Execution

To be able to easily fabricate the devices and investigate the filling behaviour, the channels are constrained to nanometer scale only in one dimension, with width and length still being on micro- and millimeter scale respectively, providing a high aspect ratio.

The basic design idea will be based on the sketch shown in Fig. 1.1 with nanochannels connected to inlet structures.

In order to determine suitable dimensions of the channels and to enable an evaluation of the experimental results, the necessary fluidic theory covering capillary filling speed and electroviscous effects will be treated. This makes it possible to design the required fluidic systems, develop a measurement setup and compare the obtained results with theory.

Hereafter a process recipe that allows one to produce nanochannels with different heights will be developed. Using this, several channels will be fabricated and characterized in order to evaluate the reliability of the process.

Having built a suitable setup and fabricated the channels, the experiments will be carried out. The obtained data will finally be treated and compared to the theoretical predictions in order to evaluate the consistence between these.
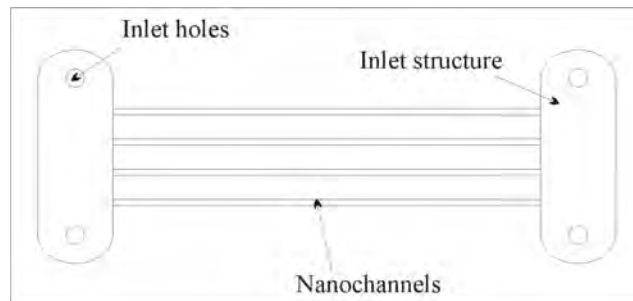
Figure 1.1: The general lay-out of the device with small nanochannels between two larger inlet structures.

Chapter 2

Theory

2.1 General assumptions

The theory describing our fluidic system will consist of three main topics, namely Poiseuille flow and velocity profile, capillary effects present due to the surface tension and contact angle, and finally the electroviscous effects arising from an electroosmotic back-flow in pressure driven channels. But first the conditions applying to the system must be made clear.

2.1.1 Continuum hypothesis

The fluidic theory is based on the assumption that the system fulfills the continuum hypothesis. In short terms this hypothesis states that the fluid can be treated as a continuous matter disregarding the actual molecular structure. Therefore the concept of fluid elements of finite dimension is used in contrast to a classical point particle. Determining the size of the fluid elements leads to the following considerations. The element must contain a sufficient amount of molecules in order to minimize statistical fluctuations. On the other hand there is an upper limit of element dimension in order to prohibit the possibility of physical variation throughout the element due to external forces. A typical side length [1, p. 5] fulfilling these requirements is

$$\lambda_{\text{typ}} = 10 \text{ nm}. \tag{2.1}$$

In this project the channel dimensions do approach the limit but it is uncertain if this will affect the validity of the continuum hypothesis. However, if the Poiseuille flow theory can experimentally be proved to be true, the hypothesis is not violated.

2.1.2 Gravitational forces

The effect of the gravitational forces must also be taken into account. In this project, however, the nanochannels are horizontally oriented and the pressure gradients from gravitation can safely be neglected due to the shallow height. The driving pressure, arising

from the capillary effect, will later be shown to have a magnitude justifying the neglection of any gravitational force, even if the channels should be slightly off-axis with the horisontal plane.

2.1.3   Compressibility and laminar flow

The system treated in this project is an open system fed with water moving at a low velocity, and incompressibility can therefore be assumed to hold. Furthermore the liquids in this system are regarded as Newtonian fluids.
The final assumption is that the flow is laminar, which holds for Reynolds number $Re \ll 1$, defined by

$$Re \equiv \frac{\rho V_0 h}{\eta} = \frac{\rho Q}{w \eta}, \tag{2.2}$$

where V_0 is the characteristic velocity found by dividing the flow rate Q by the cross sectional area. The assumption of laminar flow will be justified in Sec. 3.2.2 where the theory is applied to the actual system.

2.2   Poiseuille flow

A Poiseuille flow is present in the case of a steady-state pressure driven laminar flow in a long channel. The derivation of flow profiles is based on the central equation in fluid mechanics. This is the Navier-Stokes equation, which is also known as Newton's second law for fluid elements and can be derived using among others the concept of velocity fields and Newton's second law,

$$\rho \left(\frac{\partial}{\partial t} \boldsymbol{v} + (\boldsymbol{v} \cdot \boldsymbol{\nabla}) \boldsymbol{v} \right) = -\boldsymbol{\nabla} p + \eta \boldsymbol{\nabla}^2 \boldsymbol{v} + \rho_{\mathrm{el}} \boldsymbol{E}. \tag{2.3}$$

The two terms on the left side represents the product of the material time derivative and mass density. On the right side the body force densities from various sources are present. The first term is the pressure gradient force density, the second term arises from friction forces and the last term is the contribution from an electric field.

For the steady-state assumption to be true, the viscosity term of the Navier-Stokes equation must dominate the acceleration term, $\rho \partial_t \boldsymbol{v} \ll \eta \boldsymbol{\nabla}^2 \boldsymbol{v}$. For an infinite plates channel it can be shown that this is the case for $t \gg \rho h^2/(24\eta)$. The largest timescale will be for the channels with $h = 3.4\ \mu$m, $\rho = 1000$ kg/m^3 and $\eta = 0.89$ mPa s, which yields $t \gg 0.5\ \mu$s. For times later than this, the flow can be considered in steady-state.

In the following sections, the electrical contribution will be disregarded, as this will be treated later in the chapter.

2.2.1   Velocity profile and flow rate

Using the Navier-Stokes equation it is possible to determine the velocity profile for a Poiseuille flow in a given geometry. In this project the channels are rectangular with a
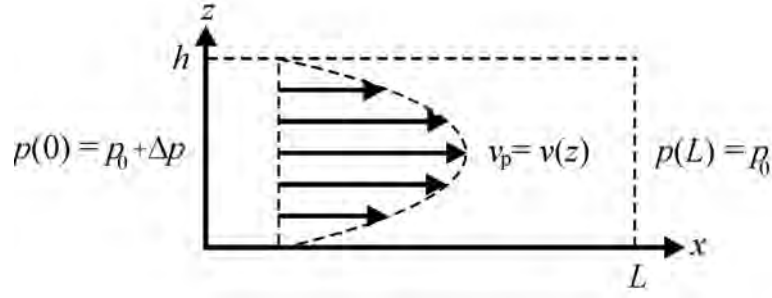
Figure 2.1: The parabolic flow profile between two infinitely wide planes placed a distance h apart and of length L.

ratio between width and height in the range from 20000:1 to 15:1. For the high aspect ratio it is a very good approximation to consider the structure as an infinitely wide channel without sidewalls, which yields the profile

$$v_{\mathrm{p}}(z) = \frac{\Delta p}{2\eta L} \left(h - z \right) z. \tag{2.4}$$

This and and the following equations assumes the pressure drop and channel to be oriented along the x-axis with height and width in the z- and y-axis respectively.

The low aspect ratio is too low for using this approximation and the effect of the sidewalls must be taken into account. Unfortunately an analytical solution to this problem does not exist, and the solution must be approximated by an infinite Fourier sum. Using the no-slip boundary condition, stating that the velocity of the fluid is zero at the channel/fluid interface, the following flow profile is obtained for a channel of height h and width w, [1, pp. 25-27]:

$$v_{\mathrm{p}}(y, z) = \frac{4h^2 \Delta p}{\pi^3 \eta L} \sum_{n,\mathrm{odd}}^{\infty} \frac{1}{n^3} \left(1 - \frac{\cosh(n\pi \frac{y}{h})}{\cosh(n\pi \frac{w}{2h})} \right) \sin \left(n\pi \frac{z}{h} \right) \tag{2.5}$$

The profile is plotted in Fig. 2.2 for a channel with aspect ratio 5:1 in arbitrary units.

The volume flow rate Q is defined as the volume passing through the channel per time unit and is easily found by integrating the velocity profile over the cross sectional area of the channel, yielding

$$Q = \frac{h^3 w \Delta p}{12\eta L} \tag{2.6}$$

for the infinite planes, and

$$Q = \frac{h^3 w \Delta p}{12\eta L} \left(1 - \sum_{n,\mathrm{odd}}^{\infty} \frac{192}{(n\pi)^5} \frac{h}{w} \tanh \left(n\pi \frac{w}{2h} \right) \right) \tag{2.7}$$

(a)   (b)
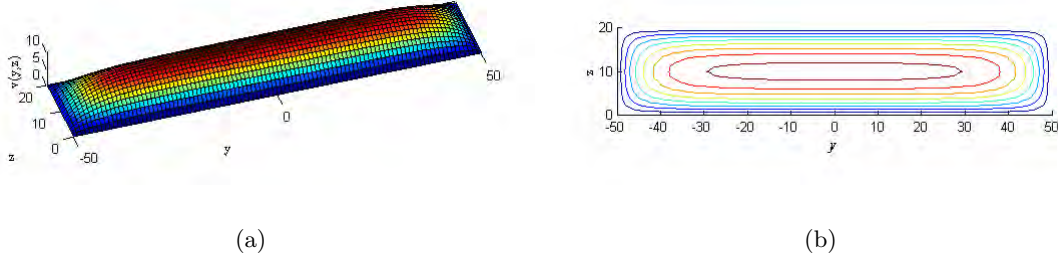
Figure 2.2: Velocity profile for Poiseuille flow in a rectangular channel of height h=20 and width w=100 in z- and y-direction respectively. The plots are made with arbitrary units and values using Eq. (2.5) with n in odd steps from 1 to 81. (a) shows the profile as a surface plot and in (b) the corresponding contour lines are plotted. The consequence of the no-slip boundary condition at the walls is clearly seen.

when accounted for the side walls. Assuming $\frac{h}{w} \to 0$ a significant simplification is obtained:

$$Q \approx \frac{h^3 w \Delta p}{12 \eta L} \left(1 - 0.630 \frac{h}{w}\right). \tag{2.8}$$

The last assumption may look a bit contradictory as it implies an infinite aspect ratio between width and height. But it only results in a deviation of 0.2% for an aspect ratio of 2:1, [1, p. 27], and for this project with an aspect ratio down to 15:1 the largest deviation will be on the order of 20 ppm.

For an aspect ratio of 15:1 the difference between using Eq. (2.7) and Eq. (2.8) is 4%, and hence it was decided to use Eq. (2.8) in general.

2.2.2   Fluidic resistance

For a Poiseuille flow there is a linear relation between the pressure difference over a channel and the flow, known as the Hagen-Poiseuille law:

$$\Delta p = R_{\text{hyd}} Q, \tag{2.9}$$

which is in analogy to Ohm's law for electrical circuits. For the rectangular channel the proportionality factor R_{hyd}, known as the hydraulic resistance, can be found from Eq. (2.8):

$$R_{\text{hyd}} \equiv \frac{\Delta p}{Q} = \frac{12 \eta L}{h^3 (w - 0.63h)}. \tag{2.10}$$

The equivalent resistance of coupled resistors is found the same way as for electrical circuits: $R_{\text{serial}}^{\text{hyd}} = R_1^{\text{hyd}} + R_2^{\text{hyd}}$ for serial connections and $1/R_{\text{parallel}}^{\text{hyd}} = 1/R_1^{\text{hyd}} + 1/R_2^{\text{hyd}}$ for parallel connections.

2.3 Capillary effects

Having determined the general behavior of a pressure driven flow, it is now time to consider the pressure source relevant for this project. But first the concepts of surface tension and contact angle must be defined.

2.3.1 Surface tension

Surface tension γ can be described from a molecular point of view considering an interface between a liquid and a gas. The molecules in the liquid form weak van der Waals bonds to the surrounding molecules. The surface molecules have less neighboring molecules and hence less bonds, as can be seen in Fig. 2.3. This leads to an increased energy per area at the surface, known as the surface tension. The consequence of this is that a liquid always tends to minimize the surface.

2.3.2 Contact angle

Another fundamental concept is the contact angle at the common interface between matter in liquid, gas, and solid phases at thermodynamic equilibrium. The angle is defined as the angle between the solid-liquid interface and the liquid-gas interface shown in Fig. 2.4. This specific angle is governed by the surface tensions of the three interfaces, liquid-solid, solid-gas, and gas-liquid, and it is given by Young's equation:

$$\cos\theta = \frac{\gamma_{\mathrm{sg}} - \gamma_{\mathrm{sl}}}{\gamma_{\mathrm{lg}}} \tag{2.11}$$

2.3.3 The Young-Laplace equation

On sub-millimeter scale, where the gravitational force is not dominant, the contact angle and the surface tension will control the shape of a liquid surface, which will be curved due to the principle of surface minimization. A fundamental property of a curved surface is the presence of a pressure drop across it. This can be derived by considering the thermodynamic equilibrium of surface energy $\gamma\delta A$ and pressure-volume energy $-\delta V\Delta p$
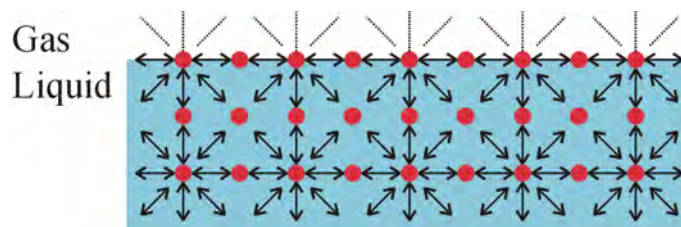
Figure 2.3: The description of surface tension at a gas and liquid interface in terms of molecular bonds. The molecules in the liquid form weak van der Waals bonds to the surrounding molecules. The surface molecules have less neighboring molecules and hence less bonds, shown by the dashed lines. This leads to an increased energy per area at the surface, known as the surface tension.
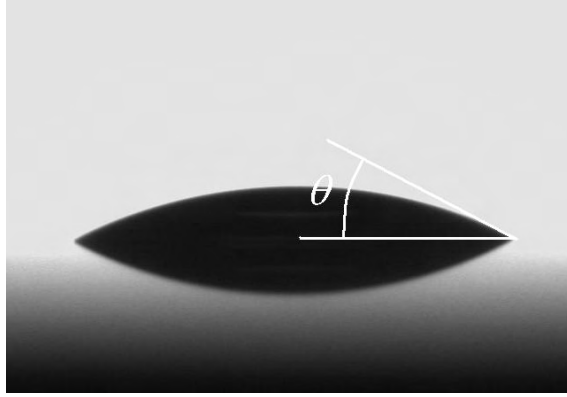
Figure 2.4: The contact angle shown on a droplet of Milli-Q water on a SiO$_2$ surface.

when a spherical surface is enlarged by a small area δA. If the curved surface is described by two radii of curvature, R_1 and R_2, the pressure drop across the surface can be found from the Young-Laplace equation,

$$\Delta p_{\text{Y-L}} = \gamma \left(\frac{1}{R_1} + \frac{1}{R_2} \right).$$
(2.12)

The pressure will be higher on the concave side of the surface, and can be explained as the pressure required to maintain the spherical form of the surface. The geometrical relation between the contact angle and the surface radius of curvature can be found from Fig. 2.5 to be:

$$R \cos \theta = \frac{h}{2},$$
(2.13)

Inserting this expression in Eq. (2.12) and neglecting the term involving the large radius, since the width to height ratio is very large, yields,

$$\Delta p_{\text{Y-L}} = \frac{2\gamma}{h} \cos \theta.$$
(2.14)

When dealing with high aspect ratio channels, leaving out the large radius provides a very good approximation. The ratio between the expression involving both radii, $\Delta P_{\text{Y-L full}}$
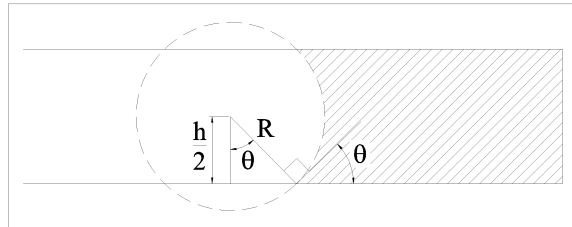
Figure 2.5: The front of a liquid (shaded) in a channel is shown. The radius of curvature can be found from the contact angle and the height.

and the simplified expression $\Delta P_{\text{Y-L simp.}}$, gives,

$$\frac{\Delta P_{\text{Y-L full}}}{\Delta P_{\text{Y-L simp.}}} = 1 + \frac{h}{w}. \tag{2.15}$$

This relative error is only $0.04\% - 0.6\%$ for heights varying from 20 nm to 300 nm, using a 50 μm wide channel. However for the deep channels e.g. 900 nm and 3.4 μm the error is 1.8 % and 6.8 % respectively. The simplified expression will nevertheless be used for all heights since the front from sidewall to sidewall, observed during measurements, at no time was well defined, which is required in order to use the full expression.

In nanochannels the Young-Laplace pressure can take on very high values. As an example, water with $\gamma = 73 \times 10^{-3}$ J m^{-2} and $\cos\theta = 1$, in a 50 nm channel will yield a pressure of $\Delta p_{\text{Y-L}} \approx 30$ bar.

2.3.4 The capillary pump

When a microfluidic chip is loaded with a liquid the curved surface known as the meniscus will readily form in the shallow hydrophillic channel, and the pressure difference over the surface will be established. Assuming that the reservoir of the chip is of macroscopic size, the gravitational force will dominate in this part of the system and form a plane surface with no pressure drop. Furthermore the height of the reservoir and the fluidic channel are assumed to be so small that there is no vertical pressure gradient in the liquid, and the pressure is the same everywhere in the reservoir. However, due to the pressure drop over the meniscus, the pressure in the water at the meniscus will be lower than normal pressure, as illustrated on Fig. 2.6. Thus, a decreasing pressure gradient $\partial_x p = \Delta p_{\text{Y-L}}/L(t)$ will exist from the meniscus towards the reservoir. The flow in the microchannel can now be modelled as a Poiseuille flow with a decreasing driving pressure and an increasing channel length. The model will hold true as long as the prerequisites of the flow are not violated. Calculations from Sec. 2.2 show that this does not happen for our channels. Using Eq. (2.14) and Eq. (2.10) the Hagen-Poiseuille law can be set up:

$$Q = \frac{h^3(w - 0.63h)}{12\eta L}\Delta p_{\text{Y-L}} = \frac{h^2(w - 0.63h)\gamma\cos\theta}{6\eta L(t)}. \tag{2.16}$$
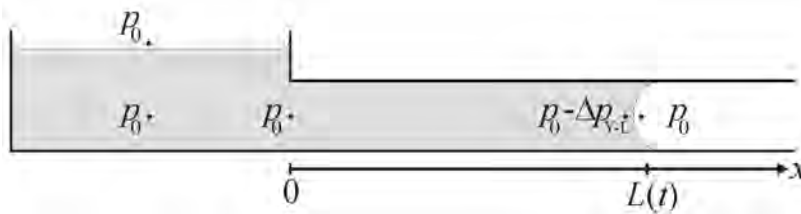
Figure 2.6: In a shallow macroscopic reservoir of a microfluidic chip, normal pressure is assumed to be everywhere in the liquid. In the microchannel, however, the pressure will be lower at the meniscus due to the Young-Laplace pressure drop over the surface. This gives a pressure gradient, that drives the liquid forward.

This expression allows one to find an expression for the distance the meniscus has travelled at a given time, by defining $Q = hw\frac{dL(t)}{dt}$ in Eq. (2.16) which gives

$$\frac{dL}{dt} = \frac{h(w - 0.63h)\gamma\cos\theta}{6\eta w L(t)} \tag{2.17}$$

Separation and integration yields

$$L^2(t) = \frac{h(w - 0.63h)\gamma\cos\theta}{3\eta w}t. \tag{2.18}$$

It is obvious that the integration constant is zero, since $L(t = 0) = 0$. If this theory applies to nanochannels, one thus expects a linear relation between $L^2(t)$ and t, where the quotient $L^2(t)/t$ for high width to height ratios with very good approximation depends linearly on the height. From Eq. (2.18) the time it takes to fill the channel to a given length, as well as the slope $a_p = \frac{\Delta L^2}{\Delta t}$, is readily obtained,

$$t = \frac{3w\eta L^2}{h(w - 0.63h)\gamma\cos\theta}, \tag{2.19}$$

$$a_p = \frac{h(w - 0.63h)\gamma\cos\theta}{3\eta w}. \tag{2.20}$$

2.4   Electrohydrodynamics

In the following sections the electrohydrodynamic effects will be taken into account in order to estimate their contribution to the deviation from the preceding simple theory omitting these effects.

2.4.1   Charges and streaming potential

The physical background for the presence of electrical effects in this system is caused by the fact that there is always a given amount of charge situated at the solid surfaces and distributed in the liquid in the form of ions, as liquids used in this project are electrolytes.

In equilibrium the solid surface charge will attract opposite charges, known as counterions, from the liquid to form a thin layer called the Stern layer whereas the co-ions of same charge are repelled. Outside this layer of immovable counterions the counterion concentration decays exponentially over a characteristic distance referred to as the Debye length λ_D, where the concentration $c(z)$ of both counterions and co-ions at infinity equals the bulk concentration c_0 resulting in a charge neutral liquid for distances from the wall greater than λ_D. The layer between the Stern layer and λ_D thus has a net charge density due to a predominance of counterions and is known as the Debye layer or the diffusive electrical double layer (EDL) as shown in Fig. 2.7.

A Poiseuille flow will move ions in the direction of the flow and due to the net charge in the EDL generate a current known as the streaming current I_s. This ion transport gives rise to formation of the so called streaming potential ϕ_s and corresponding electric field E_s

(a)

(b)
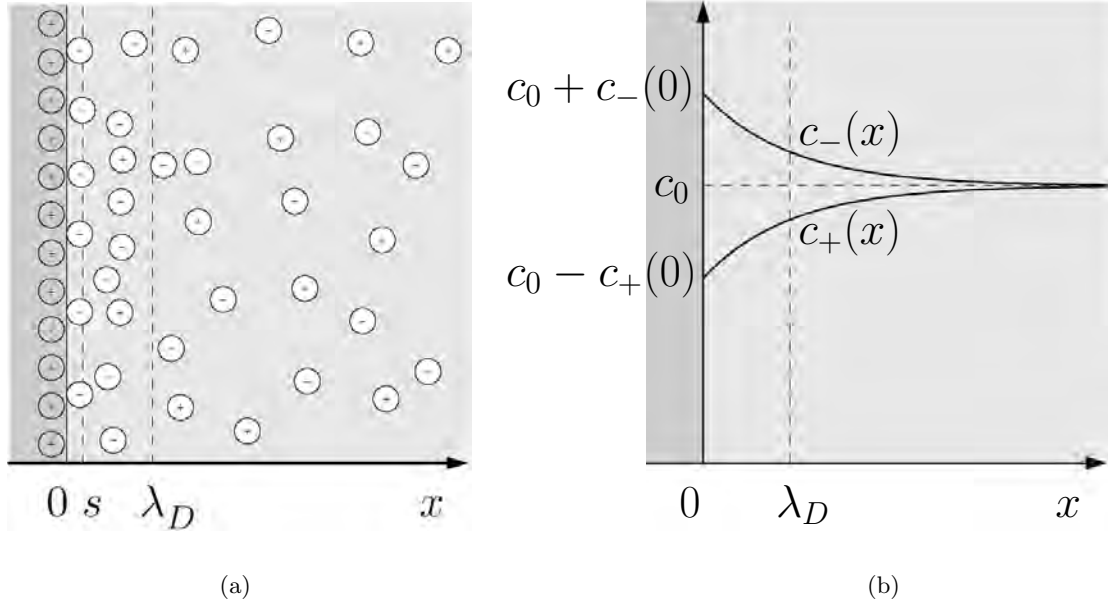
Figure 2.7: (a) Near charged surfaces, dark grey, the counterions in the electrolyte will be attracted whereas co-ions are repelled. (b) This leads to a predominance of counterions near the surface. Figures adapted from [1, Fig. 7.3].

parallel to the channel. Due to this, a current $\boldsymbol{I}_{\mathrm{con}}$, known as the conduction current will be established in the opposite direction of the streaming current as illustrated in Fig. 2.8.

For an open circuit as treated in this project, the equilibrium situation corresponds to the net current $\boldsymbol{I}_{\mathrm{net}}$ being zero, meaning that conduction and streaming current are numerically equal but of opposite sign.

The opposite flow of ions will, in combination with viscous drag of the surrounding
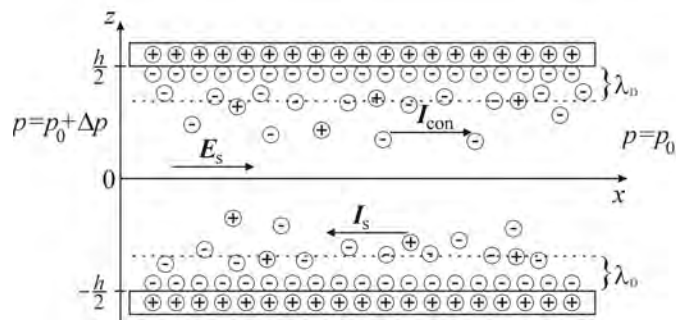
Figure 2.8: A Poiseuille flow results in a streaming current $\boldsymbol{I}_{\mathrm{s}}$ due the carriage of charges in the EDL. The accumulation of ions results in a electric field $\boldsymbol{E}_{\mathrm{s}}$ and thereby a conduction current $\boldsymbol{I}_{\mathrm{con}}$ anti-parallel to $\boldsymbol{I}_{\mathrm{s}}$. In equilibrium $|I_{\mathrm{con}}| = |I_{\mathrm{s}}|$.

molecules, result in a reduction of the volume flow. This phenomenon is known as the electroviscous effect or electroviscous retardation effect, although it has nothing to do with the viscosity except from the viscous drag. Due to the high surface to volume ratio of nanochannels, the effect will be much more pronounced than in macroscopic systems where the effect can safely be neglected. The theory is often used for channels with an external pressure source, but is expected also to apply to capillary filling as stated by N.R. Tas *et al.*[9].

2.4.2   Charge density and equilibrium potential

To determine an electroosmotic back-flow velocity profile, the charge density $\rho_{\mathrm{el}}(z) = Zec(z)$ and the corresponding electric equilibrium potential $\phi_{\mathrm{eq}}(z)$, which are sketched in Fig. 2.9, are considered. Due to the geometry of the nanochannels, ρ_{el} and ϕ_{eq} are considered only to depend on the z-coordinate restricted by the channel height.

Using the chemical potential and the boundary condition according to the coordinate system in Fig. 2.9

$$c_{\pm}(z = \infty) = c_0, \quad \phi_{\mathrm{eq}}(z = \infty) = 0, \tag{2.21}$$

it can be shown (see [1, p. 89]) that $\rho_{\mathrm{el}} = Zec_{\mathrm{net}}(z) = Ze(c_+(z) - c_-(z))$ is given by

$$\rho_{\mathrm{el}}(z) = -2Zec_0 \sinh\left(\frac{Ze}{k_B T}\phi_{\mathrm{eq}}(z)\right). \tag{2.22}$$

Notice that these boundary conditions might not hold in very narrow channels, as the Debye length in this case can be considerably larger than the channel height resulting in a Debye layer overlap. This can have the consequence that the concentration will never reach c_0. In this case corrections must be made. Nevertheless the boundary conditions are chosen in order to carry out further calculations.

Applying Eq. (2.22) to the one-dimensional Poisson equation yields

$$\frac{d^2}{dz^2}\phi_{\mathrm{eq}}(z) = \frac{2Zec_0}{\epsilon} \sinh\left(\frac{Ze}{k_B T}\phi_{\mathrm{eq}}(z)\right). \tag{2.23}$$
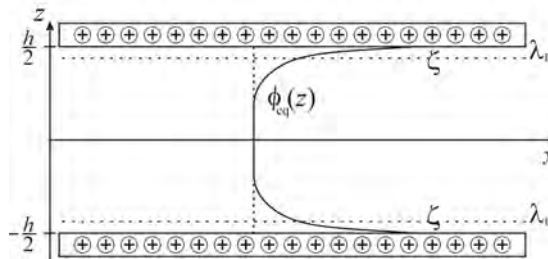
Figure 2.9: Equilibrium potential $\phi_{\mathrm{eq}}(z)$ between two positively charged walls. The potential ζ at the wall is a material dependent parameter called the zeta potential.

To obtain an analytical solution for this geometry the Debye-Hückel approximation $Ze\zeta \ll k_B T$, where the zeta potential ζ, being the maximum value of ϕ_{eq}, is introduced. This potential at the channel walls depends on the material combination, pH and temperature of the electrolyte and other parameters. Typical numerical values are in the range from a few millivolts to a few hundred millivolts (see e.g. [14]). At $T = 300$ K and $Z = 1$ the Debye-Hückel approximation demands $\zeta \ll 25$ mV. If this holds Eq. (2.22) can be linearized by a first order Taylor expansion to obtain

$$\rho_{el}(z) = -\frac{2(Ze)^2 c_0}{k_B T}\phi_{eq}(z). \tag{2.24}$$

With reference to the coordinate system shown in Fig. 2.9 one can easily obtain $\phi_{eq}(z)$ by inserting Eq. (2.24) in the one-dimensional Poisson equation with the boundary conditions

$$\phi_{eq}(z = -h/2) = \zeta, \quad \frac{d}{dz}\phi_{eq}(z = 0) = 0, \tag{2.25}$$

which yields

$$\phi_{eq}(z) = \frac{\cosh\left(\frac{z}{\lambda_D}\right)}{\cosh\left(\frac{h}{2\lambda_D}\right)}\zeta. \tag{2.26}$$

The Debye length λ_D is here defined as

$$\lambda_D \equiv \sqrt{\frac{\epsilon k_B T}{2(Ze)^2 c_0}}, \tag{2.27}$$

and typical values at room temperature range from $\lambda_D < 1$ nm for a strong electrolyte to $\lambda_D \approx 1$ μm for pure water.

2.4.3 Velocity profile

Assuming no external pressure, it is easily shown from Eqs. (2.3) and (2.26) that the velocity profile $v_{el}(z)$ in the x-direction caused by the electrical effects can be written as

$$v_{el} = \left(1 - \frac{\cosh\left(\frac{z}{\lambda_D}\right)}{\cosh\left(\frac{h}{2\lambda_D}\right)}\right)\frac{\epsilon\zeta}{\eta}E. \tag{2.28}$$

This electroosmotic velocity profile is derived under the assumption of an EDL with a negative net charge and an electric field applied in the negative x-direction, $\boldsymbol{E} = -E\boldsymbol{e_x}$, between two infinitely wide parallel plates positioned at $z = \pm h/2$. It is seen how the Debye length is important for the velocity profile, which according to this expression can be significantly reduced for a given electric field under the condition of Debye layer overlap.

As the Navier-Stokes equation in this symmetry is linear, one can obtain the total velocity profile by superposing the profile $v_{\mathrm{el}}(z)$ from the electroosmotic effect with a Poiseuille profile $v_{\mathrm{p}}(z)$,

$$v_{\mathrm{tot}}(z) = v_{\mathrm{p}}(z) + v_{\mathrm{el}}(z). \tag{2.29}$$

With a pressure drop in the positive x-direction, the negatively charged EDL will cause an electric field E_{s} co-parallel to this and thus v_{el} must be subtracted rather than added in Eq. (2.29). Hereby one obtains

$$v_{\mathrm{tot}}(z) = -\frac{1}{2\eta}\left(z^2 - \frac{h^2}{4}\right)\frac{\Delta p}{L} - \left(1 - \frac{\cosh\left(\frac{z}{\lambda_D}\right)}{\cosh\left(\frac{h}{2\lambda_D}\right)}\right)\frac{\epsilon\zeta}{\eta}E_{\mathrm{s}}, \tag{2.30}$$

where $E_{\mathrm{s}} = \frac{\Delta\phi_{\mathrm{s}}}{L}$.

Here $v_{\mathrm{p}}(z)$ does not account for the sides in order to ease calculations. The deviation of up to 4% between the two profiles is still far less than the uncertainty on the zeta potential, which is not known but will be estimated from the streaming potential.

2.4.4   Streaming field

E_s can be found by using the Nernst-Planck equation [1, p. 95] for the current density, which for this one-dimensional situation can be written as

$$J_x = -\sigma_{\mathrm{el}}\frac{d}{dx}\phi_{\mathrm{s}} + \rho\mathrm{el}(z)v_{\mathrm{tot}}(z), \tag{2.31}$$

where the conductivity σ_{el} is assumed constant everywhere in the electrolyte. The first term corresponds to the conduction current density whereas the last term is the streaming current density. Using the zero-current equilibrium condition one obtains

$$0 = \int_0^w dy \int_{-h/2}^{h/2} dz \left(-\sigma_{\mathrm{el}}\frac{d}{dx}\phi_{\mathrm{s}} + \rho_{\mathrm{el}}(z)v_{\mathrm{tot}}(z)\right)$$
$$0 = h\sigma_{\mathrm{el}}E_{\mathrm{s}} + \int_{-h/2}^{h/2} dz\rho_{\mathrm{el}}(z)v_{\mathrm{tot}}(z), \tag{2.32}$$

where $\rho_{\mathrm{el}}(z)$ and $v_{\mathrm{tot}}(z)$ are found using Eqs. (2.24), (2.26) and (2.30).

By integration the streaming field E_{s} is found to be

$$E_{\mathrm{s}} = \frac{T(h, \lambda_D)}{N(h, \lambda_D)}\frac{\epsilon\zeta\Delta p}{\eta L}, \tag{2.33}$$

with $T(h, \lambda_D)$ and $N(h, \lambda_D)$ given by

$$T(h, \lambda_D) = 2h - 4\lambda_D \tanh\left(\frac{h}{2\lambda_D}\right), \tag{2.34a}$$

$$N(h, \lambda_D) = 2h\sigma_{\text{el}} + \frac{\epsilon^2\zeta^2}{\eta}\left[-\frac{h}{\lambda_D^2}\frac{1}{\cosh^2\left(\frac{h}{2\lambda_D}\right)} + \frac{4}{\lambda_D}\tanh\left(\frac{h}{2\lambda_D}\right) - \frac{1}{\lambda_D}\frac{\sinh\left(\frac{h}{\lambda_D}\right)}{\cosh^2\left(\frac{h}{2\lambda_D}\right)}\right]. \tag{2.34b}$$

It is seen that the field is directly proportional to the pressure drop and has an inverse dependence on the conductivity. Furthermore, as $T(h, \lambda_D) > 0$ and $N(h, \lambda_D) > 0$, the sign of E_s is equal to ζ so $E_s\zeta \geq 0$, meaning that the electroviscous effect will always reduce the flow rate, independently of whether the walls are negatively or positively charged. In Fig. 2.10 the dependence on ζ is shown for water and a 0.1 M Borax solution in a 10 mm long and 1 μm high channel exerted to a pressure drop of 1.5 bar[1].

(a)   (b)
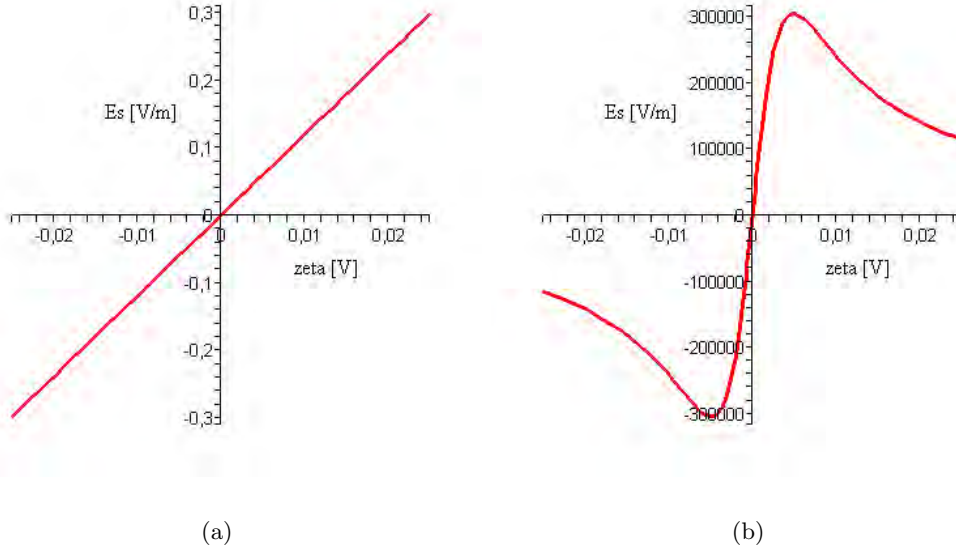
Figure 2.10: The streaming field E_s in a 1 μm high and 10 mm long channel with an external pressure drop of 1.5 bar. The liquid properties correspond to (a) 0.1 M Borax solution and (b) water. The low conductivity (see Table 7.1) of water results in a very high field. The field for the Borax solution in (a) appears to be linear, but if the range of ζ is extended, the qualitative picture is as in (b).

---

[1]These liquids are used in the experimental work, see Sec. 7.1

2.4.5   Electroviscous retardation factor

A very illustrative way to show the electroviscous effect is by calculating the electroviscous retardation factor Υ_{ev} which will be defined as[2]

$$\Upsilon_{\mathrm{ev}} \equiv \frac{Q_{\mathrm{p}}}{Q_{\mathrm{p}} + Q_{\mathrm{e}}}, \tag{2.35}$$

where Q_{p} is the flow rate of a pure Poiseuille flow given by Eq. (2.8) and $Q_{\mathrm{p}} + Q_{\mathrm{e}}$ is the actual flow rate[3] accounting for the electroviscous effect. This can be found from Eqs. (2.8) and (2.28) to be

$$Q_{\mathrm{p}} + Q_{\mathrm{e}} = Q_{\mathrm{tot}} = \frac{h^3 w \Delta p}{12 \eta L} \left(1 - 0.630 \frac{h}{w}\right) + \left[2\lambda_D \tanh\left(\frac{h}{2\lambda_D}\right) - h\right] w \frac{\epsilon \zeta}{\eta} E_{\mathrm{s}} \tag{2.36}$$

The retardation factor is thus easily found from Eqs. (2.8) and (2.36) to be

$$\Upsilon_{\mathrm{ev}} = \left[1 + \left[2\lambda_D \tanh\left(\frac{h}{2\lambda_d}\right) - h\right] \frac{(\epsilon\zeta)^2}{\eta} \left(\frac{T(h,\lambda_D)}{N(h,\lambda_D)}\right) \frac{12}{h^3} \left(1 - 0.63\frac{h}{w}\right)\right]^{-1}, \tag{2.37}$$

and plots of this as function of the electrokinetic distance $\nu \equiv h/(2\lambda_D)$ for various liquids and zeta potentials are given in Fig. 2.11.

As the flow rate is not constant in a capillary flow, Υ_{ev} will for comparison with measured results be determined from the slope of the L^2 vs. t-dependence mentioned in Sec. 2.3.4. Defining a_{meas} as the ratio $\Delta L^2/\Delta t$ obtained from measurements and using a_{p} given by Eq. (2.20), one finds

$$\Upsilon_{\mathrm{ev}} = \frac{a_{\mathrm{p}}}{a_{\mathrm{meas}}}. \tag{2.38}$$

If all parameters for a given system are known, Eq. (2.37) can be used to determine how well the experimental results fit with the theory. In this project it was intended to measure the zeta potential by measuring ϕ_{s} over a channel with an externally applied pressure. However time did not allow for this why the zeta potential is unknown. Thus Υ_{ev} will instead be used to estimate ζ to determine if it has the right order of magnitude ($\sim$mV). If this turns out to be the case, it indicates, that the described theory might apply to nanochannels.

However, one should remember that all preceding derivations have been made using the Debye-Hückel approximation and the dubious boundary conditions stated in Eq. (2.21), which might not apply to all channels treated in this project.

---

[2]Υ_{ev} is mostly seen expressed as the ratio between apparent and bulk viscosity η_a/η, see e.g. [13] and [9].

[3]Remember that with the convention used here for a flow in the positive x-direction, $Q_{\mathrm{p}} > 0$ and $Q_{\mathrm{e}} < 0$.

(a)

(b)

(c)
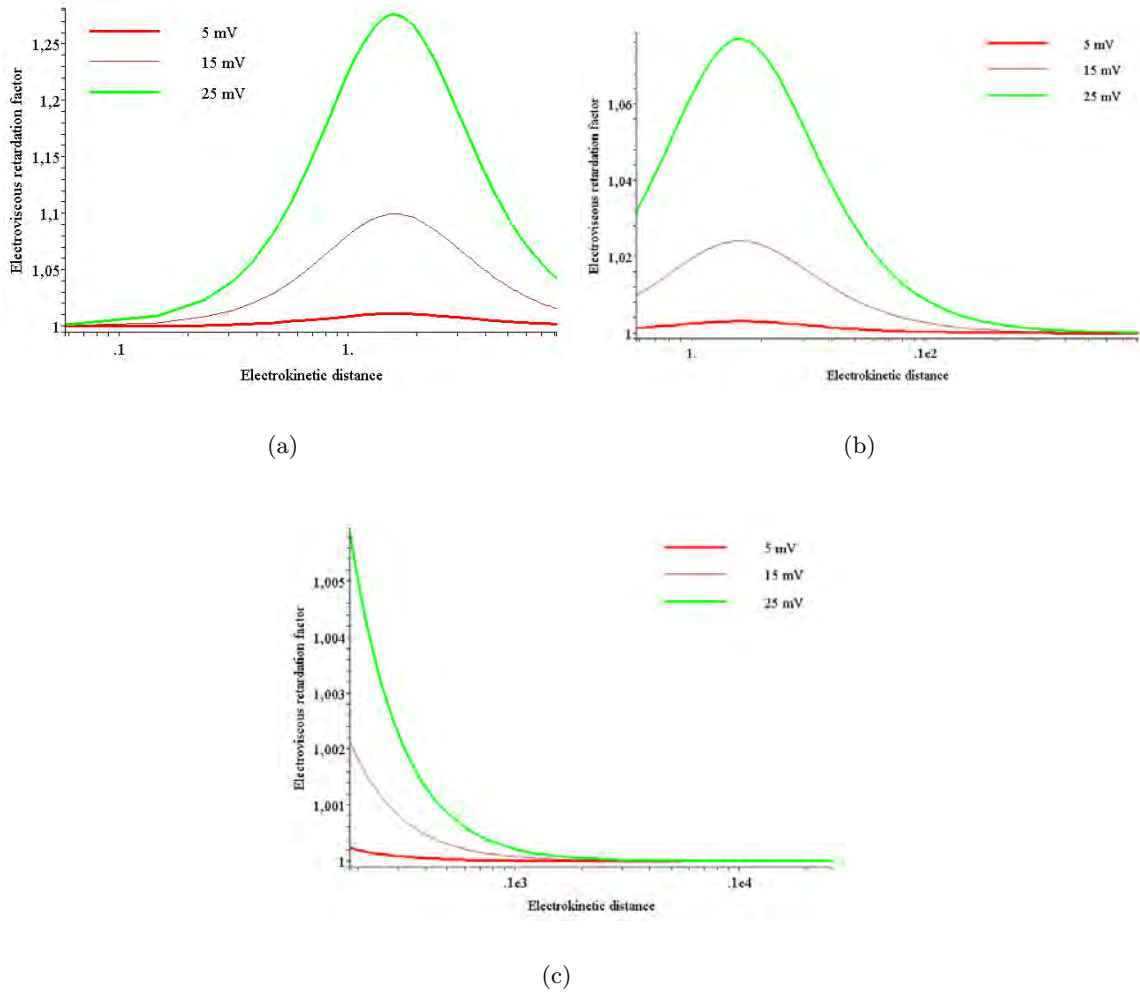
Figure 2.11: Electroviscous retardation factor Υ_{ev} as function of the electrokinetic distance $\nu = h/(2\lambda_D)$ using different zeta potentials for (a) water, (b) 0.1 mM Borax and (c) 0.1 M Borax. The range of ν corresponds to 25 nm $\leq h \leq 3.5$ μm. The theory is derived to be valid only in the case of $\nu > 1$.

Chapter 3

Design

3.1 Basic requirements

There are several demands the devices must fulfill. First of all the nanochannels must have a certain minimum length in order to allow for sufficient data acquisition. On the other hand the chip size must be limited in order to allow integration of a reasonable number of devices on each silicon wafer. As the main purpose of the project is to measure the filling speed of a liquid fed into the device, it is clear that a design must be made, where the position of the meniscus can be easily determined. Using a microscope fitted with a camera for detection, a very simple solution for length determination is to apply rulers near the channels. This can be done with very high precision using standard micromachining techniques in connection with the channel fabrication process.

The fabrication process dictates that the channels get a rectangular cross sectional shape being on nanometer scale in one dimension only. Therefore the overall design of the devices based on the sketch in Fig. 1.1 will contain a certain amount of channels being on nanometer scale in height and micron scale in width, with the aspect ratios mentioned in Sec. 2.2.1. The fabrication will primarily be based on clean room processing of silicon wafers. The transparent lid allowing for optical surveillance will be made of pyrex.

3.2 Layout of various chips

The primary design was intentionally made for channels ranging from approx. 30 nm to 500 nm in height. Later in the process it was decided to extend the spectrum up to approx. 3 μm thus covering two decades of heights.

It was decided to make several designs in order to investigate the filling behaviour in different geometries.

3.2.1 Channel length

A suitable length of the channels must first be decided in order to have a filling time, which allows for obtaining enough data to determine the filling speed behaviour. Simultaneously

the design must be suitable for the measuring equipment. From Eq. (2.19) it can be estimated that for a 500 nm high and 15 mm long channel the theoretical filling time using pure water[1] is approx. 17 s. For smaller channel heights the time is of course longer as it is inversely proportional to the height. The 17 s are sufficient for data acquisition and therefore it has been decided to have 15 mm between the inlet structures, since this is the maximum field of view for the available microscope. Besides straight 15 mm channels, meanders with a total length of 74 mm have also been implemented in order to allow for measurements on taller channels than the 500 nm.

3.2.2 Inlet structure

As it is very important to know the position of the meniscus with respect to the beginning of the channel, a way must be found to make well defined ends of the channels. The inlet holes will be made in the pyrex lid and are not fabricated by a cleanroom process, and thus the edge of the hole cannot be used as the channels' starting point.

Furthermore it was observed from measurements on a test batch that placing the inlet hole directly on top of the nanochannels could cause uneven filling of the channels, as small irregularities at the edge of the hole easily could block parts of the channel.

A very efficient and precise way of solving the inlet problem is to make a dedicated inlet structure in the silicon. This can be fabricated with high precision cleanroom techniques, and if designed to have a much smaller fluidic resistance than the nanochannels, this structure can be considered as a reservoir having no influence on the fluidic resistance in the channel system. To determine if the flow is laminar, which is required to treat the channels as resistors in serial, the Reynolds number can be calculated as a function of the meniscus position L by inserting the relevant flow rate into Eq. (2.2). A plot is shown for various channel heights[2] in Fig. 3.1 and it is clear that only for the highest channel, Re slightly exceeds 1 in the very beginning of the channel. Thus the assumption of laminar flow can safely be applied to the system.

In this type of device, the channel height is the dominating geometrical parameter for the fluidic resistance given by Eq. (2.10). The calculations can be simplified by disregarding the width and assuming the same length of the inlet and nanochannels, whereby the following relation is found.

$$\frac{R_n}{R_i} = \frac{12\mu L}{wh_n^3}\frac{wh_i^3}{12\mu L} = \frac{h_i^3}{h_n^3}, \tag{3.1}$$

where the indices i and n refer to inlet structure and nanochannels respectively.

From this it is clear that as long as the inlet channels are chosen to be in the micro regime, their resistance can be neglected when compared to the nanochannels. For this project it has been chosen to use 20 μm deep inlet structures, which allows for nanochannels

---

[1]Calculated for a 50 μm wide channel. Contact angle has been set to zero and values for viscosity and surface tension as found in Table 7.1.

[2]These heights correspond to the ones obtained during the fabrication, and the simulation is made using the properties of water given in Table 7.1.
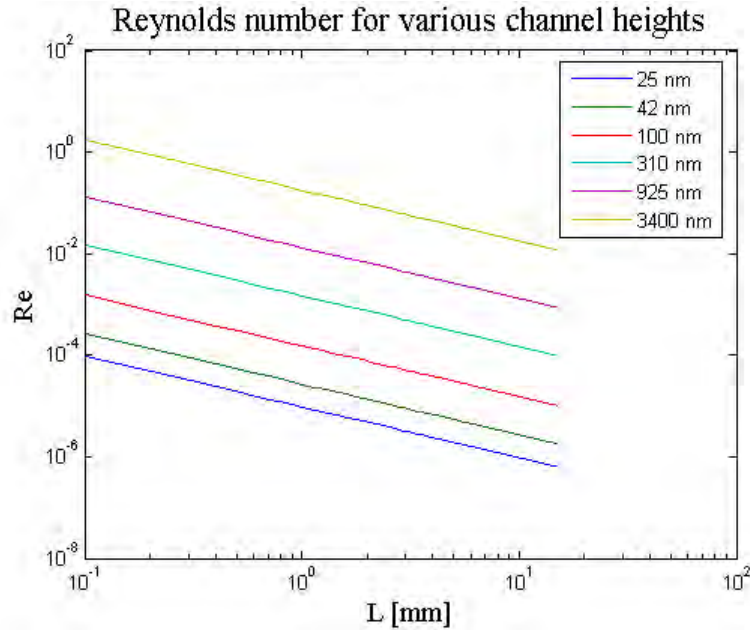
Figure 3.1: The Reynolds number as function of the meniscus position L from the beginning of the channel.

up to 3400 nm while still maintaining a resistance ratio[3] to the inlet channels in the order of 1:200.

Another advantage of using a dedicated microscopic inlet structure is the possibility for filling several nanochannels on the same device using only one inlet hole. This can be achieved using the design principle shown in Fig. 1.1. If the nano channel array has a total width of for instance 4 mm, the time between water enters the first and last nanochannel, using a 20 μm deep hydrophilic inlet channel, is in the order of 50 μs due to capillary effects[4]. This yields an almost simultaneous filling of an entire array, making it easy to perform large amounts of data acquisition from one single device.

In connection to the loading process there are two major challenges to overcome. Firstly, when the liquid is loaded into the deep filling channel, one must ensure that the liquid can flow freely past the entire nano array. By making another hole at the end of the filling channel as shown in Fig. 3.2 the pressure in front of the meniscus is maintained at atmospheric pressure allowing a capillary effect in the entire length of the inlet channel. Secondly one must have in mind that the height of the filling channel is in the order of 10^2 to 10^3 times the height of the nanochannels meaning that these have only connection to the deep structure in the uppermost part of this. Therefore it is extremely important that the upper surface of the device is hydrophilic as there would otherwise be a risk of

---

[3]The ratio is of course dependent of the position of the meniscus in the nanochannel and is here only stated for the case where the distance from inlet hole to the beginning of the nanochannel equals the position of the meniscus in the channel.

[4]The parameters for water are the same as previously used in this chapter.
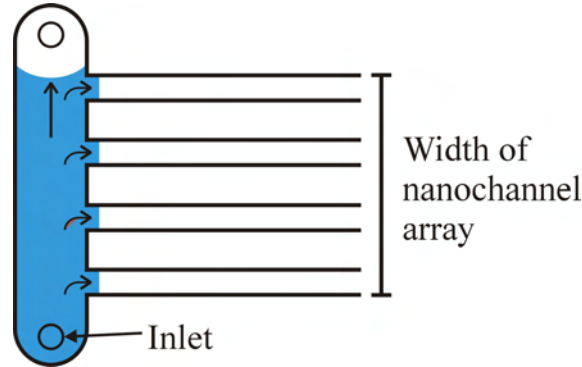
Figure 3.2: The common deep inlet structure shown in the left results in an almost simultaneous loading of the nanochannels across the array. The liquid is marked by the blue color.

not getting liquid into the nanochannels at all.

3.2.3   Nanochannel arrays

Having determined the overall principle, it is time to take a closer look at the nanochannel arrays. One of the main concerns regarding the geometry of these is the very large aspect ratio, since the width has to be detectable in a conventional microscope. This aspect ratio implies that it is uncertain how well defined the meniscus will be, and if the very low sidewalls will have any effect on the meniscus.

From experiments on a test batch with 1 mm wide channels coated with a thin SiO_2 it was found that for a height of 500 nm the liquid had a tendency to creep along the sides making it hard to define the liquid front. In the previously mentioned capillary experiment with nanochannels by N.R. Tas *et al.*, [9], it has also been reported that the meniscus at a certain time began to enclose air bubbles. These observations could indicate that the sidewalls in despite of their vanishing area compared to top and bottom have a certain effect on the meniscus.

Simple calculations using Eq. (2.19) shows that the reduced resistance of a wide channel should theoretically only have little effect of the filling time for heights on nanoscale, and as an example the deviation from a 500 μm to a 20 μm wide channel with a height of 500 nm is down to 1.5%. Besides arrays with channels of equal width it was therefore also decided to make a chip with an array of channel widths varying from 20 μm to 500 μm to investigate, if other boundary effects influence the flow. This will subsequently be referred to as a rainbow array.

The channel width is limited by the resolution and magnification of the detection equipment. The utilized microscope can be adjusted to cover an area of approximately 2×2 mm^2. In this way it is of course not possible to cover the entire channel length, but the field of view still has a size making it possible to determine the position of the meniscus, if kept in the focal area by moving the sample during measurements.

3.2.4 Identification and characterization structures

Besides the inlet structures and nanochannels, test structures have also been included. As the channels are made in silicon covered by a pyrex lid, it is a good idea to make characterization of the channels both before and after bonding of the two wafers. Before bonding the lid to the processed silicon substrate, the height determination must be made by means of a stylus profiler. This characterization process has a potential risk of damaging the channel surface as the stylus is scanned across the surface. Therefore each chip has been equipped with a test channel array with the same width as the channels in the nanoarray on the given chip.

After bonding the final channel height can be determined using Scanning Electron Microscopy (SEM). A drawback with this method is that one has to cut through a channel in order to reveal the cross sectional shape. To avoid sacrifice of the chip, the previously mentioned test structures have been positioned so they cross the dicing street. In this way their cross section is exposed when the chips are cut out.

3.2.5 Final devices implemented on photo masks

Since the primary processing is carried out in cleanroom facilities, the design is implemented on photolithographic masks. The layout is made with the CAD program Tanner EDA L-Edit 11.01, and two masks are needed; one for the nanochannels and test structures and another for the rulers and inlet structures.

A total of five different designs constrained to an overall layout have been made. One design includes an array of nine 15 mm long and 50 μm wide nanochannels, and a similar design is implemented with 20 μm wide channels. The previously mentioned rainbow chips contain a total of eight 15 mm long channels ranging from 20 μm to 500 μm in width. Finally designs containing meanders of 20 μm and 50 μm channel width have been made.

Fig. 3.3 shows a device with an array of nine 50 nm wide nanochannels (in black) separated by rulers, although these are hard to see due to their small size. Common for all
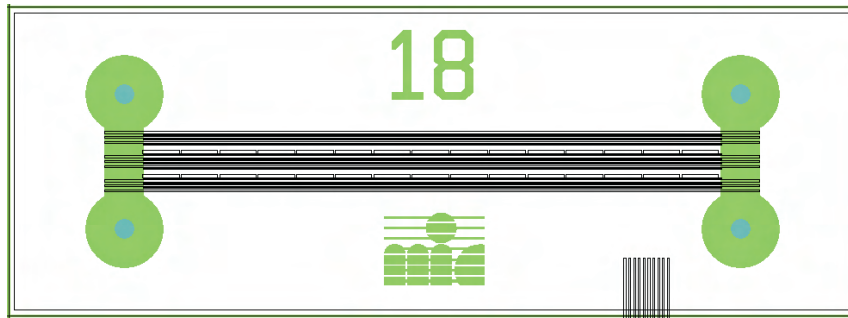
Figure 3.3: An example of a chip layout made in L-Edit. The chip contains nine 50 μm wide and 15 mm long nanochannels (black) separated by rulers. The inlet structure (green) has center channel width of 1 mm and circles of 2 mm i diameter, and the intended position of the inlet holes are marked by blue. In the lower right side a test structure is seen. The chip has a total dimension of 8×22 mm^2.

devices is that the width of the nanochannel array is constrained to a maximum of 2 mm for compliance with the microscope. The rulers have been made with tick marks for every 25 μm and numbers for every 100 μm allowing for a sufficiently precise determination of the meniscus position. The inlet structures, which are green in Fig. 3.3, have a channel width of 1 mm and in each end circles with a diameter of 2 mm. These fairly large circles are made to ease the bonding process during which the holes in the lid have to be manually aligned to the silicon substrate. The intended position of the inlet holes are marked by the blue circles, although these are not implemented on photomasks. In App. I the five different designs are shown.

All chips have a dimension of 8×22 mm^2 which allows for integration of 26 chips on a 100 mm silicon wafer. The wafer has been divided into groups with four of each meander chip and six of each type of straight channel chip and is shown on the wafer scale layout in Fig. 3.4. The structures in the left and right side of the wafer are alignment marks.

Having made the wafer scale layout the fabrication can be commenced.
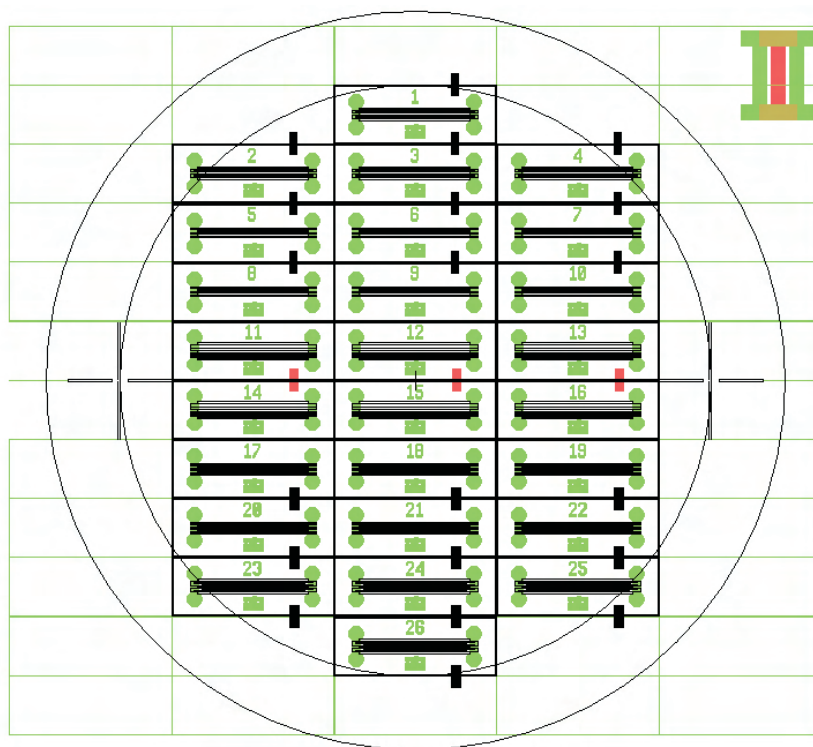
Figure 3.4: The integration of five different designs on photo masks for 100 mm silicon wafers. A total of 26 chips are integrated.

Chapter 4

Substrate fabrication

The fabrication of the channels is based on standard cleanroom techniques for silicon processing, and it is throughout this chapter assumed that the reader is familiar with the most common cleanroom techniques.

The general structure will be outlined and followed by simulations and descriptions of relevant process steps. Afterwards the performed fabrication with corresponding observations and problems is commented, and finally measurements on the substrates are used as base for characterization and evaluation of the silicon processing.

4.1   General Structure

The main challenge in the fabrication of the channels is to find a reliable and reproducible process sequence which allows the height of the channels to be controlled within a few nanometers over an entire wafer. The goal is to make a process allowing for heights in the range 20 nm to 1000 nm with a precision in the order of 5 nm. A simple process, which is known to give very homogeneous results on wafer scale, is the growth of SiO_2 using thermal oxidation. Using appropriate settings it is possible to control the thickness of the grown oxide with nanometer precision over the entire wafer, which makes oxidation an obvious choice for defining the channel height. The oxide can afterwards be removed in the pattern defining the channels.

As stated in Sec. 3.2.2 the inlet channels must be much deeper than the nanochannels, why they are etched directly in the silicon. Since a hydrophilic surface is required to ensure

| Si | | SiO_2 | | Resist | | Pyrex | | Film |

Figure 4.1: Cross sectional view of the silicon part of the device. The nanochannel is shown in the middle surrounded by inlet and outlet channels etched directly in the silicon. Notice the difference in thickness between the thick oxide on top defining the nanochannel height and the thin oxide layer in nano and inlet channels ensuring hydrophilic surfaces.

high capillary effects, a second oxide layer must be grown. A cross sectional view of the processed silicon part of the device is sketched in Fig. 4.1.

After the silicon processing, a pyrex lid with inlets is prepared and bonded with a KOH[1] assisted bonding process to seal the channels. These processes will be described in the following chapters. Finally the wafers are diced into chips with a circular saw.

4.2 Suprem Simulations

The growth of thermal oxide takes place at the silicon surface, why the growth rate is dependent both on the rate of the chemical reaction and diffusion of oxygen through the already grown oxide. For processes including more than one oxidation step the picture becomes rather complex and computer aided simulations must be made. For this purpose the 2D semiconductor simulation tool SUPREM is used.

4.2.1 Relevant processes and estimation of parameters

The most important steps in the simulation are the growth of the two oxide layers and the two isotropic wet etches. The first wet etch is the BHF etch defining the nanochannels and the second etch is connected to the KOH-based bonding process. The somewhat uncritical dry etch of the inlet structure is omitted in order to reduce the simulation time. In a few of the simulations this etch was subsequently included in order to check the transition between nanochannels and inlet structure. As expected no problems were found at the transition.

Before carrying out the simulations a rough estimation of the oxidation parameters is made by look-up in tables and graphs found in [4]. The etch rates for BHF and KOH are set to 70 nm/min and 4 nm/min respectively[2].

4.2.2 Thickness of bottom oxide and lift-up
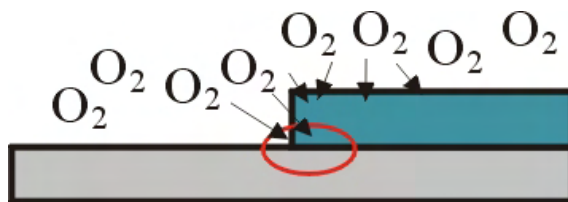
Figure 4.2: Due to the isotropic behaviour of a thermal oxidation the oxygen can diffuse from both top and side in the area marked by the circle. This results in a lift of the thick oxide at the corner as the growth rate in this area is higher than under the rest of the thick oxide.

As the bottom oxide must withstand a KOH etch for 150 s, the minimum thickness must be 10 nm. Choosing 20 nm for the bottom oxide should thus be sufficient to protect

---

[1]50 wt% Potassium hydroxide.

[2]These values are found in process cards made by Anders Michael Jørgensen, MIC, DTU, 2004.

the silicon[3]. A thicker oxide is also a possibility, but due to the isotropic behaviour of thermal oxidation, the oxygen can diffuse from both top and side at the interface between the thick oxide and the etched nanochannels, as shown in Fig. 4.2. This can result in a lift of the thick oxide at the corner, as the growth rate in this area is higher than under the rest of the thick oxide.

(a)

(b)

(c)

(d)
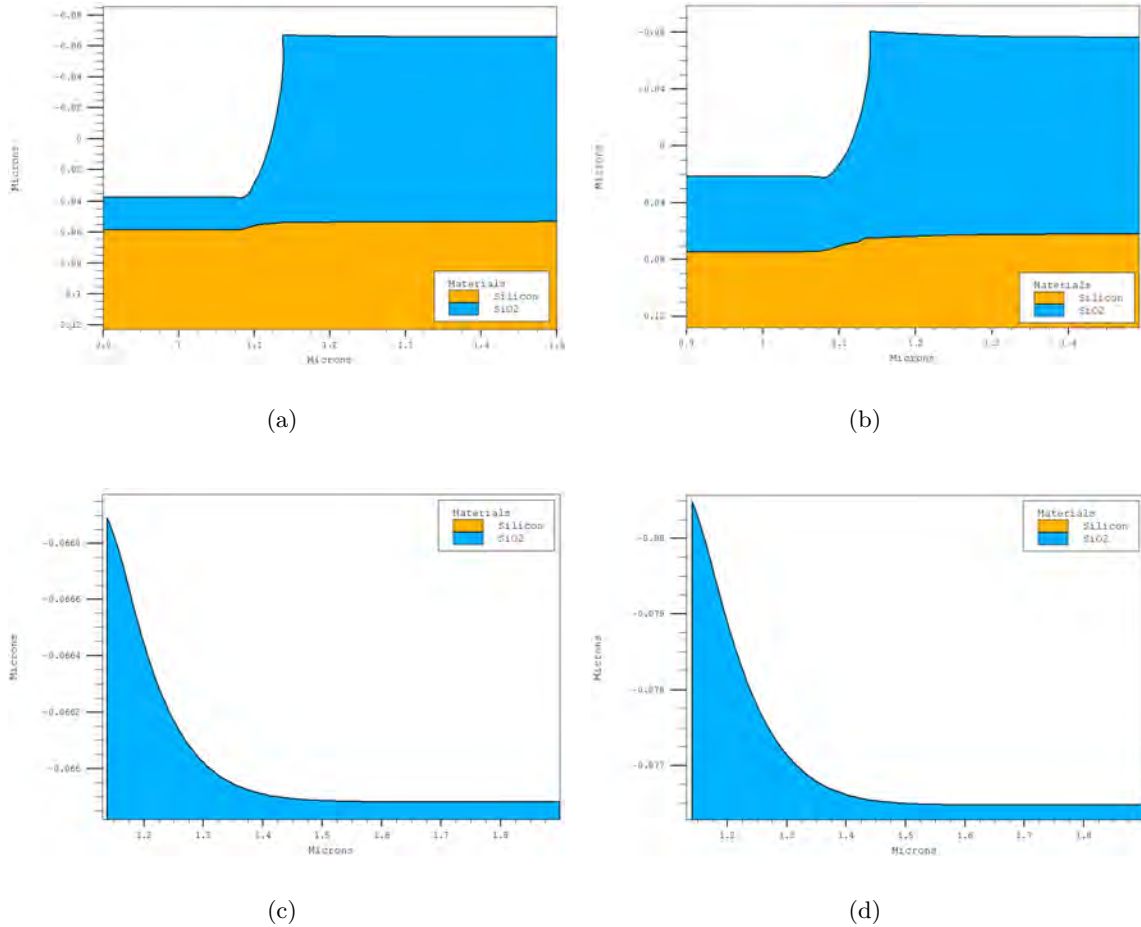
Figure 4.3: Simulation results. The oxidation process results in a lift of the corner. Figs. (a) and (b) shows the 100 nm channel near the sidewall with a bottom oxide of approximately 20 nm and 50 nm. In (c) and (d) a zoom of the corner is made and it is clear that the lift increases with the thickness of the final bottom oxide giving lifts of app. 1 nm and 4 nm. Notice that the scale differs from the different plots and is not constrained.

---

[3]If the silicon gets exposed to the KOH, the devices will immediately become useless as the anisotropic KOH etch in silicon takes place at an etch rate of 1400 nm/min (according to the previously mentioned process cards).

Increasing the thickness of the second oxide layer will thus increase this lift, and this can complicate the subsequent bonding process. In Fig. 4.3 the lift effect for a channel height of 100 nm is shown for 20 nm and 50 nm bottom oxide. In this simulation the lifts are found to be 1 nm and 4 nm respectively over a horizontal distance of approx. 0.5 μm, and hence so small that they are unlikely to cause any problems regarding the subsequent bonding process.

Practical experiences in the clean room revealed that the KOH etch rate could be considerably larger than the expected 4 nm/min depending on temperature (see Fig. 6.2). Furthermore bonding problems forced some substrates to be KOH etched more than once, which altogether made it necessary to increase the oxide thickness to 50 nm despite the increase in lift.

The lift-up also depend on the etch time of the BHF etch, as the isotropy of this changes the slope of the wall. The longer the etch time the more the wall will converge towards a vertical shape, which with reference to Fig. 4.2 is expected to cause a higher lift. Simulations also confirmed this, but the effect was found to be negligible. An example of the effect for different etch times can be found in App. C, where it is also shown how the final KOH etch slightly reduces the lift-up.

All in all the simulations indicate that the silicon processing should not cause any major troubles. Although the lift of the corner increases with etch time, it is still insignificant and very small compared to the variation in the surface of the blank silicon wafer. The over-etch of BHF is thus considered uncritical as long as it is made sure that the channels are etched down to the silicon. The recipes for the oxidation can be found in App. A and an example of a SUPREM input file is given in App. B. The parameters used in this file are for fabrication of 100 nm channels with 50 nm bottom oxide.

4.3   Process recipe

With determination of the oxidation parameters a cleanroom recipe, which takes more practical issues into account, can be developed. The following sections outline the general steps and considerations connected hereto. Detailed parameters and trivial steps connected to e.g. cleaning and standard photolithographic procedures are omitted for the sake of clarity.

The omitted details can be found in App. A where a detailed fabrication recipe with all parameters and steps is given. This appendix is suitable as a clean room guide and makes it possible to reproduce the devices.

4.3.1   Nanochannels

Generally the most critical and fragile structures should be fabricated as late as possible in the process, since there for every step always is a risk of damaging the structures during wafer handling. It is therefore preferable to make the nanochannels as the last structure. Unfortunately practical fabrication issues excludes this option, why the starting point for the fabrication is a (100)-oriented silicon wafer with a thermal oxide defining the channel

(a)   (b)
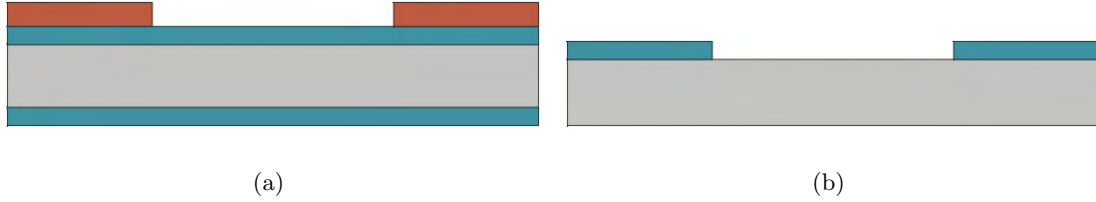
Figure 4.4: Cross section of the wafer with (a) developed resist pattern ready for BHF etch of nanochannels. In (b) the channel has been etched and the resist has been stripped. Notice that the backside oxide is also removed.

height. The highest capillary channels which are 3.4 μm deep, differ in process from the rest of the nanochannels and are shortly described in Sec. 4.3.3.

The pattern for the nanochannels is defined by a standard photolithography process. As a part of this process, the liquid photoresist is spun onto the wafer in a 1.5 μm layer. If the 20 μm deep channels had already been made, it would not be possible to obtain an even distribution of the resist leading to severe faults in the structure. Choosing to make the nanochannels first thus heavily reduces this source of error.

As the channel height is determined by the oxide thickness, it is very important that the oxide is completely removed in the desired pattern. Therefore the wafers with developed resist pattern are treated with an oxygen plasma prior to the BHF etch. This is done to ensure that possible monolayers of resist in the channel pattern are removed. Hereafter the wafers are ready for etching as shown in Fig. 4.4.

As the backside of the wafer is not protected during the BHF etch process, the oxide is here removed entirely. For thick oxides this can introduce stresses in the wafer causing it to warp slightly. However it is expected that this is not a problem in this project.

4.3.2 Inlet channels

Since this structure has a depth of approximately 20 μm and includes tick marks with a lateral size of 8.0×10.0 μm^2 for the rulers, it must be made by a strictly anisotropic etch. For this purpose an ASE reactive ion etch is chosen.

Due to the alternating etch and passivation process used in the ASE, the sidewalls will be scalloped rather than straight. However, this shape of the sidewalls does not affect the properties of the device. But besides being scalloped the walls are also covered with a thin passivation layer of C_4F_8, which must be removed before cleaning and oxidation. Therefore the etch process is to be followed by 3 min oxygen plasma etch. The structure as it looks after dry etch and subsequently strip of the photo resist is shown in Fig. 4.5.

After a final RCA cleaning process the wafer is now ready for growth of the bottom oxide giving the result sketched in Fig. 4.1.

Figure 4.5: The silicon structure with nanochannel and two inlet channels ready for the final oxidation.

4.3.3   3.4 μm channels

Although it is preferable to use the exact same process sequence for all channel heights to ensure the same surface properties for all batches, the 3.4 μm channels have been made by other means than etching of oxide. The reason for this is that the BHF etching process will give a lateral underetch of at least 3-4 μm, depending on the etch time, when etching the channels, if the these were defined by oxide. The same will be the case when pre-etching for the rulers and inlet channels, and thus the bonding area between rulers and channels is reduced[4]. This is undesirable as the meander channels are expected to be the only channels that allow for data acquisition at this height. And even the slightest bonding fault will immediately make it impossible to use the meanders, since the liquid will then be able to take a short cut and fill the channels from different positions.

Therefore the channels are simply made by a short ASE etch followed by an oxygen plasma, as shown in figure Fig. 4.6.

After etch of microchannels and inlet structures the wafers are, as for all the other bathes, oxidized to obtain a 50 nm bottom oxide.

(a)   (b)
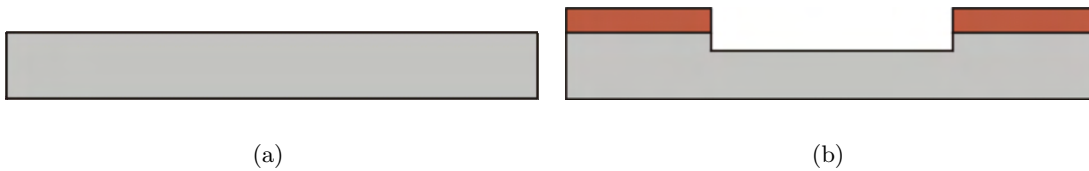
Figure 4.6: (a) The starting point for the 3.4 μm channels is a silicon wafer without oxide. (b) After a photolithography process the channels are etched directly in the silicon using a short ASE etch.

4.4   Performed fabrication

Besides the above mentioned process steps, the actual fabrication also included intermediate measurement steps in order to characterize the wafers. The oxide thickness from each oxidation step was measured by means of an ellipsometer. This was done on a single wafer from each batch. After finished silicon fabrication the channel height was measured by a Dektak 8 stylus profiler. By measuring several places at the same wafer, the important

---

[4]The distance between tick marks is reduced to 7 μm, whereas the distance from tick mark to channel is reduced to 16 μm when accounting for 50% over-etch.

uniformity of the process can be determined. Finally SEM measurements were planned to compare bonded channel height and open channel height in order to determine if collapse occurred.

4.4.1 Evaluation of test batches

Before the design described in Chap. 3 was made, two test batches containing 1 mm wide channels in a meander structure[5] were fabricated. This was done to test if it was possible to reach the simulated channel height using the stated process recipe. Furthermore it should reveal potential problems with the bonding process and of course give vital information about loading and filling issues, so that these could be taken into account when making the new design. The test chip fabrication differed from the above mentioned recipe as these did not contain any inlet structure and thus no dry etch processes were included.

Two batches of approx. 500 nm and 100 nm channel height were made. The first batch revealed that the bottom oxide should be increased to withstand the KOH etch. Besides from this, both batches showed very good correspondence with the simulations. The oxidation and BHF etch processes revealed no problems regarding the silicon processing and the yield was 100%. A very good uniformity on wafer scale is illustrated in Fig. 4.7. Some uncertainty due to noise is connected to the profiling, but it is from the measurements estimated to be within approx. 5 nm, and so the tolerance goal is absolutely fulfilled. Furthermore the lift-up mentioned in Sec. 4.2 cannot be be seen with this resolution as this is of the same magnitude as the noise.

The test batches thus indicated that the process was reliable and well suited for making uniform nanochannels on wafer scale. In App. D the simulated and measured values can be found.

4.4.2 Characterization and evaluation of main batches

In contrast to the test batches, the fabrication of the devices with the new design entailed several peculiar phenomena and unforeseen problems. Batch number one was intended to be 100 nm using the same recipe as for the test batch.

Unfortunately Dektak measurements on the 100 nm batch revealed that the channels were far from 100 nm and instead closer to 40 nm. This discrepancy between theory and practice lead to several considerations in order to determine the source of error. First of all, one could imagine that the BHF etch of the nanochannels had not been thoroughly done, although profiler scans showed very high uniformity across the wafers and wafers in between. Another explanation is that the oxidation recipe was simply another than intended although the ellipsometer showed an oxide thickness of 109 nm. Subsequent scrutinizing of the furnace log also showed that the registered recipe was not the intended, but neither one consistent with the ellipsometric measurements, channel heights nor simulations. Thus this first batch is still an unsolved mystery. The expected and measured values are found in Table 4.1.

---

[5]This structure originates from a project made by Morten Bo Lindholm Mikkelsen and Arne Nedergaard Hansen at MIC, DTU, 2004.
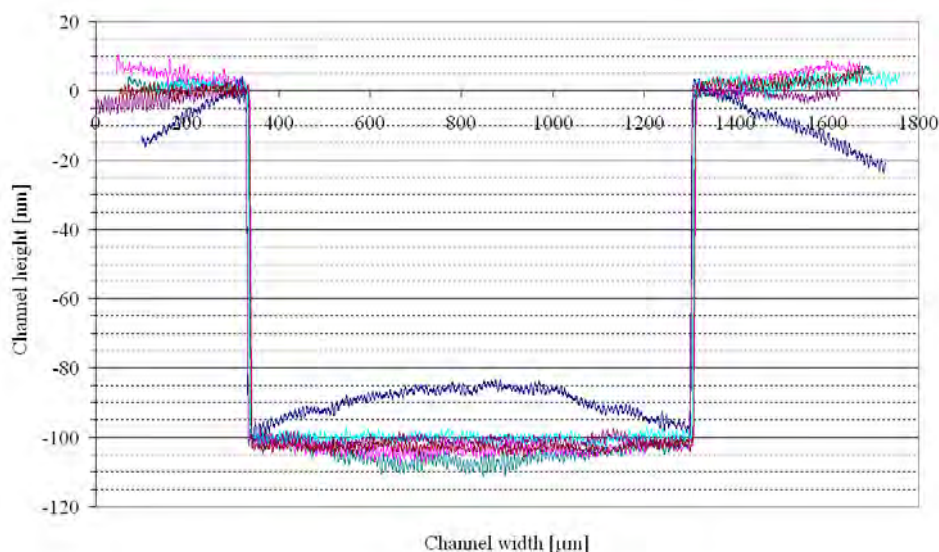
Figure 4.7: Superposed result from a Dektak surface scan across 100 nm channels at various places on a wafer from the test batch. The step height is seen to be very uniform and thus the process is well suited for making nanochannels with a very low tolerance. A small amount of stress appears, but it does not affect the step height.

For batch number two the correlation between theory and measurements was much better, as seen from Table 4.1, except from two wafers with a significantly reduced channel height. This phenomenon is assumed to arise from the oxidation process where oxidation dummies were not used. As shown i Fig. 4.9 this can due to heat radiation from the outer wafers result in an uneven growth rate between inner and outer wafers as the temperature tolerance must be within $\pm 0.5°C$ [3, p. 297], in order to assure consistent results. For the remaining batches this was taken into account and no major variation in the uniformity was registered hereafter. In Fig. 4.8 examples of Dektak scans are shown for the lowest obtained channels, with a height of 25 nm, and for a 300 nm channel. A diminutive amount of stress is seen, but the step height for every channel is very accurate.

Batch number		6	5	4	3	1	2		
Expected height	[nm]	**3400**	**925**	**304**	**99**	**99**	**41**	**41**	**41**
Oxide 1 (Suprem)	[nm]	n/a	968	341	115	86	54	54	54
Oxide 1 (Ellipsometer)	[nm]	n/a	956	334	108	109	52	n/a	n/a
Oxide 2 (Suprem)	[nm]	53	53	54	53	54	53	53	53
Oxide 2 (Ellipsometer)	[nm]	52	52	52	52	52	52	52	52
Channel (Suprem)	[nm]	n/a	925	304	99	75	41	41	41
Channel (Dektak)	[nm]	3400	925	310	100	42	42	32	25
Channel (SEM)	[nm]	3400	n/a	n/a	90	n/a	n/a	n/a	n/a

Table 4.1: Comparison of measured and simulated oxide thickness and channel height.

(a)

(b)
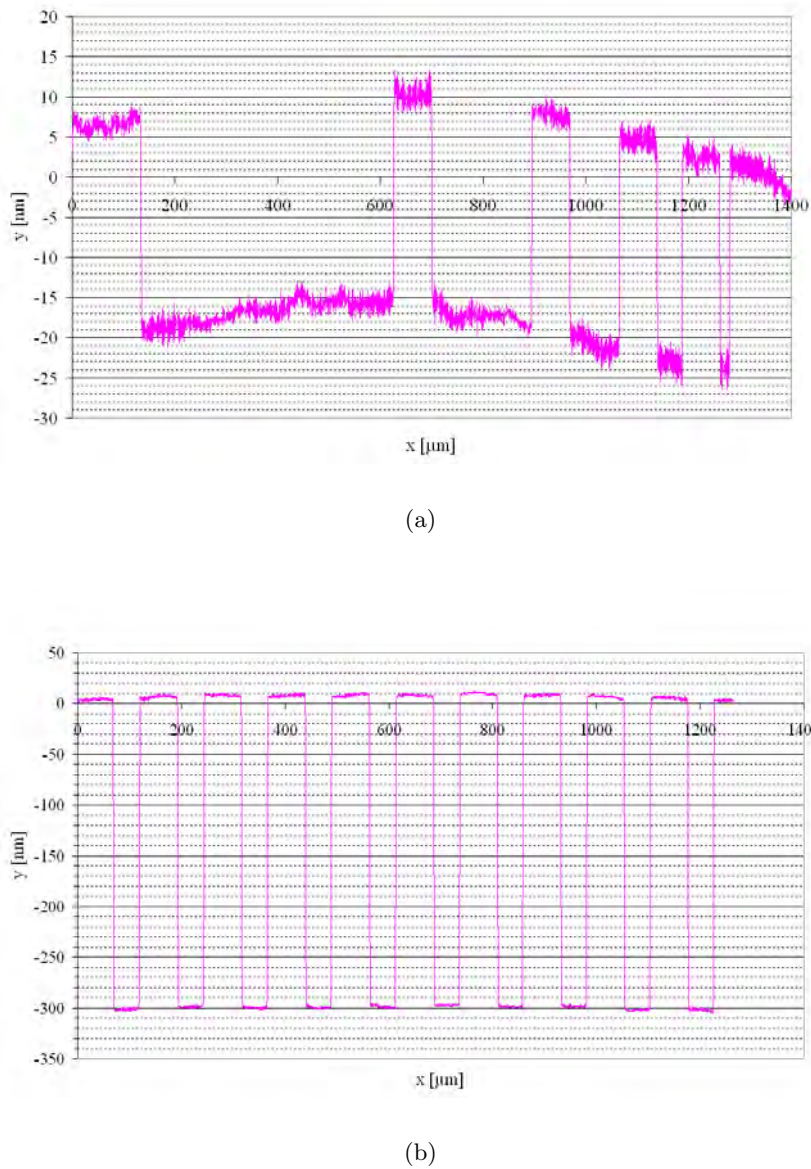
Figure 4.8: Dektak scan of a 25 nm rainbow test structure and 300 nm test structure with 50 μm wide channels. The step height for both scans is seen to be very uniform despite a tiny amount of stress.

The dry etch of the highest channels elapsed without any remarkable problems. As the ASE etches in cycles, it is not possible to adjust it precisely to a given height without making specific programming. An etch of 4 cycles resulted in a height of 3.4 μm. The disadvantage of using a dry etch is that one can not expect the same uniformity as with
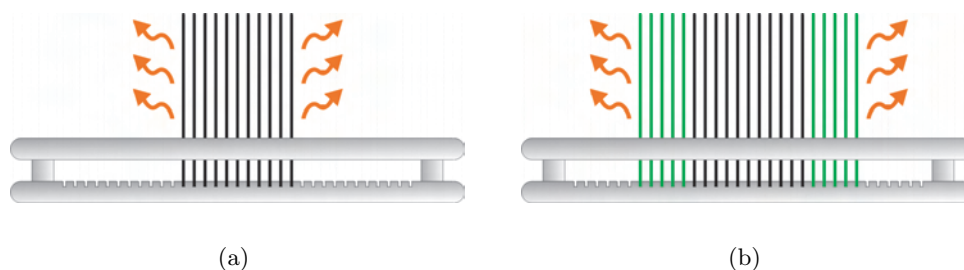
Figure 4.9: During thermal oxidation the outer wafers in the quartz boat (a) can radiate heat which results in a thinner oxide. This can be prevented by adding dummy wafers (marked green) as in (b).

the oxide defined process. Thus a variation across the wafer was expected as well as the depth of the channels in the rainbow arrays were expected to differ from each other. But Dektak scans revealed a surprisingly good uniformity on wafer scale and for the different channel widths. The variation from narrowest to widest channel in the order of 25 nm. On wafer scale the uniformity was estimated to be within approx. 50 nm.

4.4.3   SEM characterization

The final characterization using SEM on the bonded and diced wafers turned out to be very hard to perform, which can also be seen from Table 4.1. Due to charge up of the dielectric materials it turned out to be extremely difficult to get sharp and useful images. Furthermore the dicing process can also cause chunks to be removed in the interface between pyrex and silicon, which will thus not be in the same plane. This also complicated simultaneous focusing on both materials. In Fig. 4.10 an example of a 3.4 μm and a 100 nm channel is shown. The 100 nm channel is the widest channel from a rainbow array, and if the measurement can be trusted these show a slight collapsing of the channel. The focusing problem is clearly seen, and this makes height determination from the SEM relatively inaccurate and unreliable.

Therefore the height characterization is primarily based on the Dektak scans, although these do not give information about eventual collapses of the bonded channels.

4.4.4   Odd phenomena and process variations

An odd phenomenon that occurred, is that it was possible to see the overlap between the nanochannel photolithography process and inlet channels, as seen in Fig. 4.11, although this is expected to be impossible with the employed process. This was observed both before and after the dry etch. A profile scan along the inlet structure in a chip with 900 nm channels revealed protrusions of approximately 80 nm in the bottom of the 22 μm deep channel.

A possible explanation for the appearance of these protrusions can be found in the

(a)   (b)
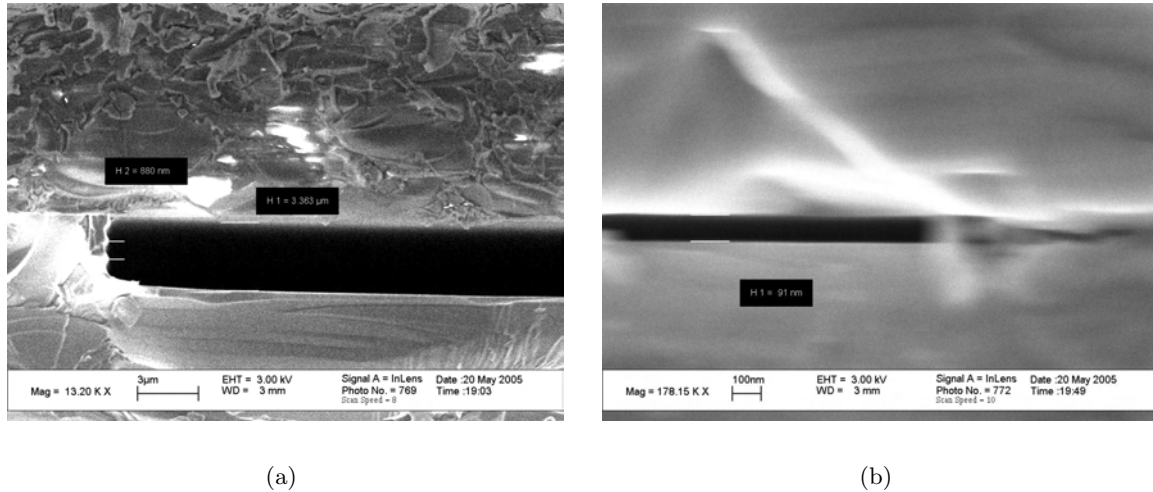
Figure 4.10: SEM of channel heights. (a) 3.4 μm channel showing $h = 3363$ nm. (b) 100 nm channel showing $h = 91$ nm. The lines are very blurred due to the charge-up of the dielectrics and the height cannot be measured with accuracy.

photolithography process. As the refraction of the UV-light in a resist spun on oxide differs from one on silicon, it is possible that a small monolayer has been left in the overlap between nanochannel mask and inlet channel mask. This monolayer combined with the native oxide underneath can thus retard the dry etch slightly leaving the observed

(a)   (b)
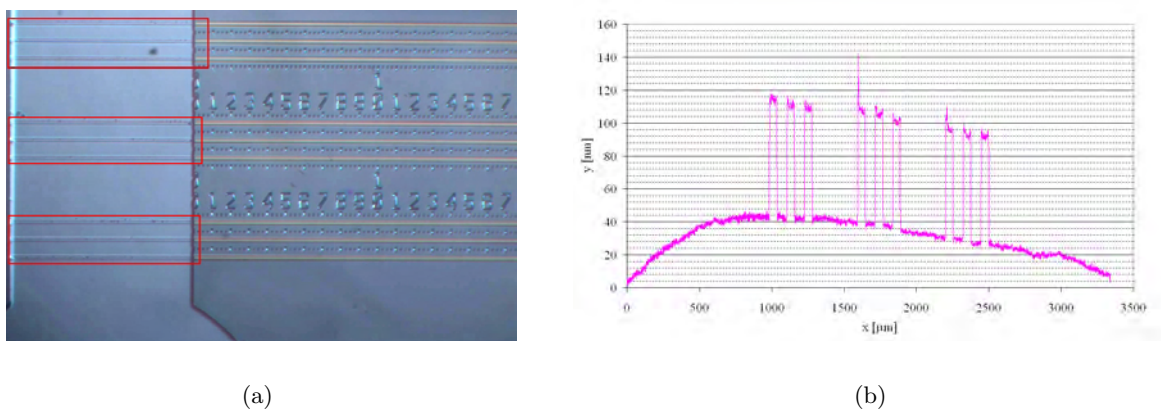
Figure 4.11: In (a) the overlap from the nanochannel photolithography process is still apparent in the 1 mm wide inlet channel of a 300 nm chip as marked by the rectangles. A Dektak scan (b) in the inlet structure of a 900 nm chip reveals protrusions in the bottom of the channel.

protrusions in the bottom of the channel. The only batch where the protrusions were not observed, was the first and previously described mysterious batch.

However, the protrusions have no influence on the characteristics of the devices no matter what has caused them to appear.

As mentioned in Sec. 4.3.1 the backside oxide is removed in the first etch step. Due to extensive bonding problems which will be described in Chap. 6, the backside oxide was protected in the second batch in order to investigate, if this could improve the bonding process. This turned out not to be the case, and the only consequence of the protection was a heavily complicated process with an increased risk of damaging the nanochannels.

4.5   Summary

Both the test batches and the new design showed excellent results concerning the silicon fabrication. Disregarding a few unexplainable deviations from simulations, the process sequence generated extremely uniform and reproducible results with nanometer precision on wafer scale with a yield of 100%. The fabrication resulted in channel heights of 3.4 μm, 925 nm, 310 nm, 100 nm, 42 nm, 32 nm and 25 nm.

Chapter 5

Lid fabrication

To close off the nanochannels a pyrex wafer is bonded to the substrate. In order to ease the filling of the channels the inlet holes need to be made in the lid, and several methods can be used to make these holes. From the test batch it was seen that drilling the holes after bonding was not a possibility since cooling water entered the channels during the process. Water droplets were still trapped inside 500 nm channels after having tried to evaporate it out for 3 days at a temperature of 250°C. In addition the SiO_2 at the channel bottom was shaded and had changed color in some regions. Another reason for not using this method on the wafers prior to the bonding is that it is rather violent, and hence the wafers would easily break. Especially when considering that 104 holes must be made in each pyrex wafer, it is not likely that any whole wafers could be produced.

5.1 Etching of holes

Originally the plan was to etch the holes using a 40% HF solution. This way all holes on the wafer are made simultaneously with no risk of cracking in contrast to the drilling method. To mask the pyrex wafer, self-adhesive 70 μm blue SWT 20 Nitto tape is used. It is applied to both sides of the wafer making sure that the edges are well protected. A CO_2 laser is used to ablate the film where the inlet holes are to be made. The coordinates, with respect to the wafer center, are taken out from the L-edit file, and the software WinMark is used to make the layout file which controls the laser. The laser uses 12 passes at 200 mm/s and 10% power (15 W) to shoot app. 100 μm down in the pyrex. One pass is enough to remove the film, but ablating some of the pyrex shortens the etch time and reduces the mask underetch.

The HF solution has an etch rate of 3 μm/min in pyrex [17], so 2:30 h to 3:00 h are needed to make the holes. To check if the etch process is thoroughly done, the blue film at the back of the holes and possibly a thin layer of glass is broken by a sharp pair of tweezers.

HF is an isotropic etch, and hence the holes will be spherical with large mask underetch. The upper diameter of a hole through the wafer is twice the thickness plus the 300 μm diameter of the laser ablated hole.

Both the intense laser treatment and the etch are likely to induce stress in the wafer. This might be the reason that fusion bonding of pyrex with HF etched holes seems to be impossible. At any rate we did not succeed in bonding any of them, while dummy pyrex wafers bonded easily. This is why the fabrication method was changed.

5.2   Powder blasting of holes

A relatively new fabrication tool in microtechnology is powder blasting. Widely used for dental applications the powder blast tools, which are also useful for micromachining, are cheap and easily available.

5.2.1   Equipment

The equipment used to blast the holes is the Microetcher II$^{\text{TM}}$ and a dust cabinet shown in Fig. 5.1.

The blasting material used is particles of Al_2O_3 which comes in different sizes. 50 μm and 90 μm particles were used and seem to give the same result. In the microetcher tool pressurized air (6-7 bar) sucks up the alumina particles from a reservoir and emits them through the nozzle at speeds on the order of 100 m/s as shown in Fig. 5.2(a). When a brittle material, such as pyrex, is hit by the very sharp edges of the particles, a high compressive stress is introduced and the contact area is plastically deformed. The following relaxation after the impact causes high tensile stress, which makes the surface crack off

(a)   (b)

Figure 5.1: Equipment for powder blasting. (a) Microetcher. Pressurized air sucks up the blasting material from the reservoir and emits it at high speed through the nozzle. (b) Dust cabinet equipped with light and filtered extraction reduces the amount of dust leaked to the surroundings. Pictures from [19] and [20] respectively.
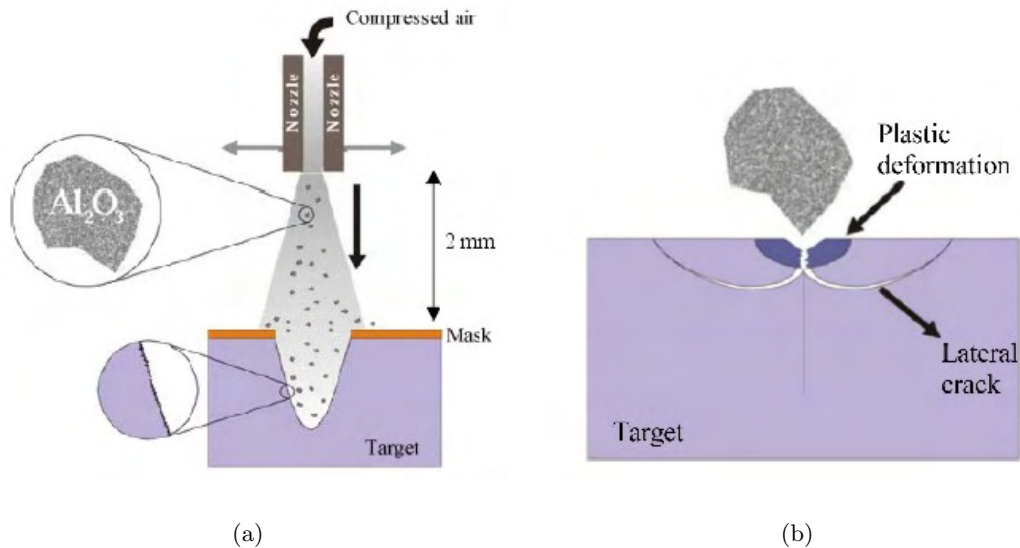
Figure 5.2: Working principle for powder blasting. (a) Setup. (b) Powder blast works only on brittle materials which crack off when exposed to the. Figures taken from [16]

.

in pieces as shown in Fig. 5.2(b). The surface roughness is on the order of 1 μm . Metals and elastomers erode in different ways and have much smaller etch rates [16].

5.2.2 Method

Since the powder blast particles spread out when emitted from the nozzle the etcher can not be used directly on the wafer. A mask is needed to create well-defined structures and to protect the remaining surface from the dust.

First attempt included a metal plate with drilled holes, which is suggested in [16] as one of the masking possibilities. But very fast it became clear that this did not work at all. The 2 mm brass plate was too thick compared to the 500 μm drilled holes, so only a very small amount of the emitted blasting particles reached the wafer surface at the end of the hole, resulting in a very low etch rate. Also voids between the plate and the wafer allowed the particles to damage the wafer surface. The article suggests the use of a hard wax to solve this problem, but instead we discovered a far better solution to the mask problem.

The same article also mentions that some special polymer films are useful due to the erosion by fatigue mechanisms with very low blasting etch rates. However they are all applied in liquid form and patterned through lithographic processes in the cleanroom, and making a lithography mask and developing a process recipe would be time consuming. By a lucky punch it was decided to test the masking properties of the blue Nitto tape used for the HF etch, which in fact turned out to be a nearly perfect mask. The pyrex wafer was

(a)   (b)
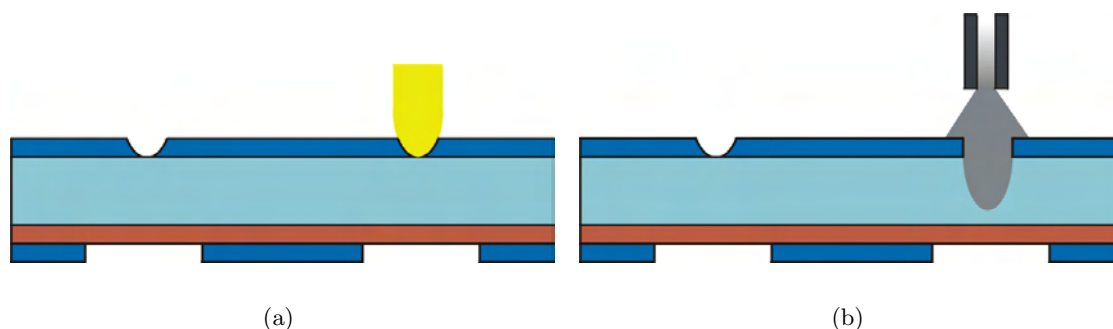
Figure 5.3: Cross sectional view of the lid fabrication process. In (a) the mask is defined in blue film by CO_2-laser, and in (b) the holes are subsequently made in the pyrex by powderblasting.

prepared in exactly the same way using the laser to ablate the film where the holes were to be, this time using only 1 pass of the beam. By placing the nozzle of the microetcher at a distance of a few milimeters above the wafer it took less than 30 s to make a very fine hole.

However mask holes are also needed at the back side since the high pressure of the compressed air will lift off the film when it breaks through the pyrex and allow particles to scratch the backside. Since accurate aligning in the CO_2 laser is not possible, only the front side of the pyrex was covered with blue film, and the holes were ablated as shown in Fig. 5.3. Afterwards slightly larger mirrored holes were made on a piece of film which was then aligned to the holes on the front side and applied to the pyrex.

To give an extra protection of the bonding side, 4.2 μm resist was spun on and hard-baked before the application of blue film, as we observed minor scratches in the backside without resist. In Fig. 5.4 the slightly conical powder blasted holes are shown, and the usefulness of the resist protection is also illustrated.

Clean surfaces are crucial for fusion bonding and since the powder blasting produces a lot of dust, thorough cleaning of the wafers is necessary before they are taken back into the cleanroom. Most of the dust is removed with a moist tissue, and the rest comes off with the blue film. When the wafers are brought into the cleanroom only the dust on the resist surface in the vicinity of the holes is remaining, and this is easily lifted off in acetone. Finally the wafers are cleaned in DI water with bubbles and spin dried before the bonding processes.

5.3   Summary

All in all it can be concluded that the powder blast method gives very good results. It is a fast process which is easy and cheap to use. Furthermore the combination of laser and blue film allows the layout to be changed at any time without any costs.

<center>(a)</center>

<center>(b)</center>

<center>(c)</center>

<center>(d)</center>
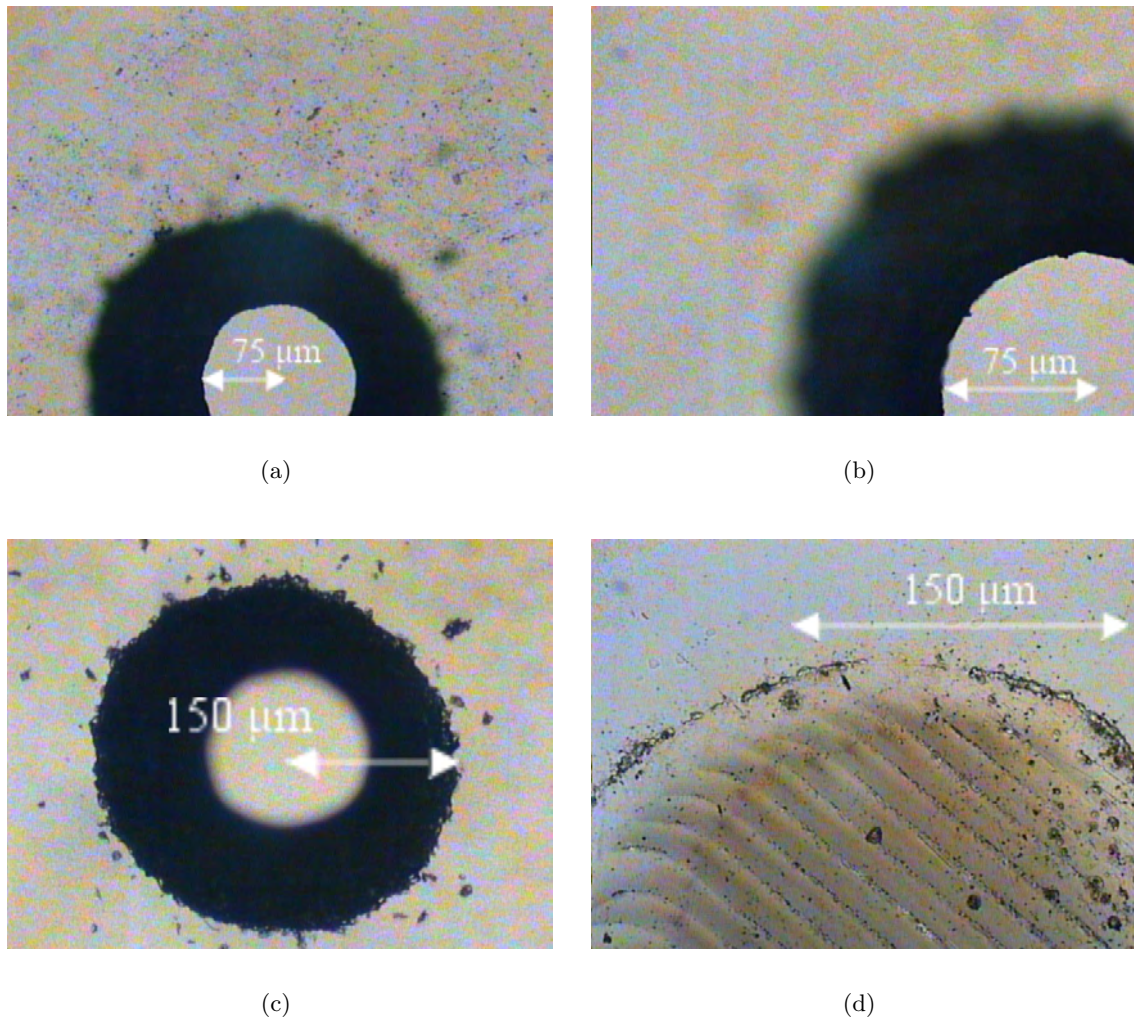
Figure 5.4: Holes in pyrex wafers. (a) Powder blasted hole seen from the bonding side (small hole). The surface is scratched since no resist has been used to protect it. (b) This wafer has been protected by a resist layer before powder blasting and no scratches are present. (C) Hole seen from the blasting side. The powder has penetrated the masking film in a few spots around the hole. (D) When the masking film is ablated the laser also removes some of the pyrex underneath.

Chapter 6

Bonding

The process of bonding the pyrex lid to the substrate can be done in several ways, but due to the extremely small dimensions of the channels and the high aspect ratio it is important to chose a method, that does not cause the channels to collapse. Anodic bonding is a very commonly used technique, but for shallow channels it is not useful since the electric field will induce electrostatic forces, which can partially close the channel as sketched in Fig. 6.1, [12]. A better solution is to use a KOH based fusion bonding.
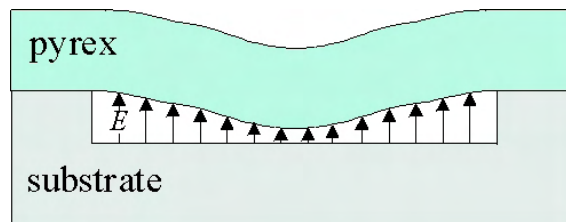
Figure 6.1: An electric field across a shallow channel will induce electrostatic forces which can partially close the channel. Adapted from [12, Fig. 1(a)] .

6.1   Principles of KOH Bonding

Litterature on the KOH bonding specifically has not been available, but from a couple of articles ([10], [11]) describing the broader term fusion bonding, it has been possible to put together a picture of the fundamental mechanisms which occur during the bonding process.

Fusion bonding works between any two mirror polished, clean surfaces, which are either both hydrophillic or both hydrophobic. When brought in contact, van der Waals forces attracts the two surfaces to each other and bond them together.

The first step of the KOH bonding recipe is a piranha treatment for cleaning the wafers to make sure that no organic substances are present and only a minimum of particles. During the subsequent KOH step the surfaces of both the pyrex and the SiO_2 are slowly etched and rendered hydrophillic by placing OH-groups on the surface silicon atoms of the
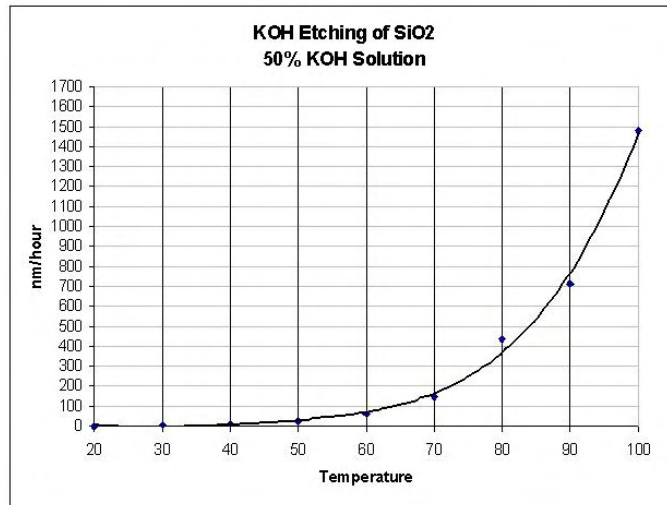
Figure 6.2: Etch rate in SiO_2 for 50 wt% KOH. Figure from [18].

oxides as shown in Fig. 6.3(a). The previous acid treatment in piranha is likely to increase the surface density of the OH-groups.

The etchrate of KOH in SiO_2 increases exponentially with temperature and is expected to be between 1 nm/min and 7 nm/min in the temperature range we primarily used, see Fig. 6.2.

After the KOH etch and spindrying the lid and substrate are aligned with a few millimeters space, and the bonding is initiated by pressing the wafers together locally with the thumbs. The bonded area will then quickly spread over the entire wafer. When the two wafers are brought into contact, hydrogen bridges between the OH-groups of both wafers are formed as illustrated in Fig. 6.3(b). Some of the OH-groups will react with each other and form a stronger strained Si-O-Si bond, while an H_2O-molecule is produced. The average bond energy of this prebonding is on the order of $\gamma = 20$ mJ/m^2 [12].

(a)   (b)   (c)
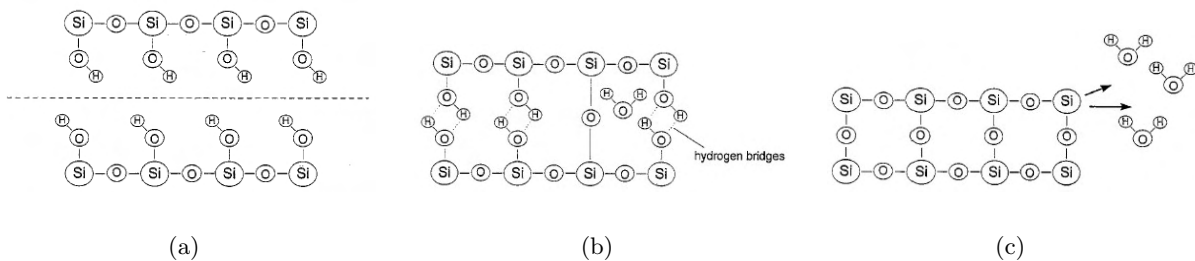
Figure 6.3: Principle of KOH bonding. (a) Surface states after KOH treatment. (b) Hydrogen bridges and water formation during prebonding. (c) Silicon-oxygen-silicon bonds after annealing. All figures are from [10].

The prebond is very weak and the wafers can easily be detached again. In order to increase the bond energy the wafers need to be annealed at high temperature. One possible explanation for this is that four H_2O-molecules tend to form a ring around the two hydrogen bridged OH-groups. These rings keep the surfaces at a distance of 0.35 nm, and since the ring of H_2O-molecules has a diameter of 0.4 nm, it cannot easily diffuse away. A strong Si-O-Si bond has a distance between the silicon atoms of only 0.16 nm, and the strained Si-O-Si bonds can rehydrate when water is present. This can explain why the water needs to diffuse away from the surface interface to let strong bonds be formed, Fig. 6.3(c). The higher the density of OH-groups, the less water will be present, and the better the prebonding will be [10].

Bonded wafers annealed at temperatures in the range of 300°C to 500°C will have an average bond energy of $\gamma = 200$ mJ/m^2 [12]. High temperatures (>600°C) are needed to break up the water rings surrounding the OH-groups [10]. The process recipe used at MIC includes the annealing temperature profile shown in Fig. 6.4, with a maximum temperature of 550°C. However, an article [12] claims that this is too high, since the temperature should always be lower than the strain point of pyrex at 510°C. The thermic expansion coefficients of the bonded wafers must be sufficiently close for the annealing to be possible. The values for silicon and pyrex are $\alpha_{l,Si} = 2.4 \times 10^{-6}$ K^{-1} and $\alpha_{l,Pyrex} = 3.2 \times 10^{-6}$ K^{-1}, [8].
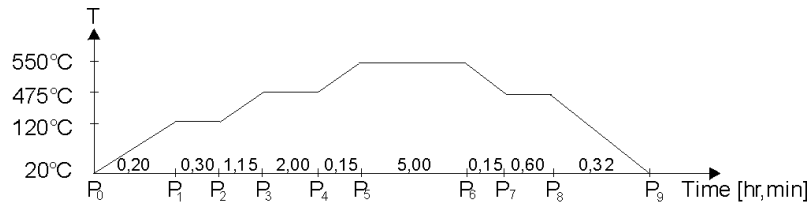
Figure 6.4: Annealing temperature profile.

6.2 Performed bonding process

As the used literature only describes general fusion bonding, the above stated principles are not understood in such great detail that a process recipe including specific times and temperatures can be derived. Variations in concentration and temperature of the KOH solution have dramatical effects on the etch rate in SiO_2, but information on this related to the bondability of the wafers is not available. Therefore the KOH process used at MIC was accepted without reservations. It includes

- 10 min hot Piranha (20% H_2O_2, 80% H_2SO_4)

- 10 min rinse in DI water with bubbles

- 2 min 30 sec etch in 50 wt% KOH (no temperature given)

- 10 min rinse in DI water with bubbles

- Spindrying (perhaps including another rinsing step)

- Bonding

When made, the KOH solution will reach a temperature of approx. 90°C due to the chemical reaction with water. At this temperature the etch rate in SiO_2 is app. 10 nm/min. To protect the thin bottom oxide, which for the first batch was only 20 nm and therefore on some wafers etched through, most KOH processes were done at temperatures less than 75°C with etch rates under 4 nm/min.

As mentioned in Sec. 5.1 the first batches had lids with HF etched holes. Though following the process recipe in great detail no successful bondings were ever made with this type of lid. However perfect bondings of dummy pyrex to dummy SiO_2 wafers and dummy pyrex to substrate with channels were made with ease. Obviously the surface activation took place, but for some reason only the lids with holes would not bond. This led us to start considering another manufacturing method of the lid.

At first the change to powder blasted holes seemed to have solved the bonding problem, since it worked perfectly with the 100 nm test batch. However the problems reoccured when trying to bond the new designs with the same tendency that only pyrex wafers without holes were easily bonded without exception. As the bonding process was not fully understood, it was hard to determine which factor caused the trouble. Therefore this step in the fabrication delayed the project for several weeks and resulted unfortunately in a fairly high loss of wafers.

6.2.1   Types of bondings

To a greater or lesser extent we observed that three different things can happen when pressing the wafers together for prebonding:

No bonding. When the wafers are brought into contact a bonding area surrounded by Newton rings is formed in the middle of the wafers, where the pressure is applied. The bonded area does not spread out, but by moving the thumbs it can be enlarged. It is, however, not stable but slowly diminishing and the Newton rings are steadily moving towards the center of the wafers as soon as the pressure is released. In a matter of 30 seconds the wafers have let go of each other. Some times the surfaces do not seem to be activated and no bonding area occurs or it disappears immediately when the pressure is off.

Bonding type 1. When the wafers are pressed together the bonding area immediately starts to spread out. To make it cover the entire wafer area it is necessary to move the thumbs to apply the pressure everywhere. The bonding is stable and only close to the edges (5 to 10 mm) there is no bonding. The Newton rings are close and regular, see Fig. 6.5(a). Voids due to particles on the surfaces can occur, but it will only cause a small local defect.

Bonding type 2. The wafers start to bond where the pressure is applied, but the bonding area does not spread. The Newton rings are blurred and not well defined opposed to the

type 1 bonding, see Fig. 6.5(b). By working hard on the wafers and wriggle them a bit the bonded area can be enlarged, but it is still blurred, voids occur, and the edge of the area is not well defined. However this type of bonding is stable and does not change if the wafers are left for a week. When trying to separate the wafers it does not happen smoothly, as for the type 1 bonding, but with a cracking sound, signifying that some strong bonds are broken. After annealing, the type 2 wafers are only bonded in very small areas, on the order of 1 cm^2. Sometimes the prebonding can look really good on most of the wafer surface, but the Newton rings at the edge are still blurred and there is no bonding after annealing.

An overview of the different parameters and bonding result is given in App. E.

| (a) | (b) |
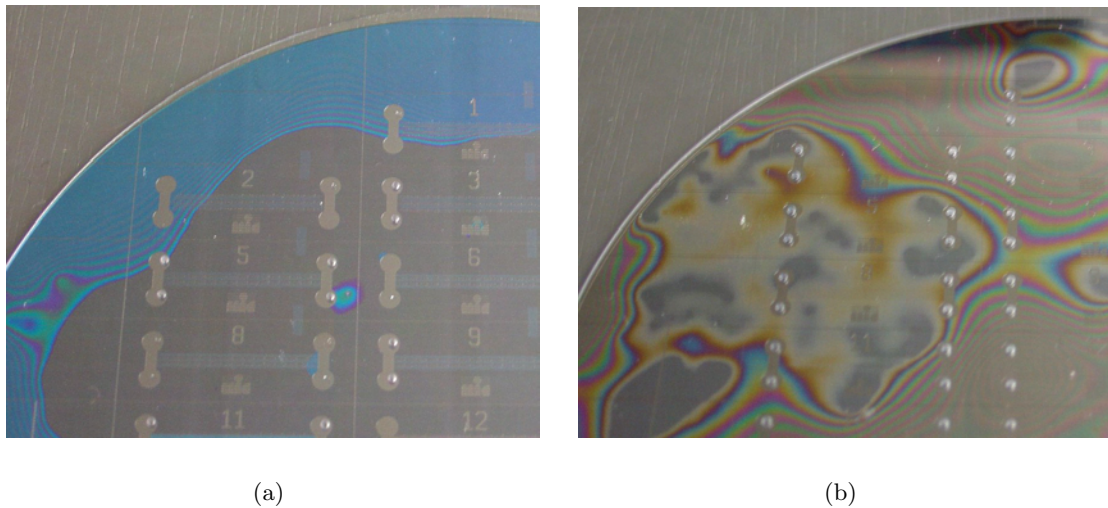
Figure 6.5: Bonding types. (a) Type 1 bonding after anneal. Newton rings are close and well defined. (b) Type 2 bonding after anneal. Newton rings are distant and blurred, and the wafer is only bonded in small areas.

6.2.2 Failure mechanisms

Several mechanisms can obstruct the bonding, and an obvious one is stress in the wafers. During the processing the thick oxide is removed from the backside. Since the stress in a SiO$_2$ film on silicon is compressive, the wafer will tend to be convex (edges are bending down). However, Dektak scans to measure the stress in some of the wafers showed that these wafers were concave (center is bending down), see Fig. 6.6, and the magnitude of the bending was on the order of what is seen for unprocessed wafers. Thus stress in the substrate is no problem, and since the substrates seems to always bond perfectly with dummy pyrex, it is easy to conclude that the problems probably are caused by the pyrex.
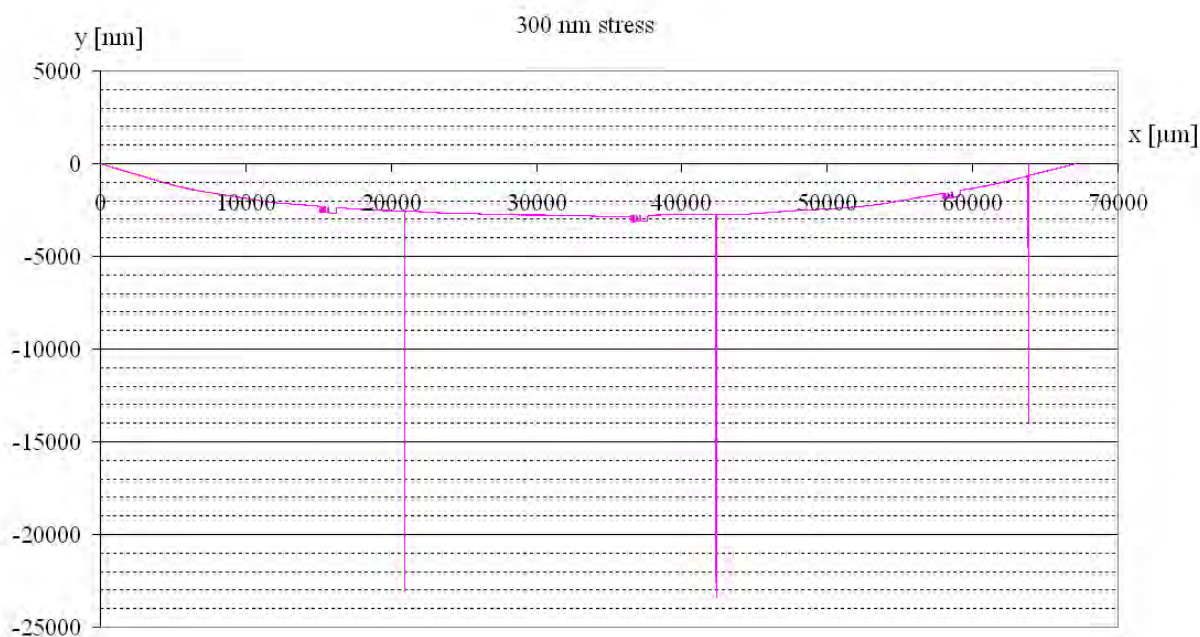
Figure 6.6: Stress in a wafer with 300 nm channels. The deep horizontal lines are 20 μm saw lines and the small trenches are the channels. The bend is 3 μm.

When the same measurements were carried out on the pyrex wafers there was a clear difference between wafers with and without holes. Fig. 6.7(a) shows a scan across a pyrex wafer with no holes. The bending is seen to be big (11 μm) but smooth. Fig. 6.7(b) shows the stress in a pyrex wafer with powder blasted holes. The scan is made between the holes parallel to where the nanochannels will subsequently be bonded, approx. 5 mm from the holes. The fluctuations of the line may arise from local stress around the holes, and the horizontal lines show the periodicity of the powder blasted holes across the wafer, which somewhere seems to fit the fluctuations nicely. Anyhow not all of the fluctuations fit and there is no clear correlation. Any local stress could maybe be explained by the fact, that the powder blasted holes are conical and hence more material has been removed from one of the sides. However, local scans near the holes did not reveal any significant stress.

Whether or not the stress causes the trouble is hard to conclude, but a tendency that the bonding works fine with dummy pyrex and worse with holes in the lid was observed. Reducing the number of holes was also tried to improve the bonding. This worked in one case but not in another.

The temperature of the KOH solution might also play a significant role, since it is responsible for the surface activation. A look at Table E.1 in App. E shows however that the good bondings have been made at very different temperatures ranging from 51°C to 86°C. It is observed that bondings with temperatures less than 65°C only succeeded for channel heights less than 100 nm. To test the time dependence some pyrex wafers were
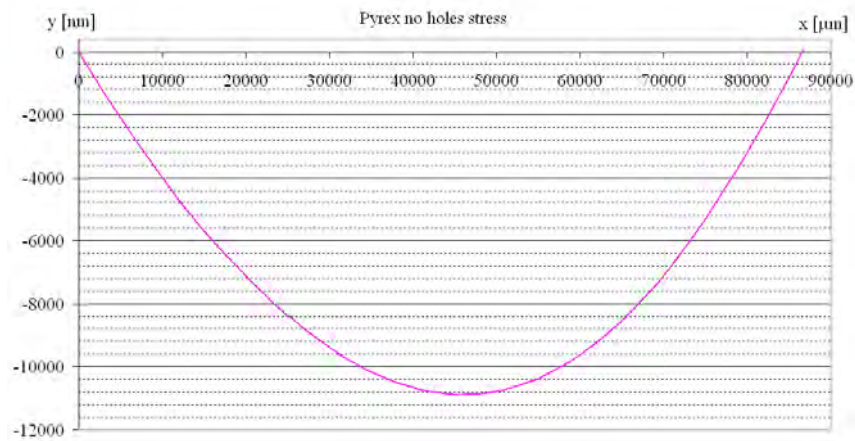
(a)
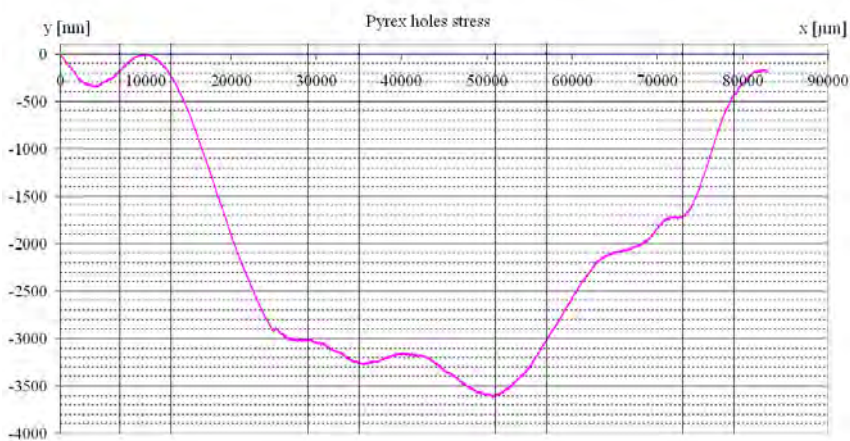
(b)

Figure 6.7: Stress in pyrex wafers. (a) Stress in a pyrex wafer with no holes. The bend is 11 μm. (b) Stress in a pyrex wafer with holes. The scan is made between the holes parallel to where the nanochannels will subsequently be bonded . The fluctuations of the line may arise from local stress around the holes. The horizontal lines show the periodicity of the powder blasted holes across the wafer. The overall bend is 3.5 μm.

given 10 min of KOH, but none of them bonded, so it is not likely that longer times will increase the bondability.

In Fig. 6.8 SEM pictures of the bonding interface are shown. It is seen that there are

(a)   (b)
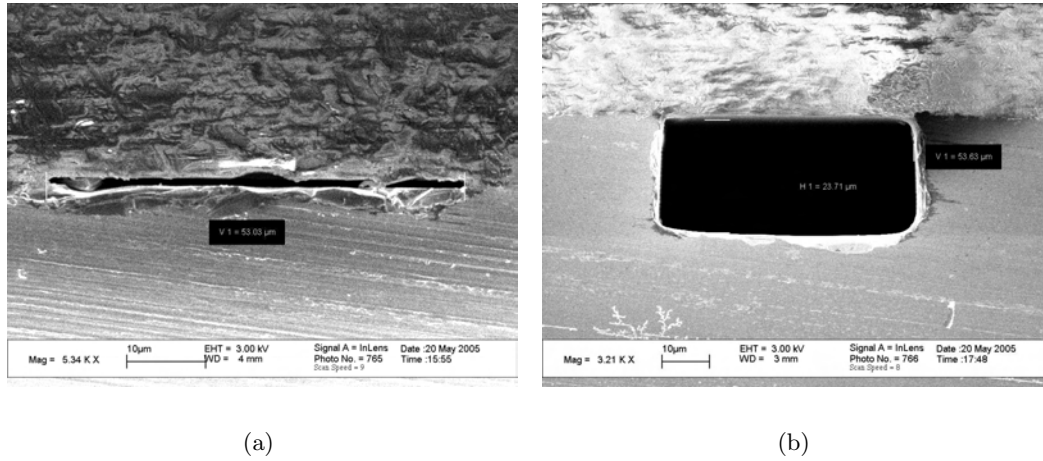
Figure 6.8: SEM of bonding. (a) 900 nm 50 μm channel. (b) 20 μm deep saw line.

no voids outside the channel, which means that the bonding is very tight when succeeded.

The bonding process has been the far most unreliable and troublesome part of the fabrication and the only real source to loss of devices. Despite systematically varying the temperature and time, no clear indication of what could improve the bonding was found. It was only observed that bonding lids with holes heavily complicated the process. Therefore further investigations must be made on how to improve the bonding process.

Chapter 7

Measurements

Two types of measurements need to be done. The primary ones are carried out on the device to investigate the capillary flow, and the secondary ones are necessary to determine certain physical properties of the liquids in order to be able to compare the primary measurements with the theory. The group of secondary measurements includes the contact angle of the liquids with pyrex and SiO_2, the surface tension, the pH, and the conductivity.

7.1 Choice and properties of the liquids

As mentioned in Sec. 1.2 one of the goals is to investigate if an electroviscous effect can be seen, as it is reported by N.R. Tas *et al.* [9]. Therefore the liquids used for the filling experiments are chosen to have different electrical properties but similar properties regarding surface tension, viscosity and contact angle. Using aqueous solutions of a given salt, the Debye length λ_D and conductivity σ_{el}, which are of importance for the electroviscous effect, are easily adjusted, as they both depend on the concentration. For increasing concentration the Debye length decreases, given by Eq. (2.27), and the conductivity increases.

It was decided to use Borax solutions, since they are well-defined and were easily obtainable. The Borax is primarily dissolved in water by the reaction

$$Na_2B_4O_7 + 7H_2O \longrightarrow 2H_3BO_3 + 2B(OH)^- + 2Na^+, \tag{7.1}$$

and thus one mole of Borax gives two moles of ions. Two concentrations were chosen; a 0.1 mM solution with a Debye length of 21 nm resulting in Debye overlap in the smallest channels, and a 0.1 M solution giving a Debye length of 0.7 nm and thus no overlap in any of the channels. These and other properties of the liquids are summarized in Table 7.1.

Besides Borax solutions, deionized water was used as well, as this has a Debye length yielding overlap for channels up to several 100 nm in height. The water was drawn from a MILLIPORE Milli-Q Gradient A10 system, and the Debye length is estimated from the concentration of H^+. Under normal conditions a given amount of CO_2 from the air is dissolved in the water thus forming

$$CO_2 + H_2O \longrightarrow H_2CO_3$$
$$H_2CO_3 \longrightarrow H^+ + HCO_3^-. \tag{7.2}$$
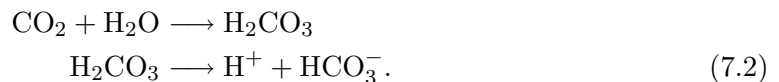
Liquid	Milli-Q	0.1 mM Borax	0.1 M Borax
γ [10^{-3}J m^{-2}]	72.8 ± 1.8	73.2 ± 1.5	73.6 ± 1.4
η [10^{-3}Pa s]	0.89 ± 0.02	0.89 ± 0.02	0.89 ± 0.02
σ_{el} [S m^{-1}]	$5.5 \times 10^{-6} \pm 5\%$	$2.0 \times 10^{-3} \pm 5\%$	$0.98 \pm 5\%$
pH	5.7 ± 0.1	8.5 ± 0.1	9.3 ± 0.1
c$_0$ [M]	$10^{-5.7} \pm 4 \times 10^{-7}$	$0.2 \times 10^{-3} \pm 5\%$	$0.2 \pm 5\%$
ϵ_{r}	78.36	78.36	78.36
λ_{D} [10^{-9}m]	215 ± 25	21 ± 0.5	0.7 ± 0.02

Table 7.1: Properties of the liquids at 25°C.

The determination of the H$^+$ concentration was carried out by measuring the pH-value and using $c_0 = 10^{-\mathrm{pH}}N_A$. Measurements were carried out with a Radiometer PHM210 STANDARD pH METER on DI-water stored for $2\,^1/_2$ month, $1\,^1/_2$ month and directly drawn water yielding pH values of 5.78, 5.61 and 5.70 respectively. Thus no direct correlation between storage time and pH was observed, and λ_D was estimated on base of the mean value pH = 5.7 giving $\lambda_D = 215$ nm. The uncertainty on pH results in an uncertainty on λ_D of 25 nm.

The conductivity of the two solutions was measured with Radiometer CMD210 Conductivity Meter. For the Milli-Q water the conductivity was given directly from the MILLIPORE system. In both cases the uncertainty is estimated to 5%.

The surface tension was measured for all three liquids with a Krüss Drop Shape Analysis System, DSA 10 Mk2, analyzing the shape of a pendant drop. The values for all liquids were found to be very close to the handbook value 72×10^{-3} J m^{-2} [7, **6**-135].

Regarding the viscosity η, this has not been measured as no suitable set-up was available, and time did not allow for the building of such. Therefore is was merely taken as the handbook value $\eta = 0.890 \times 10^{-3}$ Pa s, [7, **6**-186], for water at 25° which was close to the average temperature at which the experiments were carried out. In [9] it has been reported that a 0.1 M NaCl increases η by 1.0%. It is supposed that the same order of magnitude applies to Borax solutions, and the estimated uncertainty due to the dependence of temperature variations covers for this anyway.

The final parameter is the permittivity ϵ. The value of this is not fully known for any of the liquids under the conditions encountered in the channels, where e.g. the equilibrium electric field can result in a breakdown of the liquid in the EDL-region. Therefore the value has been chosen to the handbook value[1] for water being $78.36\epsilon_0$ [7, **6**-13].

7.2 Contact angle and surface tension measurements

Since the contact angle is needed in the theoretical predictions it is important to provide a reasonable estimate of it's value. It is known that the contact angle of liquids on a SiO$_2$ surface is not constant with time and depends on the surface treatments. Therefore at least one dummy wafer was placed in the furnace, along with each batch, during the growth of

---

[1]Chosen after advice from Ph.D. Student Anders Brask, MIC, DTU.

the final oxide layer. This was done to obtain contact angle values from a dummy, which had been exposed to the same surface treatments and stored under the same conditions for the same amount of time as the nanochannel wafers. To get a precise estimate for the contact angle in the nanochannels, the measurements on the dummy were planned to be done on the same day as the flow measurements were made.

The static contact angles are found using a Krüss Drop Shape Analysis System, DSA 10 Mk2, which during 10 s continuously makes a geometrical fit of a curve to a live picture of a droplet. Standard deviations are calculated from several curve fits on the same droplet and from repeated measurements.

Unfortunately, since all wafers in a batch were not bonded at the same time due to the bonding problems described in Chap. 6, it was not possible to let the dummies go through every bonding attempt as this would have made the KOH etch away all of the oxide. This made it impossible to produce dummy wafers with surfaces equivalent to the bottom of the nanochannels. Furthermore it was not expected that the nanochannels were exposed to as high an airflow as the dummies. This will probably imply that the oxide in the nanochannels does not change as much in the course of time as the oxide on the dummies.
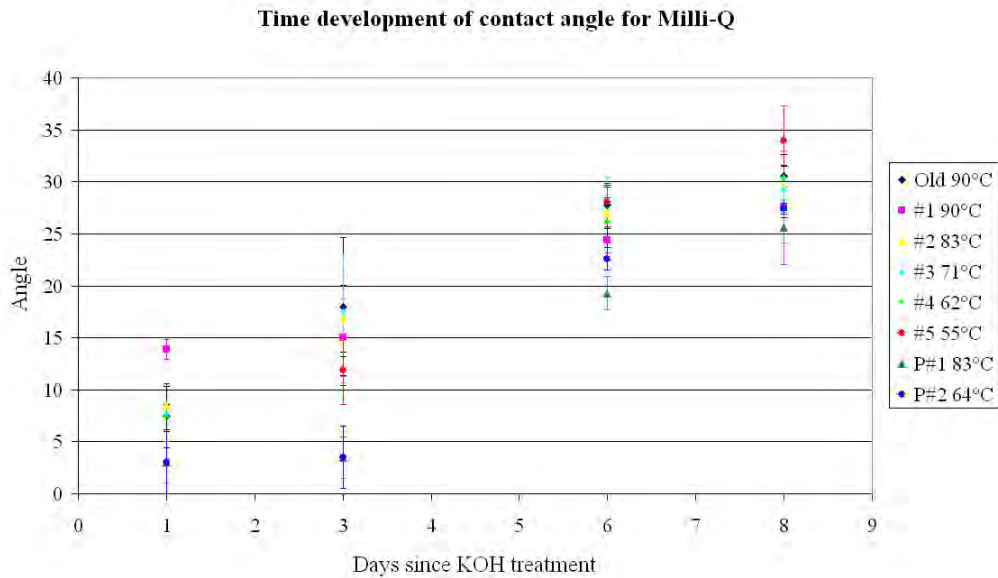
Figure 7.1: The contact angles of Milli-Q on dummies treated at different KOH temperatures. Old dummy refers to a Si wafer which had a time-span of 30 days between growth of final oxide and KOH etch.

Somehow the angle had to be estimated, and therefore it was decided to make a more thorough and systematic investigation on how the KOH temperature and time affected the contact angles. This implied measurements performed with different time intervals, on a dedicated contact angle dummy batch treated with KOH at different temperatures in the range of 55°C to 90°C.

A plot of such measurements can be found in Fig. 7.1. It is readily observed in the figure that there is a huge time dependence on the contact angle, which seems to be increasing somewhat linearly. From day 1 to day 8 after the treatment the angles increase from approx. 5° up to approx. 30°. The mutual order of the measurements on *Dummy #1* to *Dummy #5* interchange through time. Since this is observed for all three liquids, it implies that no temperature dependence can be detected. Furthermore, a 30 days old dummy treated with KOH the same day as the freshly oxidized dummies gave contact angles of same size as the dummies. This indicates that the storage time from oxidation to KOH treatment is of no importance, as the KOH etches a new surface.
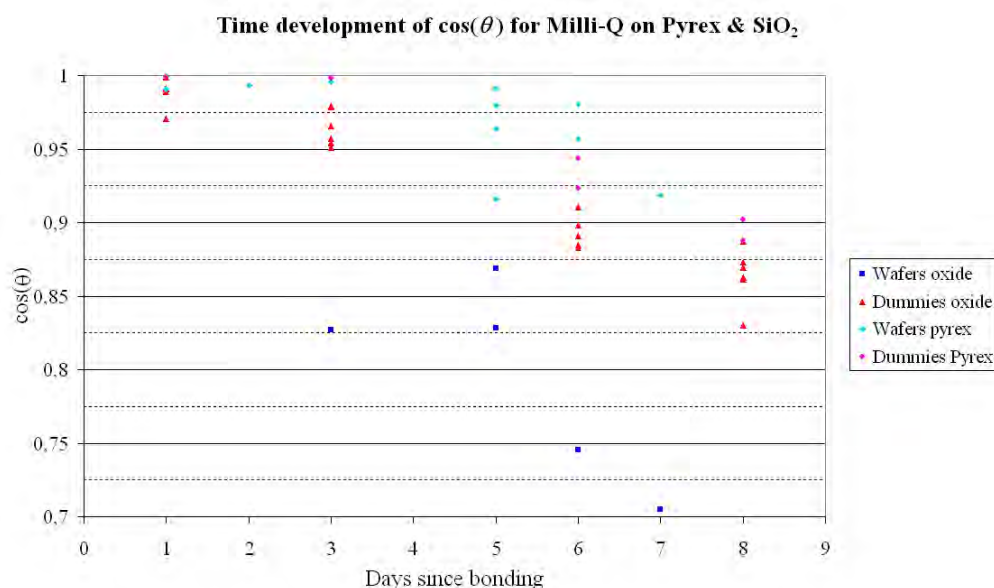
Figure 7.2: All measurements obtained for $\cos\theta$ on different surfaces for Milli-Q. Since the values of the wafer oxide differs very much from the rest, they are condired as outliers and are not used for the average. These data come from the thick oxide, which is often a wet oxide whereas the bottom oxide is a dry one, and therefore it can not be expected to give the same result.

Since $\cos\theta$ is the relevant physical parameter, this has been plotted in Fig. 7.2 for all measurements of water on pyrex and SiO_2. The values of the *Wafers Oxide* are seen to be much different from the rest. These measurements are made on top of wafers with a thick oxide, which for some of the wafers is grown in a wet ambient, whereas the thin oxide is made in a dry. Hence these values are excluded for the estimation. Despite the time dependence, a total estimate was made on the contact angle for each liquid by calculating the average of all measurements conducted with the given liquid, using the standard deviation as uncertainty. This was done, since it would be impossible to obtain a value accounting for all the prior mentioned effects, such as less exposure to air in the nanochannels. Furthermore the contact angle varied depending on where it was measured on the wafers. Only values obtained in the interval between 2 and 7 days were used, since

	$\cos \theta$	Uncertainty
Milli-Q	0.96	$\pm$ 0.03
0.1 M Borax	0.98	$\pm$ 0.02
0.1 mM Borax	0.92	$\pm$ 0.06

Table 7.2: Estimates of $\cos \theta$.

all flow measurements were performed in this interval.

Since there are two different materials at the bottom and top with two different angles, the average of $\cos \theta$ for each material should be used to calculate the total average,

$$\cos \theta = \frac{\cos \theta_{\text{pyrex}} + \cos \theta_{\text{oxide}}}{2}. \tag{7.3}$$

The estimated values of $\cos \theta$ for the different liquids are given in Table 7.2.

7.3 The setup

Since the nanochannels were ranging from 20 μm to 500 μm in width a microscope was required in order to do an optical detection of the meniscus. Furthermore, a judicious way of collecting and analyzing the data was also required, since the channels were filled too fast to read off data during the measurement. Therefore a Leica DFC 280 digital camera was mounted on one of the channels of a stereo microscope, which made it possible to record the measurements on the computer hard drive with Leica IM50 acquisition software for subsequent analysis.

As the field of view in the microscope was only a few millimetres wide, the chip had to be moved during the measurements, since the nanochannels are 15 mm long. This problem was solved by using a stage which could move parallel to the nanochannels. Unfortunately, the software did not allow the user to observe the movie being recorded while the recording was in progress, so the advancing meniscus had to be surveyed using the free ocular of the microscope. This lead to vast problems adjusting the light source as both channels of the microscope had to be supplied with sufficient light. Pictures of the setup including camera, stage and light are shown in Fig. 7.3.

Originally is was the intention to have the wafers diced before commencing the measurements. However, the circular saw, used for dicing the wafers, was out of order, so this was not possible. After all this did not turn out to be a problem since the stage could support the entire wafer without any problems, though one had to be careful only to load one chip at a time since the inlet holes of the chips were placed no more than 5 mm apart. Mixing of the fluids from two different measurements should be avoided, so inlet holes as far apart as possible were selected if there was any risk of mixing with residues of fluids from measurements on neighbouring chips. For each measurement, the temperature was measured on top of the substrate.

In order to minimize contamination of the wafers these were kept in single-wafer carriers until the measurements were conducted, and moreover any handling of the wafers and liquids was carried out wearing gloves. For the same reason the liquids were stored in tightly closed glass bottles, and the sterile syringes used for loading were regularly changed.

(a)   (b)

(c)   (d)
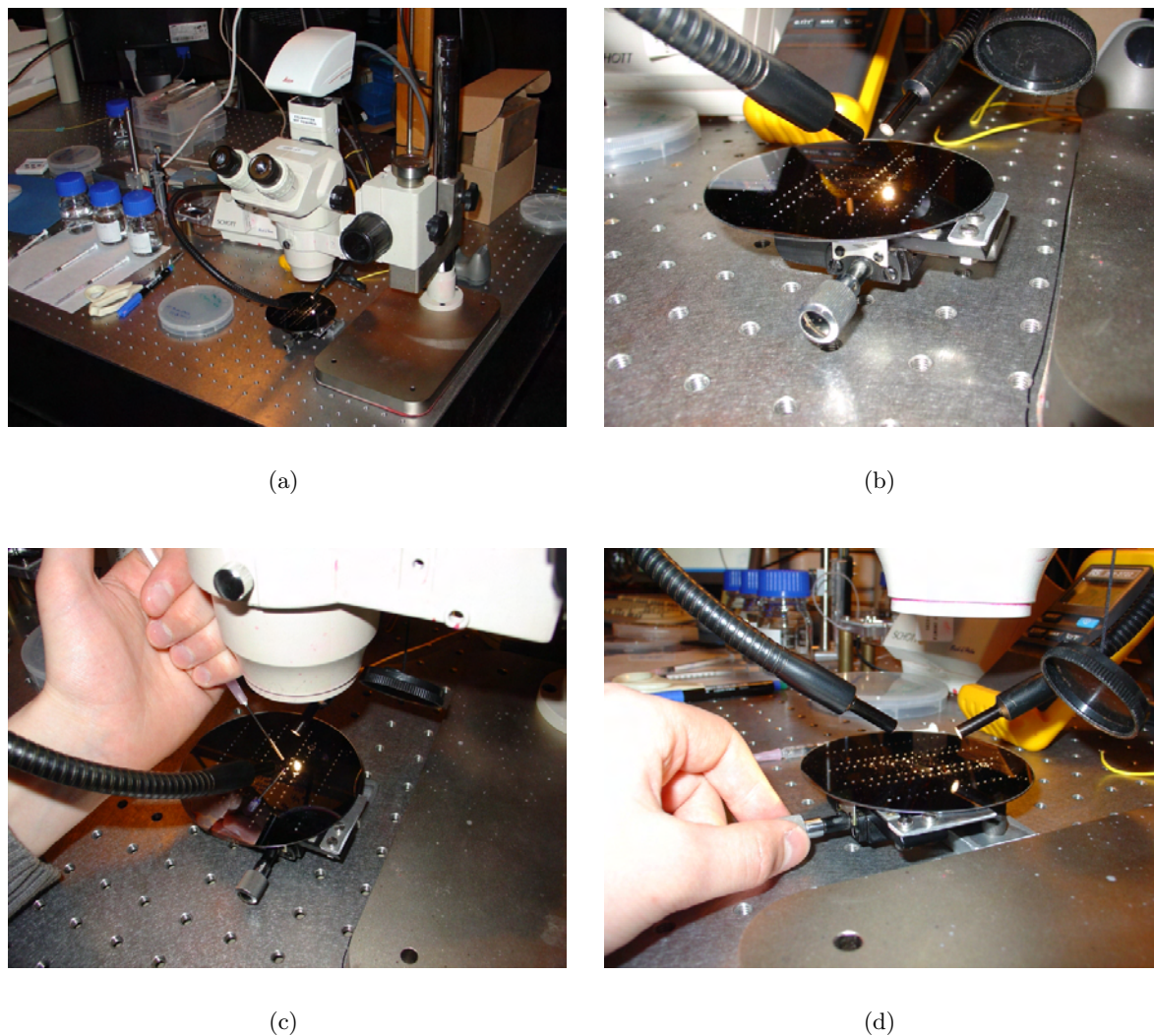
Figure 7.3: Pictures of the setup. (a) The complete setup with wafer placed on stage. (b) The stage with wafer and light. (c) The wafer being loaded using a syringe. (d) The wafer being moved using the stage.

7.4   Flow measurements in the nanochannels

Having made a suitable setup, measurements on the nanochannels were ready to be carried out. Each measurement was performed by placing a droplet on the inlet and at the same time starting the recording. As the meniscus progressed through the nanochannel the stage was moved in order to keep the meniscus in the field of view. After the meniscus had reached the end of the nanochannel the recording was stopped. All measurements were performed within a week after bonding to minimize any timedependence, and since

we did not know, if the channels would collaps with time.

For the low channels ranging from 25 nm to 300 nm in height, a time-lapse function was used when recording the movie. This time-lapse made it possible to acquire a maximum of one frame pr. second, which was sufficient, since the filling times, found using Eq. (2.19) with $L = 15$ mm and $w = 50$ μm, were approximately 280 s and 28 s for 30 nm and 300 nm respectively for Milli-Q. Unfortunately the frame rate turned out to be quite unreliable, as a recording time of e.g. 400 s resulted in a movie of approx. 300 s, which implied the use of a time correction factor. After realizing this, several measurements of this correction factor were made, using varying work loads of the computer processor. This provided a time correction factor of 1.32. The time correction factor factor tells that instead of one second between two frames, as set in the software, the time is actually 1.32 s. The factor of 1.32 was used for the measurements already made on the devices. During the subsequent measurements a stop watch was used to obtain the real time correction factor, which were all in the range from 1.29 to 1.37.

For the high channels, that is 900 nm and 3.4 μm, the filling times were only approximately 11 s and 3 s respectively. Taking into consideration that the device had to be moved during measuring, only the meanders would be useful for the 3.4 μm channels, since these would fill in approximately 75 s, making it possible to use the time lapse mode. Filling of the short 900 nm channels nevertheless required a higher frame rate, in order to obtain sufficient amounts of data. This could be done by using a live recording mode in the software used, however, for reasons unknown to man the software could only handle a total of 52 frames in this mode. This provided e.g. 17 s with 3 frames pr. s or 13 s with 4 frames pr. s. As before, the real time was recorded using a stop watch in order to estimate the time correction factor, which in contrast to the time lapse mode all were less than or equal to one.

In order to keep track of the recorded movies, all data and comments such as time correction factor, temperature, name of the movie, and any irregularities and other phenomena observed during filling were typed into a spreadsheet, which was later used for the data analysis.

If any irregularities were observed, such as bad filling of the feeding channels or local bonding problems, the measurements were excluded from the data analysis.

All acquired movies were subsequently analyzed using Windows Media Player, which allowed the movie to be played frame by frame and thereby obtaining data sets of position and time of the meniscus. For each measurement 15 to 25 data sets for each channel were manually read off and typed into a spreadsheet. Obviously this was a very time demanding way of acquiring data, but it turned out to be the only way, since it sometimes was very difficult to find and thereby read off the position of the meniscus.

Chapter 8

Data treatment and results

In the following chapter the data acquired during measurements on the devices will be presented and analyzed. The data are divided into quantitative and qualitative results.

In order to have a high amount of measurements to base the statistical inference on, it was planned to do measurements on two perfect wafers at each height. This would yield a total of four chips of each type for each liquid at a given height. For the chips with straight channel this would give 36 data series. However, due to bonding problems this was not practically feasible and therefore the amount of data for a given height varies a lot. The actual amount for each height, width and liquid combination may be found in App. F.

First of all it is wanted to investigate if the dependence between time and position of the liquid meniscus is qualitatively as predicted by the theory. Secondly the slope of the expected L^2 vs. t dependence is examined, and the possible deviations for the smallest heights, due to the electroviscous effects mentioned in [9], are investigated using liquids with different ion-concentrations. As a last experiment it is inspected how the channel width affects this slope.

8.1 Analysis of filling speed

First the quantitative results, being the relation between the meniscus position and time, will be treated and compared with the theoretical predictions. For this purpose the devices with 20 μm and 50 μm wide channels have primarily been used.

8.1.1 L^2 vs. t dependence

As stated in Sec. 2.3.4 the propagation of the liquid is assumed to depend on time as $L^2 \propto t$ and therefore a linear regression is suitable to determine if this general behaviour is valid in nanochannels. An example of a linear regression is shown in Fig. 8.1 for a 25 nm and a 925 nm chip with 50 μm wide channels.

The linear relation is clearly seen, and for far most of the performed measurements, the coefficient of correlation was $r \geq 0.999$. As this was observed for all channel heights and widths, it can be concluded that the overall relation between propagated length and

time can be described by $L^2 \propto t$ in the entire range from nanometer to micrometer scale independently of the height to width aspect ratio.
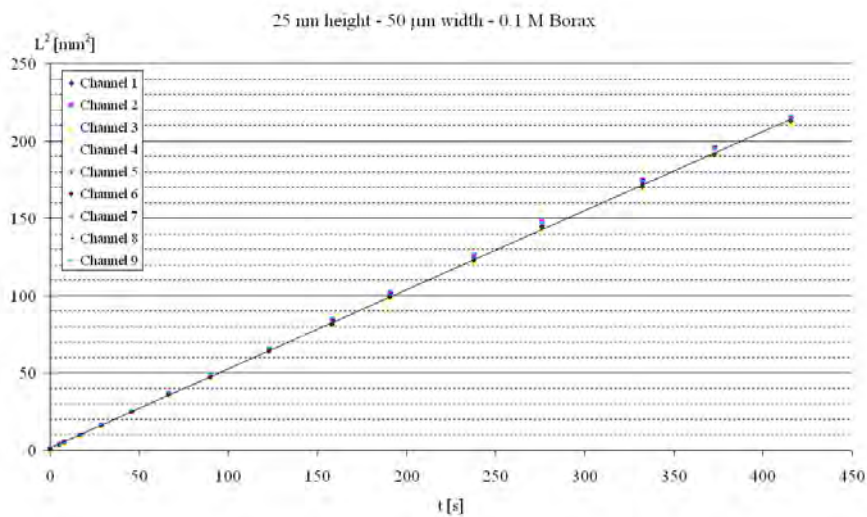
(a)
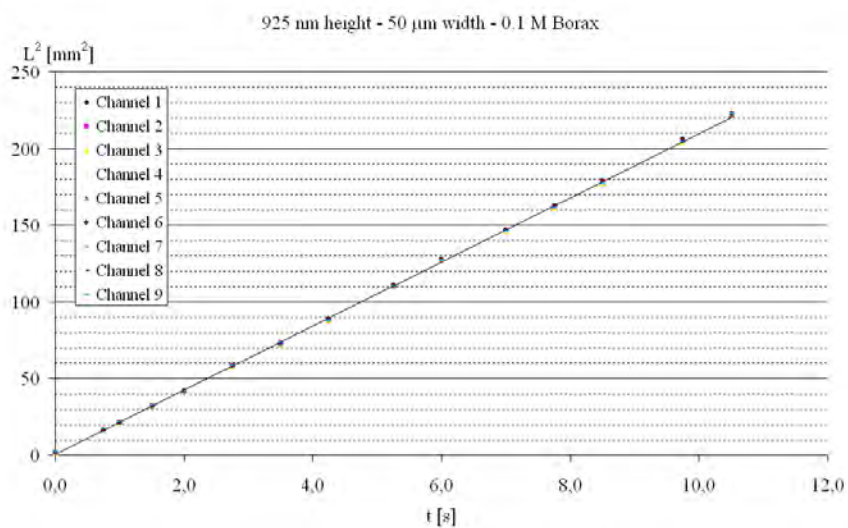
(b)

Figure 8.1: Plot of raw data showing L^2 vs. t. (a) 25 nm channel height and (b) 925 nm channel height. Both are filled with 0.1 M Borax and the linear relation is clearly seen. A linear regression for a random channel is shown.

Using the expression from Eq. (2.18) only accounting for capillary pressure it is also expected that the filling speed will be increased with the channel height. Thus plotting L^2 vs. t for the different heights should according to this yield a fan of straight lines with increasing slopes a_{meas} for increasing heights.

In Fig. 8.2 the mean of the slopes, obtained from water fillings, are plotted using both a standard and a double logarithmic coordinate system, so in this way all the individual lines can be shown in the same graph. For filling of 20 μm channels the overall picture is the same as in Fig. 8.2, independently on the liquid used.

When calculating the mean of the slopes, each channel has been treated as being independent. This implies that each straight channel chip provided nine individual data set, and the meander chips two. Meanders and short channels of same width and height have been treated as having identical properties. This decision was substantiated by the fact that comparison of the filling rates showed no tendency of meanders being filled neither faster nor slower than straight short channels.

The uncertainty related to the calculation of the slope from a single channel is obtained by considering the uncertainty when reading off a single data set. This has been estimated to be ± 50 μm for the position and ± 0.5 s for the time in time lapse mode. However, as this is a constant deviation for every data point, it has only a diminutive influence on the obtained slope and has thus been disregarded.

Although actually being a calculated quantity, the slopes acquired from each channel of a given height will be treated as a single measurement. The statistics will thus be applied to the sample of slopes which are assumed to originate from a normal distributed population.

The uncertainty on the mean of the slopes for a given height and liquid combination is based on the standard deviation s of the slopes. Using a $(1 - \alpha) = 95\%$ degree of confidence for small samples[1], the uncertainty $u(\bar{a}_{\mathrm{meas}})$ on the mean $\bar{a}_{\mathrm{meas}}$ is calculated as

$$u(\bar{a}_{\mathrm{meas}}) = t_{\alpha/2} \frac{s}{\sqrt{n}}, \tag{8.1}$$

where n is the sample size and $t_{\alpha/2}$ is the two-tailed t-distribution with $n - 1$ degrees of freedom.

It is readily observed from Fig. 8.2 that the uncertainty on the means are indeed very small as the error bars can hardly be seen, although plotted. This implies that the deviation of the channels in between is very small.

Despite the general tendency of increasing slope with increasing height, it is seen that the 32 nm channels have a smaller slope than the 25 nm channels. It has not been possible to find a reasonable explanation for this deviation. However, as all measurements are performed on the same wafer, it is likely that one of the treatments has altered the surface properties. This could for instance have resulted in a contact angle different from what was measured on the dummies. Unfortunately no other wafers with a height of 32 nm were available for comparison.

Furthermore the measurements from the 42 nm high channels are only based on Milli-Q water. This unfortunate fact originates from the severe bonding problems. In another

---

[1]Small sample refers to $n < 30$, n being the number of measurements (in this case channels) [5, p. 233].
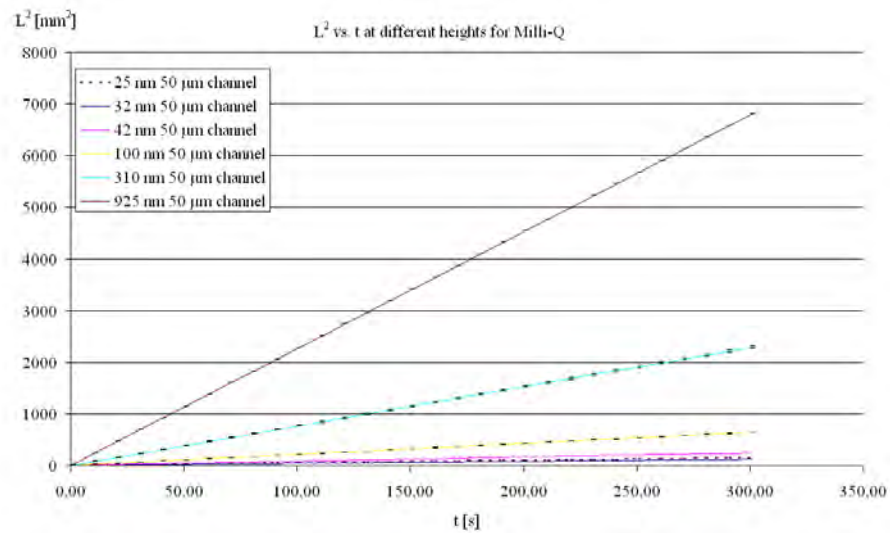
(a)
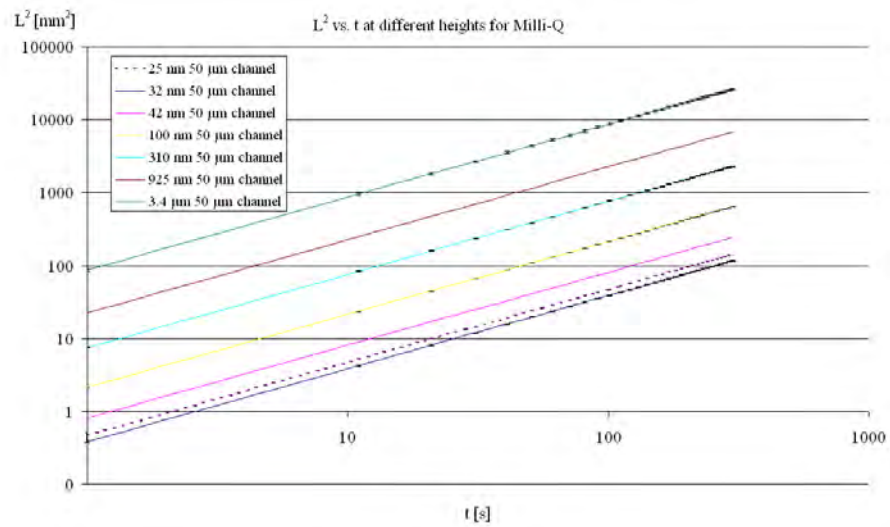
(b)

Figure 8.2: The L^2 vs. t dependence for increasing channel heights, based on the mean slope of the measurements with Milli-Q water in 50 μm channels. (a) Shows the slopes for heights up to 925 nm. In (b) a double logarithmic plot is given for all measured heights.

42 nm wafer the menisci were moving in abrupt steps very much different from the continuous propagation seen in all the other channels, and hence the data from this wafer have been disregarded.

8.2 Comparison with theory

An appropriate quantity to describe the relation between theory and measurements is the electroviscous retardation factor Υ_{ev} which for this purpose is given by Eq. (2.38). Before comparing the results with the theoretical predictions, it is necessary to determine the uncertainties on all parameters used in the calculations.

8.2.1 Uncertainty estimation and calculation

Besides the uncertainties connected to the liquid properties given in Tables 7.2 and 7.1, one must also estimate the uncertainty on the dimensions of the channel. As described in Sec. 4.4.1 the height for the oxide defined channels has been estimated to have an uncertainty of $u(h) = 5$ nm, whereas the dry etched are estimated to $u(h) = 50$ nm. The uncertainty in the width is not of great importance due to the high aspect ratio. Nevertheless an uncertainty has been estimated as two times the channel height, due to underetch, plus 0.1 μm, due to the photolithography process. For the dry etched channels, the contribution from the underetch has been replaced by the contribution from the scallops which from Fig. 4.10(a) are estimated to be approximately 300 nm wide.

It is now possible to estimate the uncertainty on the electroviscous retardation factor using the law of error propagation, [6, p. 8],

$$u(y) = \sqrt{\left(\frac{\partial Y}{\partial X_1}u(x_1)\right)^2 + \left(\frac{\partial Y}{\partial X_2}u(x_2)\right)^2 + \cdots + \left(\frac{\partial Y}{\partial X_N}u(x_N)\right)^2}, \qquad (8.2)$$

where y is the parameter for which the uncertainty is wanted and $X_1 \ldots X_N$ are the independent, uncorrelated variables upon which y depend. Eq. (8.2) is used on the expression for the theoretical slope a_p given by Eq. (2.20). Using Eq. (8.1) for the measured slope, the total uncertainty on Υ_{ev} is thus found by, [6, p. 10],

$$u(\Upsilon_{ev}) = \Upsilon_{ev}\sqrt{\left(\frac{u(a_p)}{a_p}\right)^2 + \left(-\frac{u(a_{meas})}{a_{meas}}\right)^2}. \qquad (8.3)$$

8.2.2 The electroviscous retardation factor

From all measurements the electroviscous factor can be calculated and plotted for the different channel heights. This is done for the 20 μm and 50 μm wide channels in Fig. 8.3. There is a tendency that the electroviscous retardation factor increases with lower channels. However, for the two lowest channels an exception is observed as $\Upsilon_{ev,\ 25\ nm} < \Upsilon_{ev,\ 32\ nm}$. Whether it is the retardation factor for 25 nm or 32 nm that deviates from the tendency is impossible to say, since $\Upsilon_{ev,\ 25\ nm}$ may be too low as well as $\Upsilon_{ev,\ 32\ nm}$ may be too high.
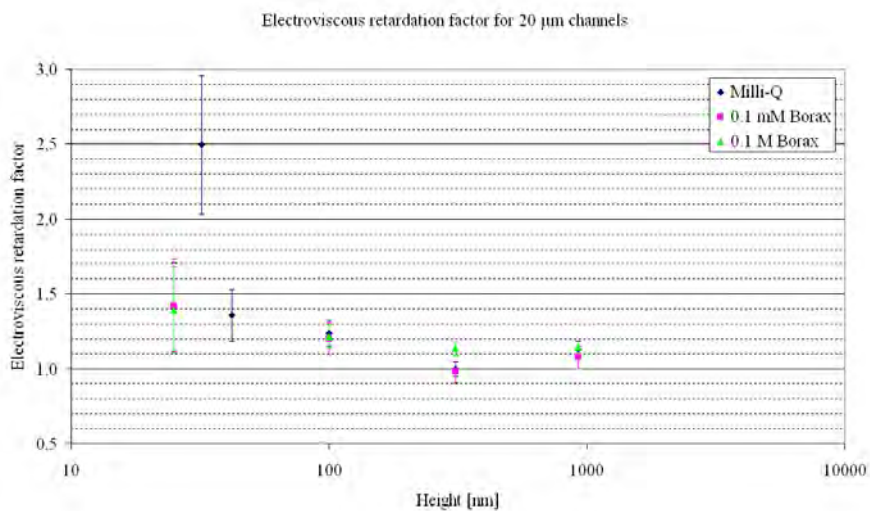
(a)
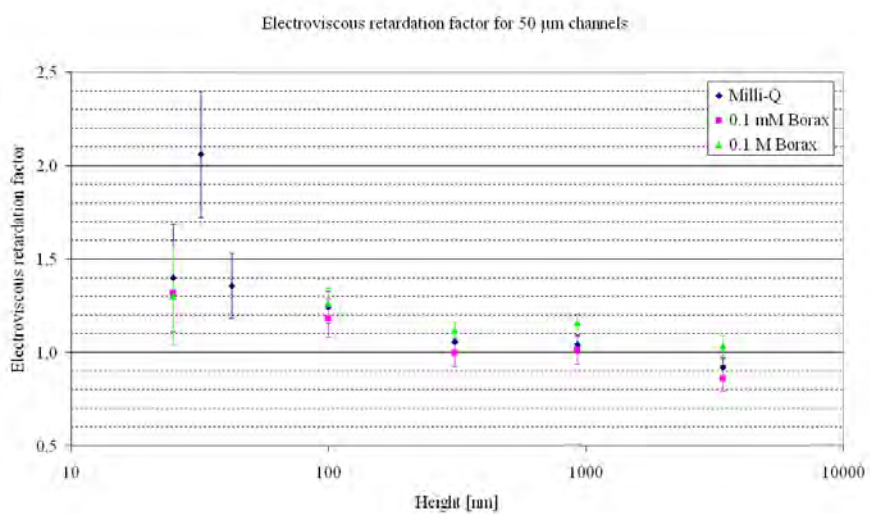
(b)

Figure 8.3: The electroviscous retardation factor of various height and liquid combinations. (a) and (b) shows for 20 μm and 50 μm wide channels respectively.

But as the electroviscous retardation factor for the 32 nm high channels is remarkably higher, compared to all other measurements, it is likely to believe that this is as previously

mentioned caused by a change of the surface properties somewhere in the fabrication process. Therefore this channel height is considered an outlier and will be disregarded in the following.

The values of the electroviscous retardation factor range from 1.42 ± 0.31 for the smallest channel height and down to 1.00 ± 0.07 for the highest. Values below 1.0 are also observed. For the two Borax solutions Υ_{ev} is approximately 7% lower for the 50 μm than the 20 μm wide channel at 25 nm. But apart from this, there is no general tendency that Υ_{ev} depends on the width. The values of the retardation factor for all channel heights and liquids can be found in App. G.

A way to determine if the increasing retardation factor can be explained by the electroviscous effect is to calculate ζ from the theoretical expression of Υ_{ev}, given by Eq. (2.37), where the values of Υ_{ev} are the mean values shown in Fig. 8.3. If the retardation can be described by the electroviscous effect, the zeta potential must be expected to be the same for all channel heights. Substituting all relevant liquid parameters into Eq. (2.37) and solving for ζ, several different values were obtained. These are given in App. H. For the case of water, the calculations are only valid for the two largest channel heights. For the 925 nm channel values of $\zeta = 18 \pm 4$ mV and 10 ± 6 mV are found, whereas the result is imaginary for the 3.4 μm channels. This is not surprising as the retardation factor in this case was found to be $\Upsilon_{ev} < 1$, which does not comply with the theory predicting that the electroviscous effect will always retard the flow.

Likewise, imaginary results are found for most of the measurements using 0.1 M Borax. This is caused by the fact that within the Debye-Hückel approximation ζ is determined from a quadratic equation, which for certain parameters have no real roots. To avoid imaginary solutions, the theory must be derived without applying the Debye-Hückel approximation as done in [15].

Generally the calculated values of the zeta potential do either violate the Debye-Hückel approximation or become imaginary, and thus we can not ascribe the different values of Υ_{ev} to the electroviscous effect with the limitations presented in Sec. 2.4.

Comparing the results to the ones found by N.R. Tas *et al.* [9], for a similar experiment with channels in the range from 53 nm to 111 nm, the tendency of an increasing retardation factor with decreasing channel height is consistent for the case of water. As the channel heights in the two projects are not identical, is not possible to make a direct comparison. But N.R. Tas *et al.* has reported a retardation factor of 1.23 ± 0.16 for a 53 nm channel and from their graphical representation a retardation factor of approx. 1.09 can be estimated for a 111 nm channel. Compared to the obtained values from our project of $\Upsilon_{ev} = 1.36 \pm 0.17$ for a 42 nm and $\Upsilon_{ev} = 1.24 \pm 0.09$ for a 100 nm channel height, there is however a tendency that our results are slightly higher.

This difference can be ascribed to several factors. First of all the fabrication methods differ in the two projects, and as we have seen, the properties of the silicon dioxide changes considerably with time. Therefore the surfaces are hard to compare from chip to chip. Furthermore, the liquids can not be considered equal since water is very sensitive to contamination due to the low natural ion concentration. Another difference is that in the experiment by N.R. Tas *et al.* [9] all measurements are made with no bubbles in the channels. As will be explained in Sec. 8.3.3 we have a lot of bubbles, which are likely

to change the hydraulic resistance of the channel. It was not technically possible to do analysis on the direct effect of the bubbles as the formation of bubbles happened faster than the low frame rate of the recorded movies.

Considering the two Borax solutions used here, there is only a small deviation from the results of water not being significant for the smallest heights. This strides against the experiment by N.R. Tas *et al.* [9] where a 0.1 M NaCl solution showed a significantly lower retardation factor for all channel heights. Although NaCl and Borax differ in chemical composition, their properties regarding Debye length λ_D and conductivity σ_{el} are similar. Assuming the same permittivity, 0.1 M NaCl has a Debye length of 0.96 nm and from the molar conductivity, [2, p. 22], one finds $\sigma_{el} = 1.07$ S m^{-1}. However, if the zeta potentials or other properties, of which we have no knowledge, differs from NaCl to Borax, this could possibly cause the observed deviation.

Just as for water, the retardation factor for 0.1 mM Borax in the 3.4 μm channel is less than unity. This is surprising, since the liquid is certainly not expected to flow faster. At this height also no electroviscous effects are expected to occur, unless a very high ζ potential exists. Therefore the value should be unity within the estimated uncertainties. Any deviation from this can be caused be systematical errors, which have been disregarded. As an example the contribution to the capillary effect from the sidewalls have been neglected due to the laterally not very well-defined meniscus. If there, despite the undefined meniscus, has been a contribution, this can cause the propagation to be faster than predicted. Also the presence of bubbles might influence the flow.

All in all the performed experiments show a tendency to a retardation in the propagation speed with decreasing channel height. With the estimated uncertainties this tendency is significant for all three liquids used, but it is not possible to conclude that the deviation is caused by the electroviscous effect described in Sec. 2.4. This can be caused by the fact that the utilized theory only applies within the Debye-Hückel approximation and no Debye layer overlap.

8.2.3   Rainbow arrays

The rainbow chips were used to investigate if the variation in channel width had any effect on the advancing meniscus. In case of an ideal surface with distinct radii of curvature the side walls of the channel will contribute to the capillary effect for low aspect ratios, and also the hydraulic resistance will change in this case. The first effect will decrease the advancement speed of the liquid for increasing widths, whereas the latter will promote the advancement speed. However, since the liquid front was seen not to be ideal in the horizontal plane, it is expected that the liquid will move relatively faster in broad compared to narrow channels. Due to the very high aspect ratio of the channels smaller than 900 nm this effect is not expected to be noticeable here.

An example of data sets for L^2 vs. t obtained from a rainbow chip is shown in Fig. 8.4, where results from a 32 nm and 925 nm chip are plotted. One immediately sees a significant difference in propagation speed as function of the channel width for the 32 nm rainbow chip, where the widest channels are considerably slower than the narrow ones. The opposite is the case for the high channels but less significant. In Fig. 8.5 the mean of the slope of L^2/t
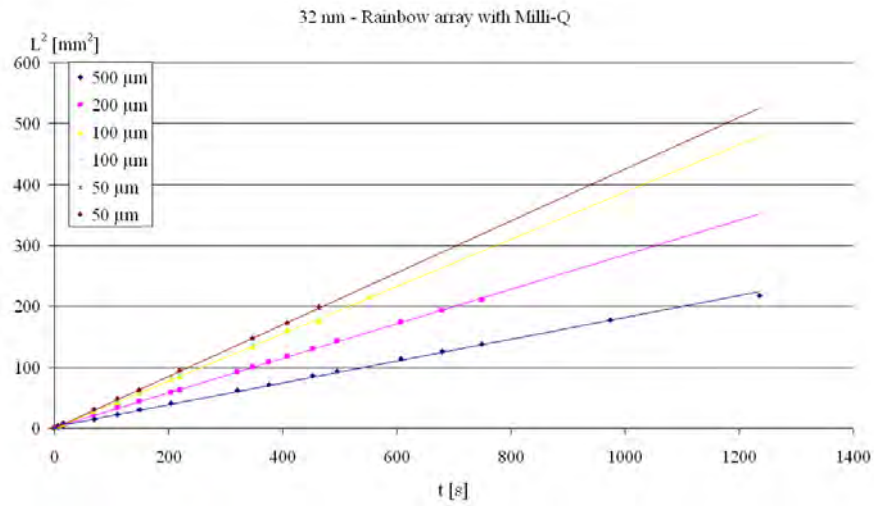
(a)
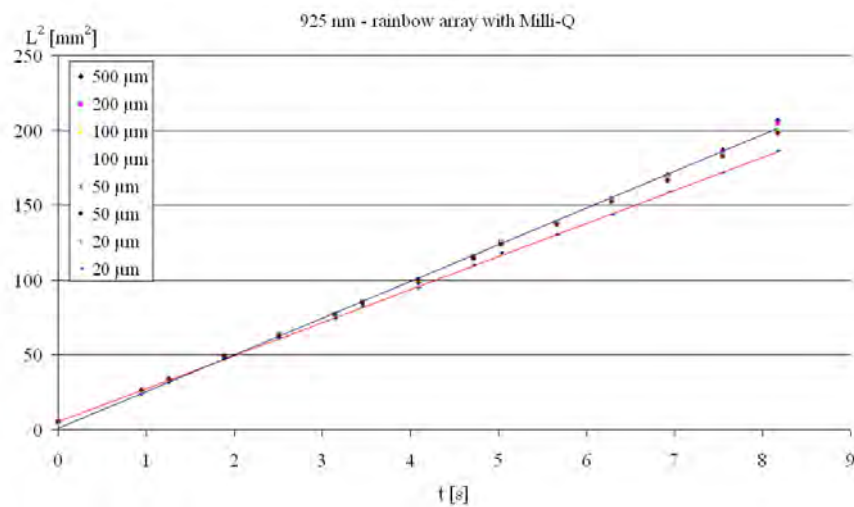
(b)

Figure 8.4: Raw data obtained from rainbow array chips. (a) A 32 nm rainbow shows that the propagation slows down with increasing channel width. The opposite is the case in (b) where for a 900 nm chip the blue and the red lines are linear regressions on date from a 500 μm and a 20 μm wide channel respectively.

for a given channel height and width is plotted, normalized to the slope of the 500 μm channel for each height.

There is a clear tendency that the propagation is reduced with increasing channel width for low channels. The tendency is seen to decline with increasing channel height and for 300 nm channels it is no longer observable. A possible explanation for this phenomenon could be that the channels are slightly collapsed. The wider the channels the greater bend down must be expected, and assuming a bend independent of the height, it will have a bigger influence on the shallow channels. This bend down will increase the hydraulic resistance and slow down the liquid flow. The 900 nm channels will possibly be independent of this, and the tendency is, as first predicted, that the flow increases with increasing width, see Fig. 8.2.3. However the observed effect of the channel width in this experiment is somewhat higher than predicted by the theory, why the change in hydraulic resistance cannot give the full explanation. Although only data for Milli-Q is presented, the overall tendency is the same for the Borax solutions and is also independent of which inlet hole is used.
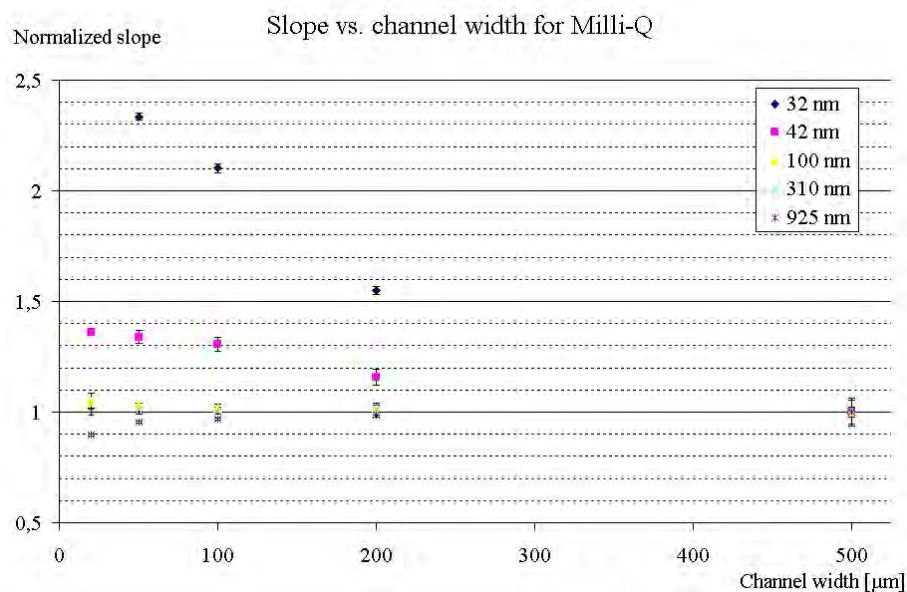
Figure 8.5: Slopes of L^2/t for rainbowchips of different heights normalized to the 500 μm wide channels. The higher the slope the faster the propagation. The error bars correspond to the normalized standard deviation on the measurements.

8.3   Qualitative observations

Besides the above mentioned quantitative data regarding filling speed, other more qualitative observations were made.

8.3.1 Evaluation of design

Before considering any phenomena regarding the nanochannels, the overall design of the chips is shortly evaluated. The primary concern of the design was it's ability to fill the nanochannels, which are connected to the inlet structures only in the very top. But due to the hydrophilic surfaces it was found that the transition from microchannel to nanochannel elapsed with no difficulties.

As expected, the nanochannels were filled almost simultaneously, when the inlet channel is loaded from one end, and Fig. 8.6(a) shows how the menisci in the nanochannels are nearly on line as marked by the red frame. The effect of having two holes in the inlet structure is illustrated in Fig. 8.6(b) where the upper part of an inlet channel for a 300 nm array is shown. The channel has been filled from the lower hole and as seen, the upper part of the channel is also filled leaving only a small bubble of air in the very top.

(a)   (b)
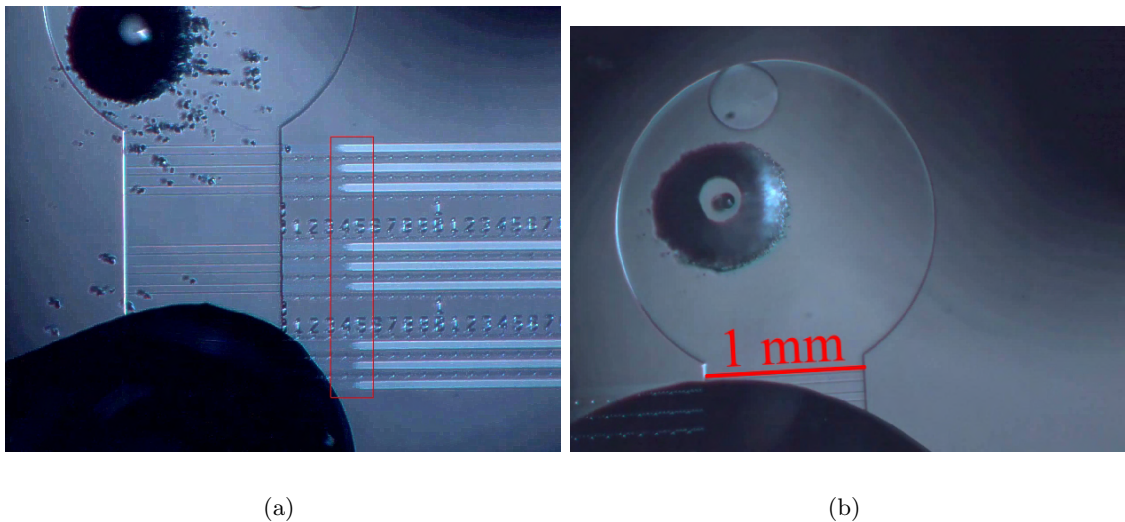
Figure 8.6: Evaluation of inlet structure. Due to the fast loading, the menisci of 100 nm channels in (a) are almost aligned. Having two holes in the inlet channel allows the channel to be filled completely as in (b) where the upper part is also filled leaving only a small air bubble.

Accidentally a single wafer was fabricated with inlet channels of same height as the nanochannels. Filling experiments were also conducted on this wafer, and it was found that the lack of deep inlet structures caused troublesome and uneven loadings. Furthermore the channel length in this constellation was not well defined. Therefore microchannels should always be used as inlet structure, and it can be concluded that the combination of microchannels and nanochannels yields a very reliable solution with perfect loading of the nanochannels. The overall design concept has thus been found very suitable and performed as expected with regard to the loading procedure.

8.3.2 Meniscus shape at various heights

During the experiments performed on both test batches and the final design we observed that the shape of the advancing liquid front changed radically with channel height. For the channels above 301 nm the front was concave laterally across the channel, whereas for smaller channel heights the front was more irregular with a lot of small projecting tongues and a general tendency to be convex across the channel. The phenomenon was very consistent for a given height and independent of liquid and channel width as can be seen in Fig. 8.7 and Fig. 8.8(a).

8.3.3 Bubbles and capillary effects

In the 900 nm channels the liquid front is observed to move faster at the side walls than in the middle of the channel. This causes a sideways movement of the liquid from the side walls towards the middle, and when these fronts meet a bubble is trapped due to the slower movement in the middle. This seems to happen with great regularity, since the distance between the bubbles is more or less constant, see Fig. 8.7(d). The bubbles are moving with the liquid, but at a slower speed.

Another type of bubbles can be seen on Fig. 8.8(a) where many bubbles are produced simultaneously in a 300 nm channel, presumably in the above mentioned way, where sideways moving liquid traps a bubble. In this case, however, the bubbles are mostly not moving with the liquid but stay immobile for wide channels. For 20 μm wide channels they have a tendency to be of same width as the channels and move with the liquid. But even more surprisingly, most of the bubbles disappear again. Fig. 8.8(b) is taken 50 s later than Fig. 8.8(a) and clearly all the bubbles are then gone. Since bubbles cannot diffuse away or dissolve in the liquid this fast, what is seen can not be bubbles, unless it is caused by an optical illusion. The fact that they are not moving supports this conclusion. A possible explanation of the phenomenon could be that small areas on the pyrex surface do not wet, and hence a thin layer of air is trapped on the surface giving the bubble-like look. After a while the surface wets, however, and the extremely small volume of air forms a real but invisible bubble due to the small size. However, since the wafer surfaces need to by hydrophillic in order to bond together, this explanation is nevertheless doubtful. Another possibility is that free-flowing bubbles are invisible, even if it's diameter is close to the height of the channel. This problem could maybe be solved by making an analysis of ray paths. For the 900 nm channels the front looks very strange with two similar long and narrow splits with a bubble forming at the end. This is seen in Fig. 8.9.

Whether the formation of bubbles occur or not, does not seem to depend on the channel width. However, it must be expected that 2D nanochannels will have a more regular meniscus and hence less tendency to produce bubbles. The presence of bubbles might be a problem for certain applications, where a homogeneous liquid is required. What causes the bubbles to be generated is not known, but their size and density seem to depend on the height.

Despite the presence of the bubbles, the strong capillary effect is nevertheless still observed.
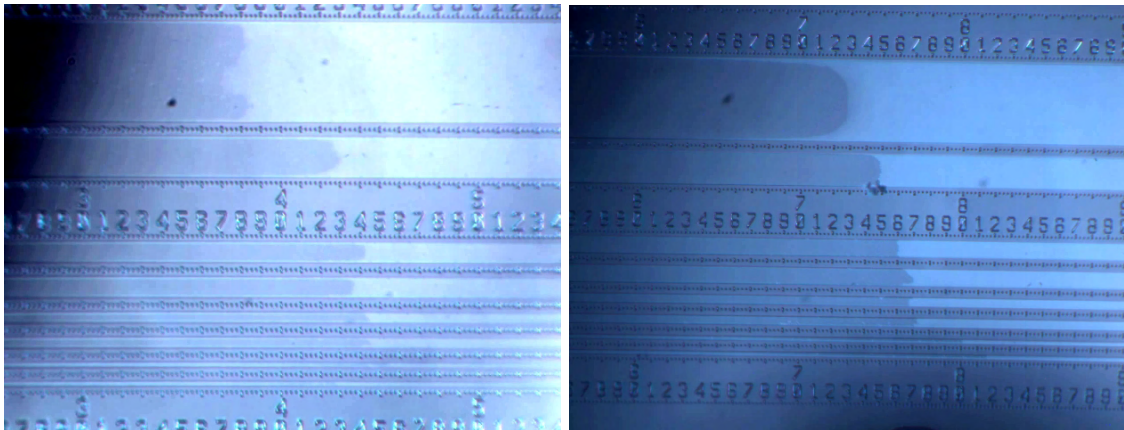
(a)

(b)
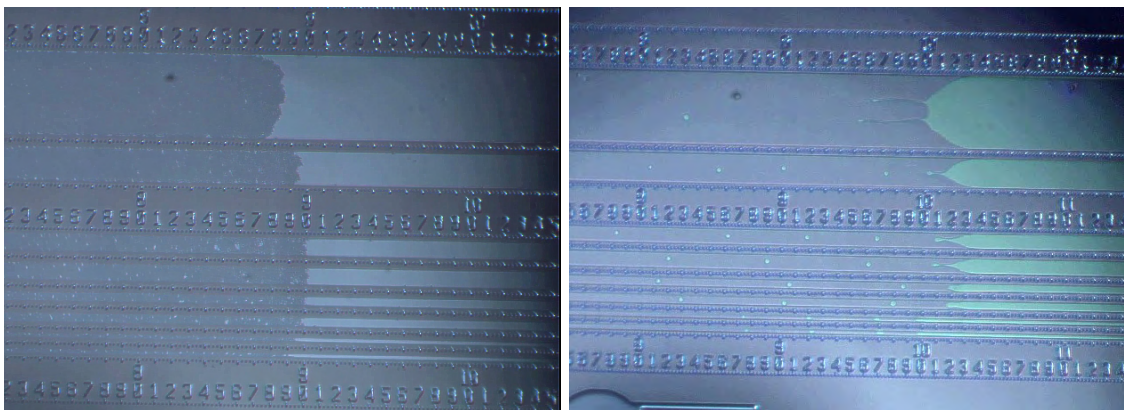
(c)

(d)

Figure 8.7: Typical pictures of the liquid fronts, shown as the dark areas, in a rainbow array at different channel heights. The smallest tickmarks are placed 25 μm apart. (a) 25 nm and (b) 42 nm tend to have convex and not very well defined fronts. (c) 100 nm have same overall shape but tends to have larger tongues and more bubbles. In 925 nm channels (d) the liquid protrudes along the sides regularly enclosing bubbles in the center of the channel.

(a)   (b)
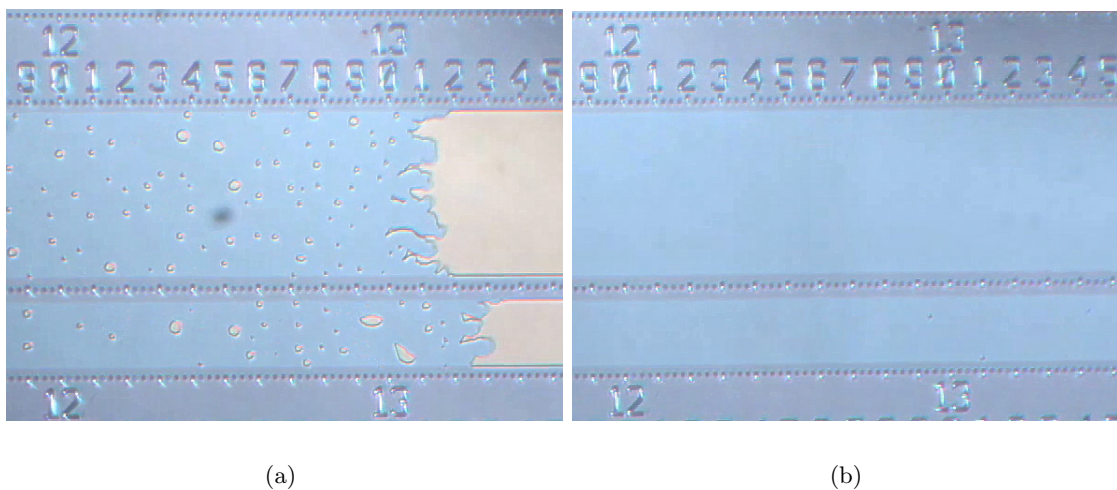
Figure 8.8: (a) In the 300 nm channel many bubbles are produced simultaneously, and the advancing front is seen to be very irregular. (b) This picture is taken 50 s later, and now all the bubbles have disappeared. The distance between the smallest tick marks is 25 μm.
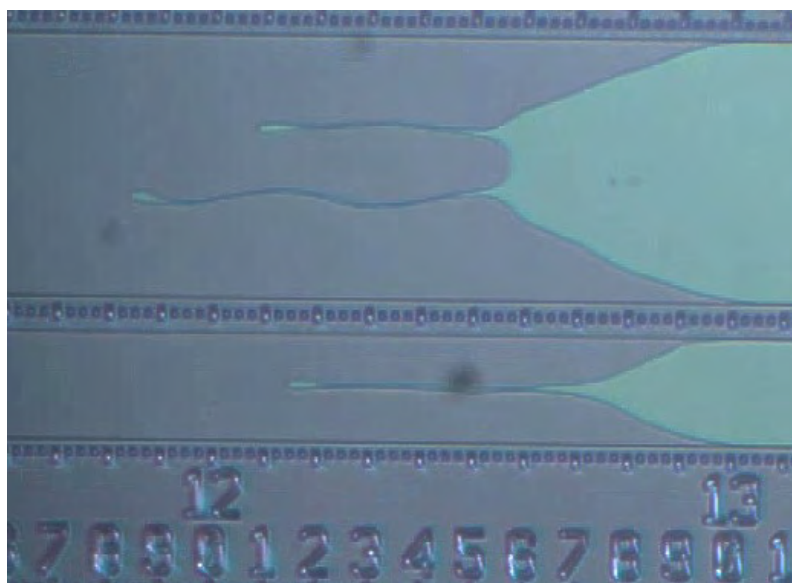
Figure 8.9: Liquid front of a 900 nm channel shows how the liquid (dark blue) creeps along the sides and tend enclose air, which results in formation of bubbles.

Chapter 9

Conclusion

During the project, several subjects have been treated. Based on the theory a suitable design for measuring capillary filling speed of nanochannels was developed. This combined microsized inlet structures with nanochannel arrays, which provided a reliable and very efficient filling of the nanochannels.

A process recipe for making nanochannels has been composed. The implementation of this showed an excellent consistence with simulations, and that it was possible to make nanochannels with a uniformity of a few nanometers on wafer scale using simple, cheap and reliable cleanroom techniques. Channels down to a height of 25 nm were fabricated in silicon dioxide.

A novel technique for making well-defined holes in pyrex was developed. This exploited the flexibility of making patterns in polymers by laser combined with the effectiveness of powder blasting, making the method very versatile, fast and easy to use.

The KOH fusion bonding turned out to be quite unreliable for bonding of oxidized silicon wafers to pyrex with pre-made inlet holes. Therefore this method must be developed further before applied to future work. However, successful bondings were found to be of high quality.

Experiments were conducted on the fabricated devices using three different liquids with different electrical properties. In the analysis of the experimental data it was found that for all liquids the square of the position of the propagating front showed a near perfect linear relation with time, as stated by the theory. This implies that the Poiseuille theory is still valid for dimensions down to 25 nm, which is in the vicinity of the limit for the continuum hypothesis. Furthermore, there was a tendency that the propagation in shallow channels was slower than predicted by the theory only accounting for capillary pressure and hydraulic resistance. However this tendency was generally the same for all three liquids, and it was not possible to ascribe this phenomenon to the electroviscous effect described by the theory presented in this report.

General observations of the behaviour of the liquids in the nanochannels showed that the shape of the advancing front depended on the channel height. Moreover it was observed that bubbles were generated during propagation with a density varying with height. This can be a problem for certain applications, but does not obstruct the capillary effect.

Appendix A

Detailed process recipe

Nanochannels in silicon wafer

| Si | SiO₂ | Resist | Pyrex | Film | **Color code** |

1. Wafer
- Use a single side polished silicon wafer.
- Thickness 525 μm, diameter 100 mm.

2a. Oxidation for channel walls
- 900 nm channels:
- Wet thermal oxidation, 3:05 h @ 1050°C.
- Expected: 968 nm oxide. Measured: 956 nm oxide.
- 300 nm channels:
- Wet thermal oxidation, 1:40 h @ 950°C.
- Expected: 341 nm oxide. Measured: 334 nm oxide.
- 100 nm channels:
- Dry thermal oxidation, 1:50 h @ 1050°C.
- Expected: 115 nm oxide. Measured: 108 nm oxide.
- 30 nm channels:
- Dry thermal oxidation, 1:05 h @ 1000°C.
- Expected: 54 nm oxide. Measured: 52 nm oxide.

3a. Photo resist for nanochannels
- HMDS oven for 32 min.
- Spin on 1.5 μm AZ5214 in Track 1.
- Program pr1_5 includes 1 min softbaking @ 90°C
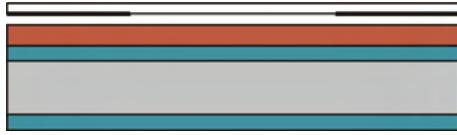
4a. Expose the photoresist

- Expose 8 sec. with mask "Nanochannels" in KS-aligner.
- Hard contact, constant intensity ci2 - 9.0 mW/cm^2.
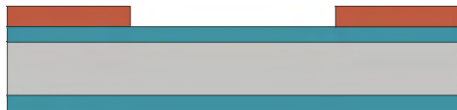
5a. Develop resist

- 60 sec. with agitation in AZ351B. (17 vol%)
- 5 min rinse in DI water with bubbles.
- Spin dry.

6a. BHF etch

- Remove monolayer:
+ Method used in project:
- Plasma Asher
- O$_2$: 50 mL/min, N$_2$: 50 mL/min, P: 150 W, t: 10 min.
+ Method to be used in the future:
- O$_2$ plasma in ASE.
- Dip in BHF.
- 900 nm: 20 min.
- 300 nm: 6:30 min
- 100 nm: 2 min
- 30 nm: 2 min
- Rinse in DI water with bubbles for 5-10 min.
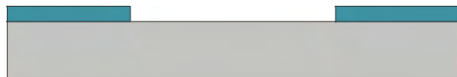
7a. Strip resist

- Rinse in "coarse" acetone 60 s.
- Rinse in "clean" acetone 60 s.
- Immerse in DI water.
- Spin dry.

8a. Photo process for feeding channels

- HMDS oven for 32 min.
- Spin on 2.2 μm AZ5214 in Track 1 pr2_2.
- Expose 10 s in KS-aligner using mask "Feed Channels". Align to substrate.
- Hard contact, constant intensity ci2 - 9.0 mW/cm^2.
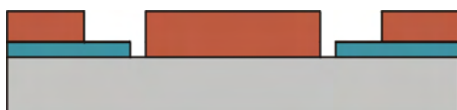
9a. Develop feeding channels

- Develop 70 sec. in AZ351B. (17 vol%)
- 5 min in DI water with bubbles.
- Spin dry.

10a. Preliminary etch process for feeding channels

- Dip in BHF.
- 900 nm: 20 min.
- 300 nm: 6:30 min
- 100 nm: 2 min
- 30 nm: 2 min
- Rinse in DI water with bubbles for 5-10 min.
- Spin dry.

11a. Primary etch process for feeding channels

- Dry etch in ASE.
- 25 cycles shallow etch (etch: 6.5 s, passivation: 5.0 s) → 20 μm deep channels.
- 3 min O_2 clean to remove passivation layer.

12. Strip resist

- Rinse in "coarse" acetone 60 s.
- Rinse in "clean" acetone 60 s.
- Immerse in DI water.
- Spin dry.

13. RCA clean

- RCA clean procedure without BHF:
- 10 min in SC-1: H_2O + NH_4OH + H_2O_2.
- 2 min in coarse DI water, 2 min in DI water with bubbles.
- 10 min in SC-2: H_2O + HCl + H_2O_2.
- 2 min in coarse DI water, 5 min in DI water with bubbles.
- Spin dry.

14. Oxidation for channel bottom

- Dry thermal oxidation.
- 50 nm bottom:
- Settings: 65 min @ 1000°C.
- Expected result: 52 nm oxide in channels.
- Measured result: 53 nm.
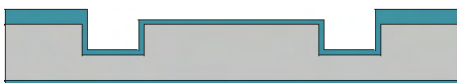
15. Measure channel height

- Use Dektak 8 profiler

Pyrex lid

16. Pyrex wafer

- Thickness 500 μm diameter 100 mm.

17. Clean wafer

- Clean on both sides with Triton soap on turntable.
- Immerse in DI water.
- Clean in piranha for 10 min.
- Rinse in DI with bubbles for 10 min.
- Spin dry.
- Bake in 250°C oven for 20 min.

18. Spin on resist

- Spin 4.2 μm AZ5214 on the bonding side using JTC4_2 on Track 1.
- Hard bake for 2 min at 120°C hotplate.

19. Mount blue film

- Mount self sticking 70 μm blue SWT 20 Nitto tape on wafer front.
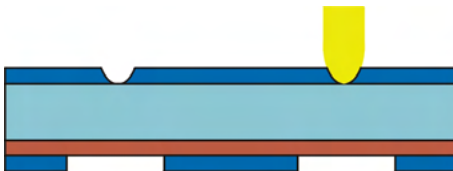
20. Define holes

- Not a clean room process:
- Ablate holes in the film by CO_2 laser.
- 1 mark pass at 200 mm/s.
- 10% power by 150 W CO_2 laser.
- Use hole diameter of 0.5 mm.
- Mount blue film with mirrored hole pattern on the backside.
- Use hole diameter of 2 mm for easy alignment.
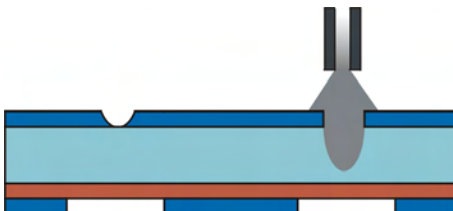
21. Powder blast access holes

- Not clean room processes.
- Wear Gloves, dust mask and lab coat.
- Mount wafer in vented chamber.
- Powder blast holes perpendicular to surface.
- Use Microetcher II$^{\text{TM}}$ with 50 to 90 μm Al_2O_3 particles.
- Air pressure: 6-7 bar.
- Distance to blue film: A few millimeters.
- Process time: < 20 s pr. hole.
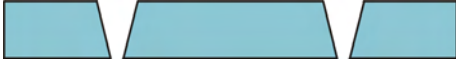
22. Clean and strip lids

- Not a clean room process:
- Blow away excess particles by compressed air.
- Wife off blue film with moist cloth
- Remove blue film by pliers.
- Clean room processes:
- Clean wafers thoroughly with DIW in clean room wardrobe.
- Strip resist by acetone in fume hood.
- Spray and immerse in DIW with bubbles.
- Optional: Strip resist in "coarse" acetone 2 min.
- Optional: Strip resist in "fine" acetone 2 min.
- Immerse in DIW with bubbles for 5 min.
- Spin dry.

Bonding silicon and pyrex
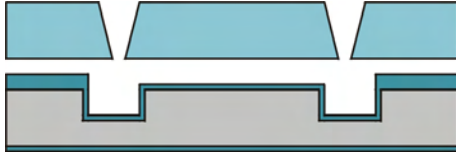
23. Cleaning

- Clean pyrex and silicon in Piranha for 10 min.
- Immerse in DI water with bubbles ≥ 5 min.
- Dip in 50 wt% KOH @ < 80°C for 2 min 30 sec.
- Immerse in with bubbles DI water 5 min.
- Spin dry.
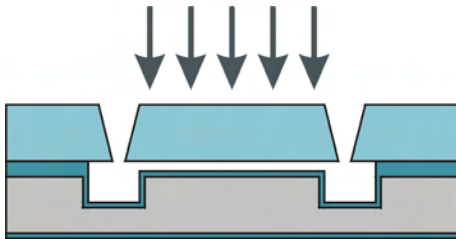
24. Bonding

- Align and bring together by hand.
- Apply pressure from center and outwards by hand.
- Fairly high pressure required.
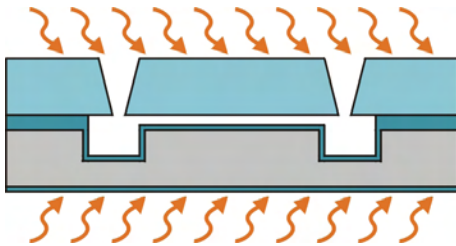
25. Baking

- Not a clean room process.
- Bake in program oven using the following procedure.
- heat to 120°C at 5°C/min, dwell in 30 min.
- heat to 475°C at 5°C/min, dwell in 120 min.
- heat to 550°C at 5°C/min, dwell in 300 min.
- heat to 475°C at 5°C/min, dwell in 60 min.
- heat to 20°C at 15°C/min.
- end of program.

Dicing out chips
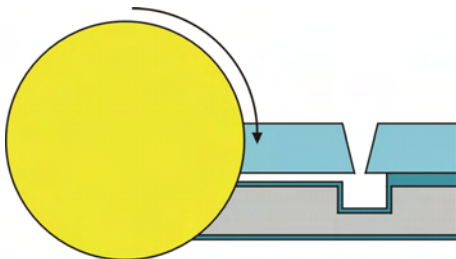
26. Dicing out

- Not a clean room process.
- Cover holes by blue film.
- Dice out wafers using the diamond circular saw.

Microchannels in silicon wafer

For the 3 μm channels the above mentioned steps 2 to 11 are substituted with the following steps.
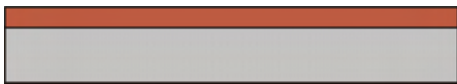
2b. Photo resist for microchannels

- HMDS oven for 32 min.
- Spin on 1.5 μm AZ5214 in Track 1.
- Program pr1_5 includes 1 min softbaking @ 90°C.

3b. Expose the photoresist

- Expose 8 sec. with mask "Nanochannels" in KS-aligner.
- Hard contact, constant intensity ci2 - 9.0 mW/cm^2.

4b. Develop resist

- 60 sec. with agitation in AZ351B. (17 vol%)
- 5 min rinse in DI water with bubbles.
- Spin dry.

5b. Etch of microchannels

- Dry etch in ASE.
- 4 cycles shallow etch (etch: 6.5 s, passivation: 5.0 s) → 3.4 μm deep channels.
- 3 min O_2 clean to remove passivation layer.

6b. Strip resist

- Rinse in "coarse" acetone 60 s.
- Rinse in "clean" acetone 60 s.
- Immerse in DI water.
- Spin dry.
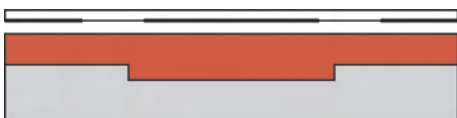
7b. Photo process for feeding channels

- HMDS oven for 32 min.
- Spin on 6.2 μm AZ4562 in Track 2 pr6_2.
- Expose in KS-aligner using mask "Feed Channels". Align to substrate.
- Hard contact, constant intensity ci2 - 9.0 mW/cm^2.

8b. Develop feeding channels

- Develop 3 min. in AZ351B. (17 vol%)
- 5 min in DI water with bubbles.
- Spin dry.

9b. Primary etch process for feeding channels

- Dry etch in ASE.
- 25 cycles shallow etch (etch: 6.5 s, passivation: 5.0 s) →
  20 μm deep channels.
- 3 min O_2 clean to remove passivation layer.

Appendix B

SUPREM ATHENA file

This appendix contains input file used for simulations of a 100 nm channel with 50 nm bottom oxide. Be aware that line breaks have been made in order to fit to the page. Line breaks are marked by \... .

Source code

```
go athena

#TITLE: 100 nm channel fabrication using oxidation and BHF etch. \...
        ... 50 nm bottom

#Define the grid
#
line x loc=0.9 spac=0.005
line x loc=1.9 spac=0.005
#
line y loc=0.00 spac=0.001
line y loc=.4 spac=0.01


#initialize the (100) wafer
#
init silicon orientation=100 c.phos=1.0e15

# ----- Grow thick oxide -----
#
diffuse tim=110 minutes tem=1050 dryo2

#Save structure
#
```

```
struct outf=Channel2D_100nm_tyk_0.str.

# ----- Photomasking -----

#Spinning and etch of 1.5 um AZ-resist for nanochannels
#
deposit photo thick=1.5 divis=14
etch photo    start x=-1 y=-5
etch          cont  x=-1 y=5
etch          cont  x=1 y=5
etch          done  x=1 y=-5


# ----- Perform isotropic etch of channel ----
#
rate.etch machine=BHF wet.etch oxide iso=700 a.m

etch machine=BHF time=150 second dx.mult=0.1

#Save structure
#
structure outfile=Channel2D_100nm_tyk_1.str

# ----- Strip resist -----
#
strip

#Save structure
#
structure outfile=Channel2D_100nm_tyk_2.str

#Extract relevant data
#
extract name="Oxide Thickness center" thickness oxide x.val=0.95 \...
               ... datafile="Channel2D_100nm_tyk_Data.doc"
extract name="Oxide Thickness side" thickness oxide x.val=1.7 \...
               ... datafile="Channel2D_100nm_tyk_Data.doc"

# ----- Grow second oxide layer -----
#
diffuse tim=65 minutes tem=1000 dryo2

#Extract relevant data
#
```

```
extract name="Oxide Thickness 2 center" thickness oxide x.val=0.95 \...
                ... datafile="Channel2D_100nm_tyk_Data.doc"
extract name="Oxide Thickness 2 side" thickness oxide \...
                ... x.val=1.7 datafile="Channel2D_100nm_tyk_Data.doc"

#Save structure
#
structure outfile=Channel2D_100nm_tyk_3.str

# ----- Perform isotropic KOH etch for bonding -----
#
rate.etch machine=KOH50 wet.etch oxide iso=40 a.m

etch machine=KOH50 time=150 second dx.mult=0.1

#Save structure
#
structure outfile=Channel2D_100nm_tyk_4.str

#Extract relevant data
#
extract name="Oxide Thickness 3 center" thickness oxide \...
                x.val=0.95 datafile="Channel2D_100nm_tyk_Data.doc"
extract name="Substrate Thickness 3 center" thickness silicon \...
                x.val=0.95 datafile="Channel2D_100nm_tyk_Data.doc"

extract name="Oxide Thickness 3 side" thickness oxide \...
                x.val=1.7 datafile="Channel2D_100nm_tyk_Data.doc"
extract name="Substrate Thickness 3 side" thickness silicon \...
                x.val=1.7 datafile="Channel2D_100nm_tyk_Data.doc"

# ----- Plot the results -----
#
tonyplot -st Channel2D_100nm_tyk_*.str

quit
```

Appendix C

Simulation examples

This appendix contains simulation results showing how the etch time of the masked BHF and unmasked KOH can affect the lift of the corner.

The effect of BHF etch time is shown in Fig. C.1 for a 100 nm channel etched with 0% and 150% over-etch respectively. A close-up of the lifts corresponding to the etch times in Fig. C.1, using a 50 nm bottom oxide, is given in Fig. C.2, where the longer etch has resulted in a slightly larger lift. However it is laterally smooth and still very small compared to the lateral extent, and thus not expected to cause any problems with the bonding.

<div align="center">(a)   (b)</div>
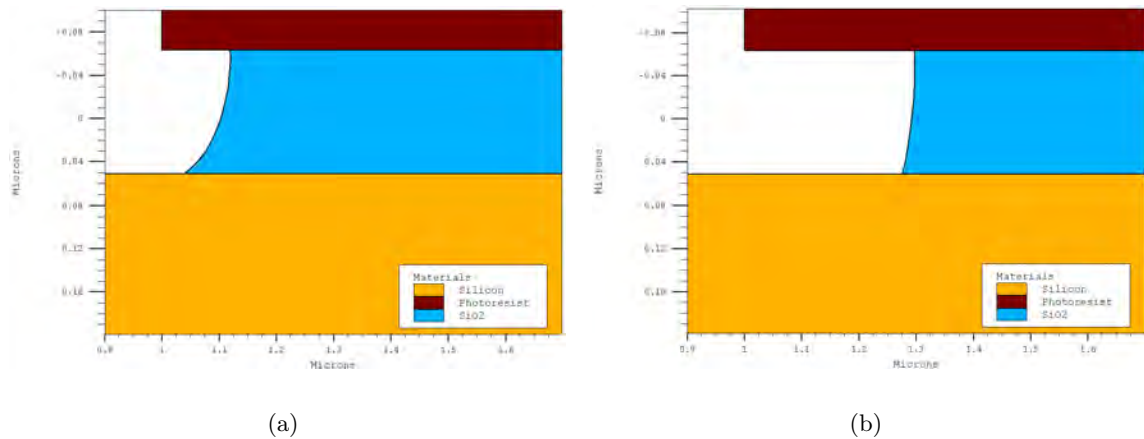
Figure C.1: Simulation results. The slope of the side wall for a resist masked BHF over-etch of approximately (a) 0% and (b) 150% of a 120 nm thick oxide, which is used for defining channels with a height of 100 nm. The longer the etch time, the steeper the wall becomes as a result of the isotropic etch.

The final process step is the unmasked KOH etch connected to the bonding process. As the channel corner will be etched from several sides, the lift will thus be slightly reduced.

(a)   (b)
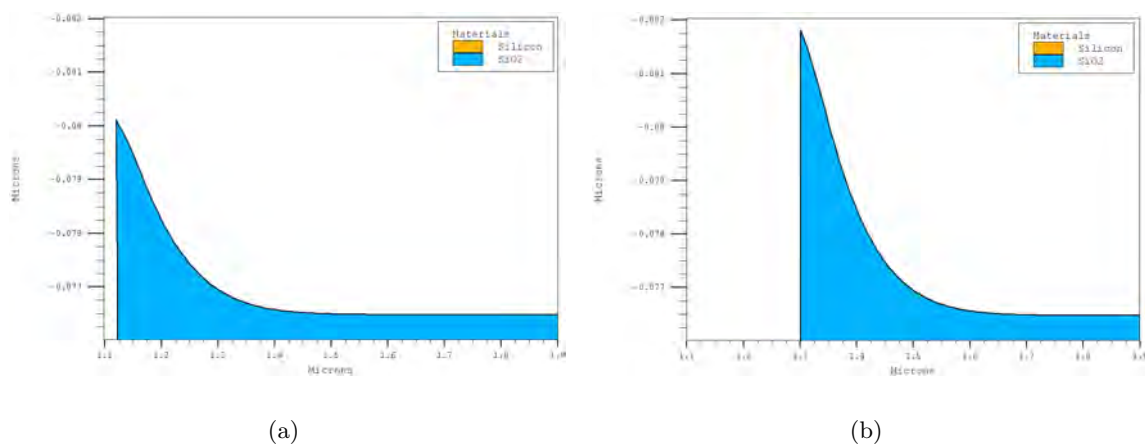
Figure C.2: Simulation results. Close-up of the lifts for a 100 nm channel with 50 nm bottom oxide. The adjusted parameter is the BHF over-etch, which is (a) 0% (3.5 nm lift) and (b) 150% (5 nm lift) respectively. The longer the etch time, the bigger the lift.

As an example, the lift-up for a 100 nm channel is reduced from app. 4.5 nm to 3.0 nm.

(a)   (b)
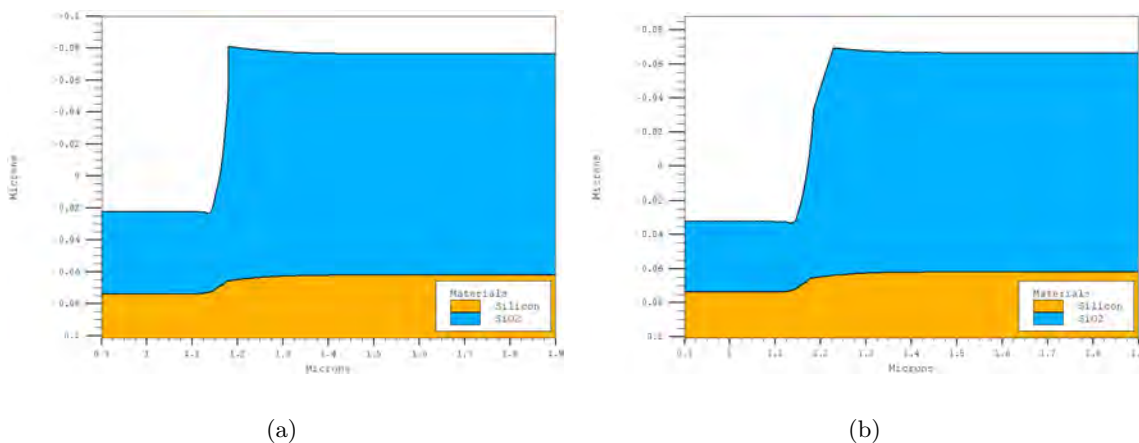
Figure C.3: Simulation results. The structure of the sidewall for a 100 nm channel (a) before KOH etch and (b) after KOH etch. The isotropic unmasked KOH etch reduces in this case the lift-up from app. 4.5 nm to 3.0 nm.

Appendix D

Measured and simulated values

This appendix contains the measured and simulated values for oxide thickness and channel height for both test and main batches.

Test batches

Expected height	484 nm	99 nm
Oxide 1 (Suprem)	494 nm	115 nm
Oxide 1 (Ellipsometer)	491 nm	117 nm
Oxide 2 (Suprem)	22 nm	115 nm
Oxide 2 (Ellipsometer)	20 nm	117 nm
Channel (Suprem)	484 nm	99 nm
Channel (Dektak)	493 nm	101 nm

Table D.1: Measured and predicted oxide thicknesses and channel heights for the two test batches.

Main batches

Batch number		**6**	**5**	**4**	**3**	**1**	**2**		
Expected height	[nm]	**3400**	**925**	**304**	**99**	**99**	**41**	**41**	**41**
Oxide 1 (Suprem)	[nm]	n/a	968	341	115	86	54	54	54
Oxide 1 (Ellipsometer)	[nm]	n/a	956	334	108	109	52	n/a	n/a
Oxide 2 (Suprem)	[nm]	53	53	54	53	54	53	53	53
Oxide 2 (Ellipsometer)	[nm]	52	52	52	52	52	52	52	52
Channel (Suprem)	[nm]	n/a	925	304	99	75	41	41	41
Channel (Dektak)	[nm]	3400	925	310	100	42	42	32	25
Channel (SEM)	[nm]	3400	n/a	n/a	90	n/a	n/a	n/a	n/a

Table D.2: Comparison of measured and simulated oxide thickness and channel height.

Appendix E

Bonding results

Substrate type	$T_{\text{KOH}}^{\text{sub}}$	$T_{\text{KOH}}^{\text{pyrex}}$	Prebond	Final bond	Date	Comments
25 nm	78°C	78°C	no		Apr 25	
25 nm	72°C	72°C	no		Apr 26	
25 nm	73°C	82°C	1	ok	Apr 29	
30 nm	51°C	53°C	1	ok	Mar 18	
30 nm	51°C	53°C	1	no	Mar 18	Broken pyrex.
30 nm	78°C	78°C	1	ok	Apr 11	
40 nm	74°C	74°C	no		Apr 25	
40 nm	68°C	68°C	no		Apr 26	
40 nm	73°C	82°C	no		Apr 29	
40 nm	73°C	82°C	1	ok	Apr 29	
47 nm	58°C	58°C	1	ok	Mar 18	
100 nm dummy	86°C	86°C	1		Jan 14	Dummy sub. and pyrex.
100 nm dummy	78°C	78°C	no		Jan 14	Dummy sub., pyrex with HF holes.
100 nm test	72°C	72°C	no		Jan 14	Pyrex with HF holes.
100 nm test	82°C	82°C	1	ok	Jan 17	Dummy pyrex
100 nm test	69°C	69°C	1	ok	Jan 20	First with powder blast holes.
100 nm test	61°C	55°C	2	small area	Mar 1	
100 nm	54°C	65°C	2	small area	Mar 30	Broken pyrex. Wriggled.
100 nm	54°C	65°C	2	small area	Mar 30	Wriggled during prebonding.
100 nm	70°C	70°C	2		Apr 6	Tested for stability.
100 nm	73°C	73°C	no		Apr 13	
100 nm	77°C	77°C	no		Apr 15	
100 nm	67°C	67°C	2		Apr 15	Only holes for every other chip.
100 nm	72°C	77°C	1	ok	Apr 18	
300 nm	49°C	65°C	no		Mar 30	Wriggled during prebonding.
300 nm	49°C	57°C	2	small area	Mar 30	Wrenched during prebonding.
300 nm	73°C	73°C	2	small area	Apr 6	
300 nm	84°C	84°C	1		Apr 11	Dummy pyrex. Proves subs. is ok.
300 nm	78°C	78°C	2		Apr 13	
300 nm	74°C	74°C	no		Apr 15	
300 nm	72°C	77°C	1	ok	Apr 18	Only holes for every other chip.
300 nm	72°C	77°C	1	ok	Apr 18	
500 nm test	78°C	78°C	1	ok	Jan 20	
900 nm	47°C	57°C	2	small area	Mar 30	Wriggled during prebonding.
900 nm	47°C	57°C	2	small area	Mar 30	Wriggled during prebonding.
900 nm	79°C	79°C	no		Apr 6	
900 nm	85°C	85°C	1	ok	Apr 13	Broken pyrex
3400 nm	66°C	66°C	no		Apr 25	
3400 nm	69°C	69°C	1	ok	Apr 25	
3400 nm	65°C	65°C	1	ok	Apr 26	

Table E.1: Bonding results.

Appendix F

Number of measurements

Milli-Q

No. of measurements	Channel width for short chips [μm]		Channel width for rainbow chip [μm]				
Channel heigth [nm]	20	50	20	50	100	200	500
25	9	9	0	0	0	0	0
32	20	59	5	5	10	10	6
42	9	27	4	4	8	8	8
100	18	20	2	2	4	4	4
310	11	18	2	2	4	4	4
925	9	20	2	2	4	4	4
3400	0	4	0	0	0	0	0

Table F.1: Number of measurements performed with Milli-Q for different height and width combinations

0.1 M Borax

No. of measurements	Channel width for short chips [μm]		Channel width for rainbow chip [μm]				
Channel heigth [nm]	20	50	20	50	100	200	500
25	9	18	4	4	4	2	2
32	0	0	0	0	0	0	0
42	0	0	0	0	0	0	0
100	18	17	2	2	4	4	4
310	11	9	2	2	4	4	4
925	9	18	1	1	2	2	2
3400	0	4	0	0	0	0	0

Table F.2: Number of measurements performed with 0.1 M Borax for different height and width combinations

0.1 mM Borax

No. of measurements	Channel width for short chips [μm]		Channel width for rainbow chip [μm]				
Channel heigth [nm]	20	50	20	50	100	200	500
25	9	18	0	0	0	0	0
32	0	0	0	0	0	0	0
42	0	0	0	0	0	0	0
100	18	12	2	2	4	4	4
310	11	9	2	2	4	4	4
925	9	9	2	2	4	4	4
3400	0	4	0	0	0	0	0

Table F.3: Number of measurements performed with 0.1 mM Borax for different height and width combinations

Appendix G

Electroviscous retardation factor

Milli-Q

	Channel width [μm]			
	20	50	50	50
Channel height [nm]	Υ_{ev} [ ]	Υ_{ev} [ ]	$u(\Upsilon_{ev})$ [ ]	$u(\Upsilon_{ev})$ [ ]
25	1.41	1.40	0.29	0.29
32	2.50	2.06	0.43	0.34
42	1.36	1.36	0.17	0.17
100	1.24	1.24	0.09	0.09
310	1.00	1.05	0.05	0.05
925	1.13	1.04	0.05	0.05
3400	n/a	0.918	n/a	0.05

Table G.1: The electroviscous retardation factor and corresponding uncertainty for Milli-Q

0.1 M Borax

	Channel width [μm]			
	20	50	50	50
Channel height [nm]	Υ_{ev} [ ]	Υ_{ev} [ ]	$u(\Upsilon_{ev})$ [ ]	$u(\Upsilon_{ev})$ [ ]
25	1.39	1.30	0.29	0.27
32	n/a	n/a	n/a	n/a
42	n/a	n/a	n/a	n/a
100	1.22	1.26	0.08	0.08
310	1.13	1.12	0.05	0.04
925	1.15	1.16	0.04	0.04
3400	n/a	1.03	n/a	0.06

Table G.2: The electroviscous retardation factor and corresponding uncertainty for 0.1 M Borax

0.1 mM Borax

Channel height [nm]	Channel width [μm]			
	20	50	50	50
	Υ_{ev} [ ]	Υ_{ev} [ ]	$u(\Upsilon_{\text{ev}})$ [ ]	$u(\Upsilon_{\text{ev}})$ [ ]
25	1.42	1.32	0.31	0.28
32	n/a	n/a	n/a	n/a
42	n/a	n/a	n/a	n/a
100	1.20	1.18	0.11	0.11
310	0.98	1.00	0.07	0.07
925	1.08	1.01	0.08	0.07
3400	n/a	0.86	n/a	0.07

Table G.3: The electroviscous retardation factor and corresponding uncertainty for 0.1 mM Borax

Appendix H

Calculated zeta potentials

In the following tables the color red indicates that the value exceeds the Debye-Hückel approximation, green indicates an overlap of the Debye layers and gray indicates both.

Milli-Q

Channel height [nm]	Channel width [μm]			
	20	50	50	50
	ζ [V]	ζ [V]	$u(\zeta)$ [V]	$u(u(\zeta))$ [V]
25	0.41	0.41	0.19	0.2
32	0.62	0.52	0.15	0.14
42	0.23	0.23	0.07	0.07
100	0.08	0.08	0.02	0.02
310	Imaginary	0.007	Imaginary	0.014
925	0.018	0.01	0.004	0.006
3400		Imaginary		Imaginary

Table H.1: The zeta potential and corresponding uncertainty for Milli-Q

0.1 M Borax

Channel height [nm]	Channel width [μm]			
	20	50	50	50
	ζ [V]	ζ [V]	$u(\zeta)$ [V]	$u(u(\zeta))$ [V]
25	0.89	0.34	6.4	0.6
32	n/a	n/a	n/a	n/a
42	n/a	n/a	n/a	n/a
100	Imaginary	Imaginary	Imaginary	Imaginary
310	Imaginary	Imaginary	Imaginary	Imaginary
925	Imaginary	Imaginary	Imaginary	Imaginary
3400		Imaginary		Imaginary

Table H.2: The zeta potential and corresponding uncertainty for 0.1 M Borax

0.1 mM Borax

Channel height [nm]	Channel width [μm]			
	20	50	50	50
	ζ [V]	ζ [V]	$u(\zeta)$ [V]	$u(u(\zeta))$ [V]
25	0.09	0.08	0.04	0.04
32	n/a	n/a	n/a	n/a
42	n/a	n/a	n/a	n/a
100	0.04	0.04	0.01	0.01
310	Imaginary	Imaginary	Imaginary	Imaginary
925	0.18	0.055	0.11	0.21
3400		Imaginary		Imaginary

Table H.3: The zeta potential and corresponding uncertainty for 0.1 mM Borax

Appendix I

L-Edit chip layout

All the devices shown below are 8×22 mm^2 in dimension. Red and black areas indicate nanochannels and green areas are inlet structures .
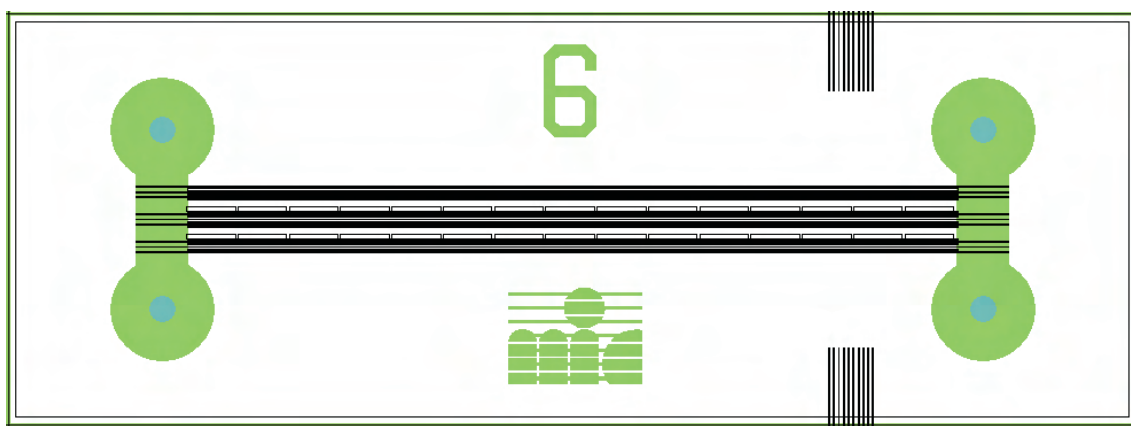
Figure I.1: L-Edit file showing the mask for a device with 20 μm wide channels.
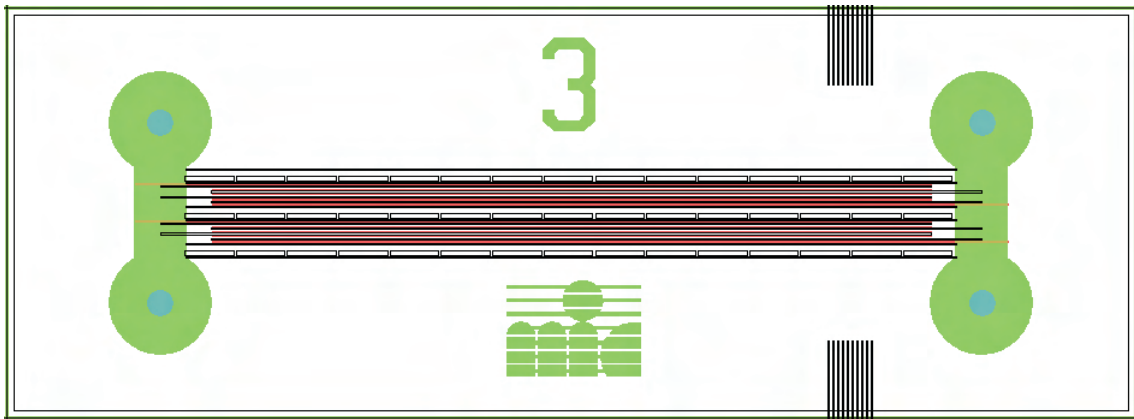
Figure I.2: L-Edit file showing the mask for a device with 20 μm wide meanders.
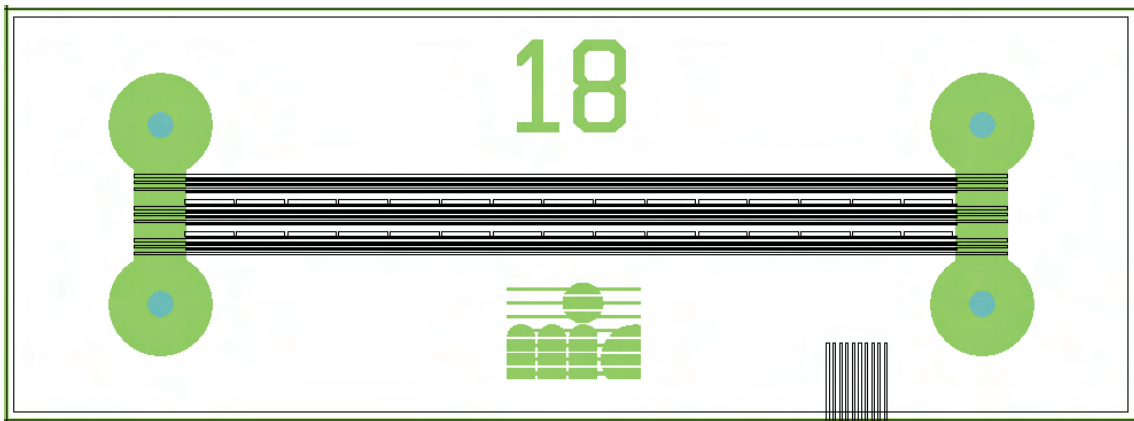
Figure I.3: L-Edit file showing the mask for a device with 50 μm wide channels.
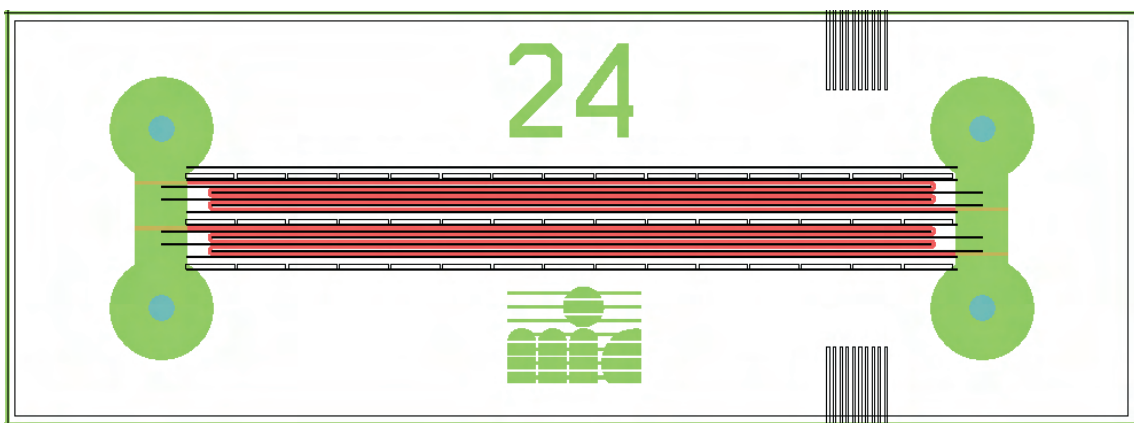
Figure I.4: L-Edit file showing the mask for a device with 50 μm wide meanders.
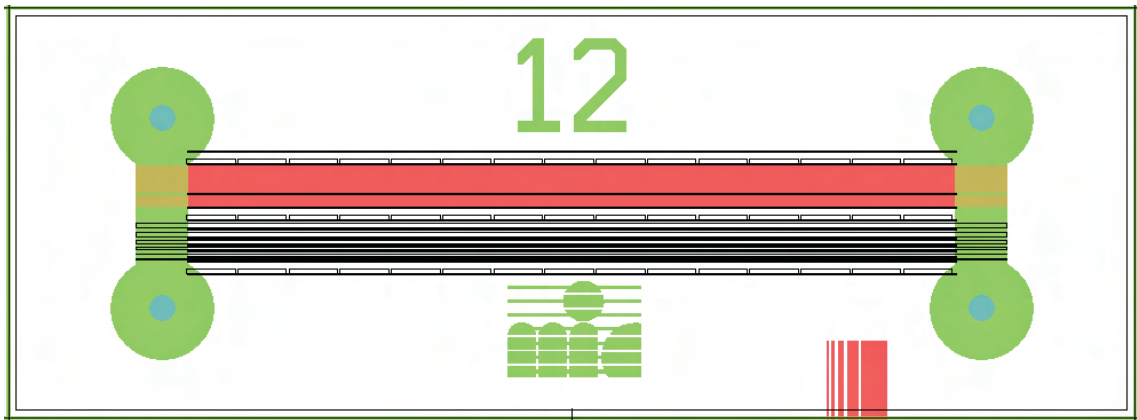
Figure I.5: L-Edit file showing the mask for rainbow chips.
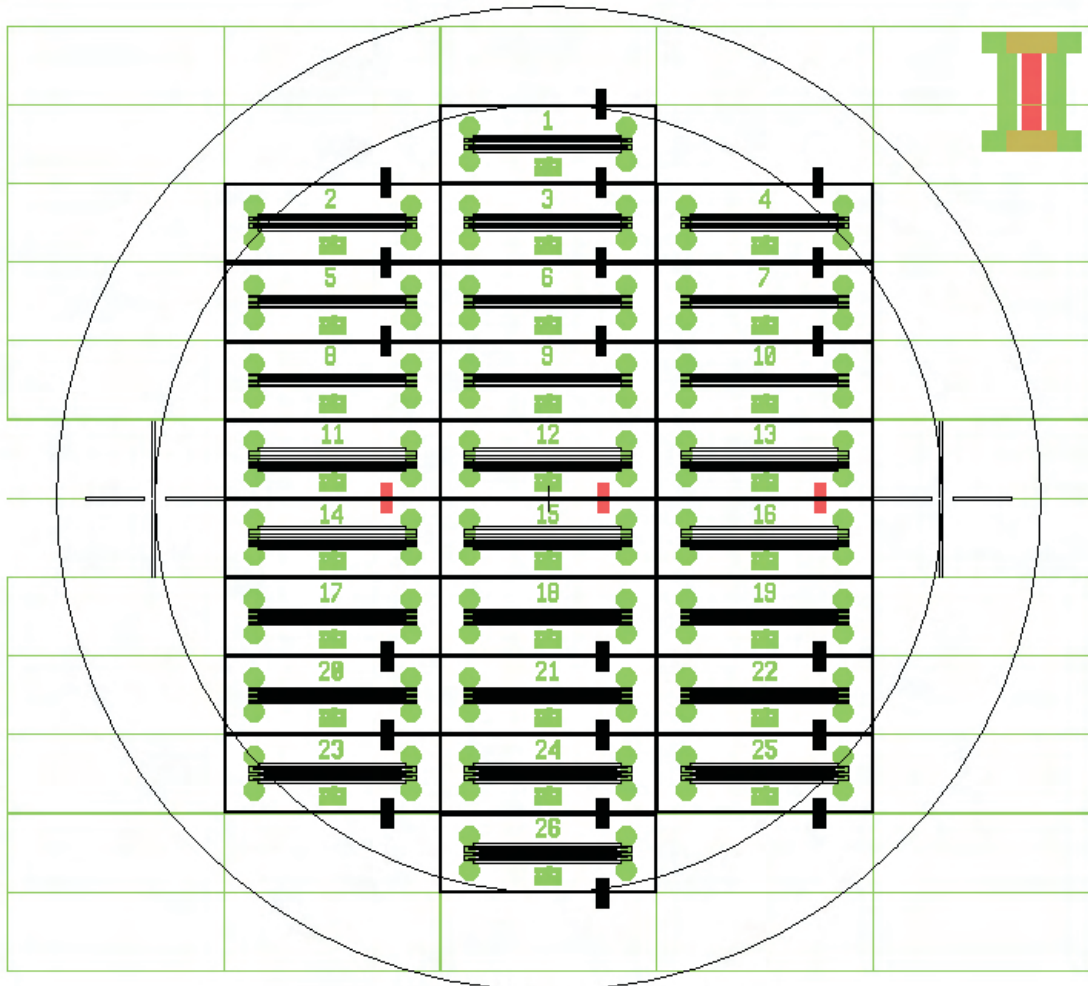
Figure I.6: L-Edit lay-out for a 100 mm wafer.

Appendix J

DVD

The enclosed disc contains various data such as layout files, movies and a PDF-version of the report.

Bibliography

Books, lecture notes and theses

[1] *Theoretical microfluidics,*
     Henrik Bruus,
     Lecture notes, fall 2004,
     MIC - Department of Micro and Nanotechnology,
     DTU - Technical University of Denmark.

[2] *Principles of Electroosmotic Pumps,*
     Anders Brask,
     Master Thesis,
     MIC, Technical University of Denmark, 2003.

[3] *Silicon VLSI Technology,*
     Fundamentals, Practice and Modeling,
     J.D. Plummer, M.D. Deal, P.B. Griffin,
     Prentice Hall, 2000,
     ISBN 0-13-085037-3.

[4] *Fundamentals of Semiconductor Fabrication,*
     Gary S. May, Simon M. Sze,
     Wiley International Edition, 2004,
     ISBN 0-471-45238-6.

[5] *Miller & Freund's,*
     Probability and Statistics for Engineers,
     International Edition, Seventh Edition,
     Richard A. Johnson,
     Pearson, Prentice Hall, 2005,
     ISBN 0-13-127840-1.

[6] *Måletekniske begreber og behandling af måledata,*
     2. udg. 1999.02.23, revision 2000.11.17, 1.udg 1999.01.05,
     K.A.Mørch,
     Institut for Fysik, DTU

[7] *CRC Handbook of Chemistry and Physics,*
    85th Edition, 2004-2005
    CRC Press
    Online Edition.

[8] *DATABOG fysik kemi,*
    Erik Strandgaard Andersen, Paul Jespersgaard og Ove Grønbæk,
    10. udgave, 3. oplag,
    F & K forlaget,
    ISBN 87-872-2959-5

Articles

[9] *Capillary filling speed of water in nanochannels,*
    N.R. Tas, J. Hanevel, H.V. Jansen, M. Elwenspoek and A. van den Berg,
    Appl. Phys. Lett., **Vol. 85, No. 15**, 11 October 2004.

[10] *Wafer-to-wafer fusion bonding of oxidized silicon to silicon at low temperatures,*
     A. Berthold *et al.*,
     Sensors and Actuators **A68** (1998) 410-413,
     Elsevier.

[11] *Wafer bonding for microsystems technologies,*
     U. Gösele, Q.-Y. Tong *et al.*,
     Sensors and Actuators **74** (1999) 161-168,
     Elsevier.

[12] *Failure Mechanisms of Pressurized Microchannels, Model, and Experiments,*
     M. T. Blom *et al.*,
     Journal of Microelectromechanical Systems **Vol. 10, no 1** (March 2001) 158-164.

[13] *On electroviscous effects in microchannels,*
     P. Vainshtein & C. Gutfinger,
     J. Micromech. Microeng. **12** (2002) 252-256.

[14] *Zeta potential of microfluidic substrates:*
     1. Theory, experimetal techniques, and effects on separations,
     Brian J. Kirby & Ernest F. Hasselbrink Jr.,
     Electrophoresis 2004, **25**, 187-202.

[15] *Electrokinetic Flow in Ultrafine Capillary Slits,*
     D.Burgreen and F.R.Nakache,
     The Journal of Physical Chemistry,
     Vol. 68, no. 5, 1084-1091. May, 1964.

[16] *Mask materials for powder blasting,*
Henk Wensink, Henri V. Jansen, J. W. Berenschot and Miko C. Elwenspoek,
J. Micromech. Microeng., **10** (2000) 175-180.

[17] *Smoothing of ultrasonically drilled holes in borosilicate glass by wet chemical etching,*
T. Diepold and E. Obermeiery,
J. Micromech. Microeng., **6** (1996) 29-32.

Internet references

[18] Brigham Young University
Dep. of Electrical and Computer Engineering
http://www.ee.byu.edu/cleanroom/KOH.phtml
Reference on site: J. Electrochem. Soc. Vol 137, 11, Nov 1990, 3612-3632

[19] www.daneng.com
Danville Engineering

[20] www.ronvig.com
Rønvig Dental Mfg. A/S